THE OBSERVATION OF THE WEAK RADIATIVE HYPERON DECAY $\Xi^\circ \to \Lambda^\circ\pi^\circ\gamma$ at KTEV/E799, FERMILAB

by

HUICAN PING

A dissertation submitted in partial fulfillment of the

requirements for the degree of

DOCTOR OF PHILOSOPHY

(PHYSICS)

at the

UNIVERSITY OF WISCONSIN - MADISON

2005

Acknowledgments

Many people contributed to this thesis in a number of ways. Without them, this work would not have been possible. I would like to take this time to thank them.

First and foremost, I would like to express my deepest gratitude to my major advisor Professor Albert Erwin for his continued guidance and advice during all of the years of my research. I will always be deeply grateful for his generosity in helping me achieve my goals. I have been very lucky to have the opportunity to learn from him.

I want to express my gratitude to Prof. Charles J. Goebel at the Physics Department of University of Wisconsin_Madison. He gave us a theoretical calculation of the Branching Ratio for our signal mode $\Xi^\circ \to \Lambda^\circ \pi^\circ \gamma$. It is very important for me to fulfill this project.

I would also like to thank my lab colleagues in Madison. Professor, Theodoros Alexopoulos taught me high energy physics, data analysis, computers, and most importantly work ethics during my first 2 years in Madison. Dr. Christos Velisaris also gave me useful suggestions and helps during the process of doing data analysis in the last 3 years.

I am indebted to all of the KTeV collaborators. I would like to give thanks to the hyperon group: E.J. Ramberg, E. Monnier, D.A. Jensen etc. I am grateful for

the financial support from the Department of Energy.

I really appreciate the help from the hardworking staff at the physics department B. Schutz, J. Buehlman, A. Lefkow and T. Sherron for making things really work for me.

I don't know how to express my appreciation to my wife, Gangjuan Jiang, whose love, friendship, support, and devotion are beyond description.

Contents

List of Tables

List of Figures

Abstract

The large sample of Ξ° hyperons available at KTeV 799 provides an opportunity to search for the Weak Radiative Hyeron Decay $\Xi^\circ \to \Lambda^\circ\pi^\circ\gamma$. We present a branching fraction measurement of $\Xi^\circ \to \Lambda^\circ\pi^\circ\gamma$ based on the E799-II experiment data-taking in 1999 at KTeV, Fermilab. We used the principal decay of $\Xi^\circ \to \Lambda^\circ\pi^\circ$ where Λ decays to a proton and a π^- as the flux normalization mode. This is the first observation of this interesting decay mode. 4 candidate events are found in the data. The branching ratio at 90% confidence level has been measured to be $(1.67\ ^{+1.45}_{-0.80}(stat.)\ \pm 0.50(syst.)) \times 10^{-5}$ or $(1.67\ ^{+1.16}_{-0.69}(stat.)\ \pm 0.50(syst.)) \times 10^{-5}$ at 68.27% confidence level.

Chapter 1

Introduction

The puzzle of Weak Radiative Hyperon Decays (WRHD) dates back to the 60's, when experiment [1] suggested large asymmetry in the $\Sigma^+ \to p\gamma$ decay, contrary to the expectation based on Hara's theorem [2]. During the last 30 years a large number of models have been constructed to treat these processes. But for a long time only some limited decays, such as $\Sigma^+ \to p\gamma$, were well studied and measured. One reason was that only limited experimental data were available.

Experimentlly, for 2-body final states, there are only two quantities relevant to the measurement of these decays: their branching fraction and the asymmetry of the photon emission with respect to the initial spin direction. Despite this, there is only one accurate measurement of a WRHD asymmetry, the decay $\Sigma^+ \to p\gamma$, where the asymmetry is unexpectedly large and negative. Theoretically, these decays are diffcult because of the involvement of weak, electromagnetic, and strong forces. One recent attempt has indicated that experimental measurements of the two Ξ° WRHD ($\Xi^\circ \to \Sigma^\circ\gamma$ and $\Xi^\circ \to \Lambda^\circ\gamma$) may resolve some of the questions surrounding this topic [3].

In KTeV the neutral beam contained a copious amount of neutral hyperons, Λ° and Ξ° which made KTeV a unique facility to study the rare decay of these

particles as well. For the decay $\Xi^\circ \to \Sigma^\circ\gamma$, the KTeV collaboration observed about 5,000 events on top of a background of 1,400 and gave a more precise branching ratio and asymmetry measurement [4].

This thesis will focus on the hyperon physics at KTeV. We will report the results of searching for the decay $\Xi^\circ \to \Lambda^\circ\pi^\circ\gamma$.

1.1 The Standard Model

The Standard Model of Particle Physics is an excellent description of nature at the level of its building blocks. All matter falls into three classification schemes: the quarks, the leptons, and the gauge bosons. The quarks contain charges of +2/3 and -1/3. For example, the flavored quarks, the up (u), charm (c), and top (t) quarks are of positive charge, whereas the down (d), strange (s), and bottom (b) quarks are of the negative charge. The anti-quarks have opposite sign. Most everyday matter is made up of protons and neutrons, which are in turn made up of the up and down quarks. These fermions and their properties are summarized in Table 1.1.

There are four forces found in nature governing the interactions, and they include the strong, the electromagnetic, the weak, and the gravitational. Sometimes, they are referred as the three forces with the elctromagnetic and weak combined into the electroweak force. Each of these forces has its own mediator, the gluon belonging to the strong force, the photon to the electromagnetic force, the $W^\pm$ and Z to the weak force, and the graviton to the gravitational force. These mediators are the ones that transmit a force between a quark or lepton to another quark or

letpon. The strong force has the most "strength", decreasing in strength in order to the weakest one of gravity.

The strong interaction is described by *QuantumChromodynamics* and is one of the compoments of the $SU(3) \otimes SU(2) \otimes U(1)$ of the Standard Model. It is the force that holds atomic nuclei together. A single quark of a specific flavor may come in three colors. The SU(3) symmetry group has 8 gluons (massless mediators). This force allows for hadrons to be made of quark composites.

The Electromagnetic interaction is described by *QuantumElectrodynamics* and its force is carried by the mediating massless photon, represented by the U(1) symmetry group. The weak interaction is described by the SU(2) symmetry group. Its force is mediated by the $W^{\pm}$ and Z^0, massive intermediate vector bosons. A gauge theory unifying the electromagnetic and weak interactions was proposed in 1967 by Salam, Weinberg, and Glashow [5, 6, 7]. In this theory, named the *Electroweak* theory, the forces obey the $SU(2) \otimes U(1)$ gauge symmetry.

1.2 Some Basic Facts about Hyperons

Hyperons are the class of baryons containing strange quarks. The lowest mass hyperons decay through the weak interaction, with strangeness changing by ± 1, and all have the long lifetime, 10^{-10} sec., associated with weak decays. The only exception is the decay $\Sigma^{\circ} \rightarrow \Lambda^{\circ}\gamma$, which is an electromagnetic decay and has a lifetime $(7.4 \pm 0.7) \times 10^{-20}$ sec [9]. Table 1.2 shows the lowest mass hyperons, their quark content, the dominant decay modes with their branching fractions or ratios, and the weak radiative decay modes.

Table 1.1: Quarks and Leptons[8]

Particle Name	Symbol	Electric Charge	$Mass(Gev/c^2)$
Up	u	$+2/3$	0.0015 to 0.0045
Down	d	-1/3	0.005 to 0.0085
Charm	c	$+2/3$	1.0 to 1.4
Strange	s	-1/3	0.080 to 0.155
top	t	$+2/3$	$174.3\pm$ 5.1
Strange	s	-1/3	4.0 to 4.5
Particle Name	Symbol	Electric Charge	$Mass(Mev/c^2)$
Electon	e	-1	0.510999
Electon Neutrino	ν_e	0	$<$0.000003
muon	μ	-1	105.658
Muon Neutrino	ν_μ	0	$<$0.19
tau	τ	-1	$1776.99^{+0.29}_{-0.26}$
Tau Neutrino	ν_τ	0	$<$18.2

The dominant weak decay modes always involve a baryon and a meson in the final state. For the radiative decays, a photon is emitted. 2-body radiative decays look less complex. They involve only a single baryon in the initial and final states, and a photon is emitted. Precisely how the decays occur, however, is not at all obvious. The parent and daughter particles in the hyperon radiative decays differ in makeup by only one quark: a strange quark appears to have converted into a down quark plus a γ. The modern interpretation of this kind of hyperon radiative decay has been dominated by the results of ref. [10]. In that paper, Gilman and Wise present an elegant analysis using $s \rightarrow d\gamma$.

3-body radiative decays are much more complicated, and little theoretical work has been performed.

Table 1.2: Properties of Hyperons [8]

Hyperon(Gev/c^2)	T(sec)	Quarks	Dom. Modes(B.R.)	Rad. Mode
Λ° (1.1157)	2.632×10^{-10}	uds	$\begin{matrix} p\pi^- \\ n\pi^0 \end{matrix}$ $\begin{pmatrix} 63.9\% \\ 35.8\% \end{pmatrix}$	$\begin{matrix} n\gamma \\ p\pi^-\gamma \end{matrix}$
Σ^+ (1.1894)	0.8×10^{-10}	uus	$\begin{matrix} p\pi^0 \\ n\pi^+ \end{matrix}$ $\begin{pmatrix} 51.57\% \\ 48.31\% \end{pmatrix}$	$\begin{matrix} p\gamma \\ n\pi^+\gamma \end{matrix}$
Σ^0 (1.1193)	7.4×10^{-20}	uds	$\Lambda^0\gamma$ (100%)	NA
Σ^- (1.1974)	1.479×10^{-10}	dds	$n\pi^-$ (99.848%)	$n\pi^-\gamma$
Ξ° (1.3148)	2.9×10^{-10}	uss	$\Lambda^0\pi^\circ$ (99.522%)	$\begin{matrix} \Lambda^0\gamma;\Sigma^0\gamma \\ \Lambda^0\pi^\circ\gamma \end{matrix}$
Ξ^- (1.3213)	1.639×10^{-10}	dss	$n\pi^-$ (99.887%)	$\Sigma^-\gamma$
$\Omega-$ (1.6725)	0.821×10^{-10}	sss	$\begin{matrix} \Lambda^0 K^- \\ \Xi^0\pi^- \end{matrix}$ $\begin{pmatrix} 67.8\% \\ 23.6\% \end{pmatrix}$	$\Xi^-\gamma$

1.3 Phenomenology of $\Xi^\circ \to \Lambda^\circ\pi^\circ$

The dominant weak hyperon decay modes usually involve a baryon and a meson in the final state. A strange quark (s) in the parent hyperon converts into an up (u) or a down (d) quark. For all spin-$\frac{1}{2}$ hyperons [1], except for Σ° which decays electromagnetically, all have a π meson in the final state, and therefore the decays are usually represented by $B \to B'\pi$, where B and B' are initial and final state baryons. In our case (the mode $\Xi^\circ \to \Lambda^\circ\pi^\circ$ is our normalization mode), we will discuss the phenomenology here.

When a spin-$\frac{1}{2}$ hyperon decays nonleptonically, the daughter baryon is also a spin-$\frac{1}{2}$ particle while the daughter meson has spin zero. Conservation of angular momentum implies this Hamiltonian is restricted to having only $l = 0$ (s-wave) and $l = 1$ (p-wave) components. For $\Xi^\circ \to \Lambda^\circ\pi^\circ$ the most general decay amplitude that satisfies Lorentz invariance must be a sum of scalar and pseudoscalar quantities and can be written [11]

$$\mathcal{M} = \overline{u}_{\Lambda^\circ}(A + B\gamma_5)u_{\Xi^\circ} \tag{1.1}$$

where A and B are the s-wave and p-wave amplitudes respectively. Since the final state pion is a pseudoscalar and has negative parity, the $\overline{u}_{\Lambda^\circ}B\gamma_5 u_{\Xi^\circ}$ term which is also a pseudoscalar is called the parity conserving amplitude. The term $\overline{u}_{\Lambda^\circ}Au_{\Xi^\circ}$ is a scalar and has a positive parity and is called the parity violating amplitude.

We now define $s = A$ and $p = (E_{\Lambda^\circ} - M_{\Lambda^\circ})/(E_{\Lambda^\circ} + M_{\Lambda^\circ})B$ for the s-wave and p-

[1] not exactly for Ω^- in Table 1.2

wave parts. s and p have the advantage that they appear in an analogous manner in the decay rate and asymmetry formulae. E_{Λ° and M_{Λ° are the energy and and mass of Λ° in the rest frame of Ξ°. Using these definitions and equation 1.1 the decay rate becomes [8, 12, 13]

$$\Gamma = \frac{\mid q \mid}{4\pi}(\mid s \mid^2 + \mid p \mid^2)\frac{(E_{\Lambda^\circ} + M_{\Lambda^\circ})}{M_{\Xi^\circ}} \tag{1.2}$$

where M_{Ξ° is the Ξ° mass and $\mid q \mid$ is the momentum transfer of the decay.

Other quantities of interest are the so called decay asymmetry parameters which describe the angular distribution of Λ° and its polarization. The decay parameters can be written in terms of s and p amplitudes

$$\alpha_{\Xi^\circ} = \frac{2Re(s^*p)}{\mid s \mid^2 + \mid p \mid^2} \tag{1.3}$$

$$\beta_{\Xi^\circ} = \frac{2Im(s^*p)}{\mid s \mid^2 + \mid p \mid^2} \tag{1.4}$$

$$\gamma_{\Xi^\circ} = \frac{\mid s \mid^2 - \mid p \mid^2}{\mid s \mid^2 + \mid p \mid^2}, \tag{1.5}$$

with the normalization condition $\alpha^2 + \beta^2 + \gamma^2 = 1$. The angular distribution of the Λ° in the rest frame of Ξ° can be written as:

$$\frac{1}{\Gamma}\frac{d\Gamma}{d\Omega} = \frac{1}{4\pi}(1 + \alpha_{\Xi^\circ}\vec{P_{\Xi^\circ}} \cdot \hat{p}_{\Lambda^\circ}) \tag{1.6}$$

where $\vec{P_{\Xi^\circ}}$ is the polarization of Ξ° and $\hat{p}_{\Lambda^\circ}$ is a unit vector along the momentum direction of the Λ° in the rest frame of Ξ°. It is known that some hyperons are produced with a significant polarization [14, 15, 16].

The polarization of the daughter baryon in its own rest frame is

$$\vec{P_{\Lambda^\circ}} = \frac{(\alpha_{\Xi^\circ} + \vec{P_{\Xi^\circ}} \cdot \hat{p}_{\Lambda^\circ})\hat{p}_{\Lambda^\circ} + \beta_{\Xi^\circ}(\vec{P_{\Xi^\circ}} \times \hat{p}_{\Lambda^\circ}) + \gamma_{\Xi^\circ}[\hat{p}_{\Lambda^\circ} \times (\vec{P_{\Xi^\circ}} \times \hat{p}_{\Lambda^\circ})]}{1 + \alpha_{\Xi^\circ}\vec{P_{\Xi^\circ}} \cdot \hat{p}_{\Lambda^\circ}} \tag{1.7}$$

which simplifies to

$$\vec{P_{\Lambda^0}} = \alpha_{\Xi^0} \hat{p}_{\Lambda^0}, \tag{1.8}$$

if the parent hyperon Ξ° is unpolarized. Note that a polarization vector is only simply well defined in the rest frame of the polarized particle, and so the polarization terms in the left hand side of the above equations are measured in the daughter particle Λ° rest frame, while those on the right hand side are measured in the rest frame of the decaying particle Ξ°.

Experimental measurements of β and γ are difficult, requiring measurement of both parent and daughter polarization. However, the measurement of α can be made simple, in the case when the daughter baryon itself decays.

The Λ decays in turn to a proton and π^-, with the proton distribution given by the form of equation 1.6

$$\frac{1}{\Gamma}\frac{d\Gamma}{d\Omega} = \frac{1}{4\pi}(1 + \alpha_{\Lambda^0} \vec{P_{\Lambda^0}} \cdot \hat{p}_p) \tag{1.9}$$

This equation is independent of ϕ angle and can be integrated over this angle. Therefore, using equation 1.8, equation 1.9 can be rewritten as

$$\frac{1}{\Gamma}\frac{d\Gamma}{d(cos\theta)} = \frac{1}{2}(1 + \alpha_{\Lambda^0}\alpha_{\Xi^0} \hat{p}_p \cdot \hat{P}_{\Lambda^0}) \tag{1.10}$$

where $\hat{P}_{\Lambda^0}$ is the unit vector in the direction of Λ^0 polarization in the Λ rest frame. The decay parameter product $\alpha_{\Lambda^0}\alpha_{\Xi^0}$ is extracted by measuring the slope of the decay angle θ distribution in the Λ^0 rest frame.

1.4 2-Body Weak Radiative Hyperon Decays

The two-body weak radiative decays [12] of spin 1/2 hyperson, $B_i \to B_f\gamma$, yield information about matrix elements (form factors) similar to that gained from weak hadronic decays. For a polarized spin 1/2 hyperon decaying radiatively via a $\Delta Q = 0$, $\Delta S = 1$ transition, the angular distribution of the direction $\hat{\mathbf{p}}$ of the final spin 1/2 baryon in the hyperon rest frame is

$$\frac{dN}{d\Omega} = \frac{N}{4\pi}(1 + \alpha_\gamma \mathbf{P_i} \cdot \hat{\mathbf{p}}) \tag{1.11}$$

Here $\mathbf{P_i}$ is the polarization of the decaying hyperon, and α_γ is the asymmetry parameter. In terms of the form factors $F_1(q^2)$, $F_2(q^2)$, and $G(q^2)$ of the effective hadronic weak electromagnetic vertex,

$$F_1(q^2)\gamma_\lambda + iF_2(q^2)\sigma_{\lambda_\mu}q^\mu + G(q^2)\gamma_\lambda\gamma_5 \tag{1.12}$$

α_γ is:

$$\alpha_\gamma = \frac{2Re[G(0)F_M^*(0)]}{|G(0)|^2 + |F_M(0)|^2} \tag{1.13}$$

where $F_M = (m_i - m_f)[F_2 - F_1/(m_i + m_f)]$. If the decaying hyperon is unpolarized, the decay baryon has a longitudinal polarization given by $P_f = -\alpha_\gamma$ [17].

The angular distribution for the weak hadronic decay, $B_i \to B_f\pi$, has the same form as Equation 1.11, but of course with a different asymmetry parameter, α_π. Now, however, if the decaying hyperon is unpolarized, the decay baryon has a logitudinal polarization given by $P_f = +\alpha_\pi$. The difference of sign is because the spins of the pion and photon are different.

This kind of two-body weak radiative decay applies to modes like $\Xi^\circ \to \Sigma^\circ\gamma$ which was studied in KTeV for branching ratio and asymmetry measurement [4]. Also it applies to the mode $\Xi^\circ \to \Lambda^\circ\gamma$. A measurement of $\Xi^\circ \to \Lambda^\circ\gamma$ decay rate was reported in 1990, with 115 signal events [18]. The measurement of the branching ratio and asymmetry differed from the expectation at the 1σ level. KTeV collected about 1100 of these events at KTeV during the E799 winter run (Fig 1.1).

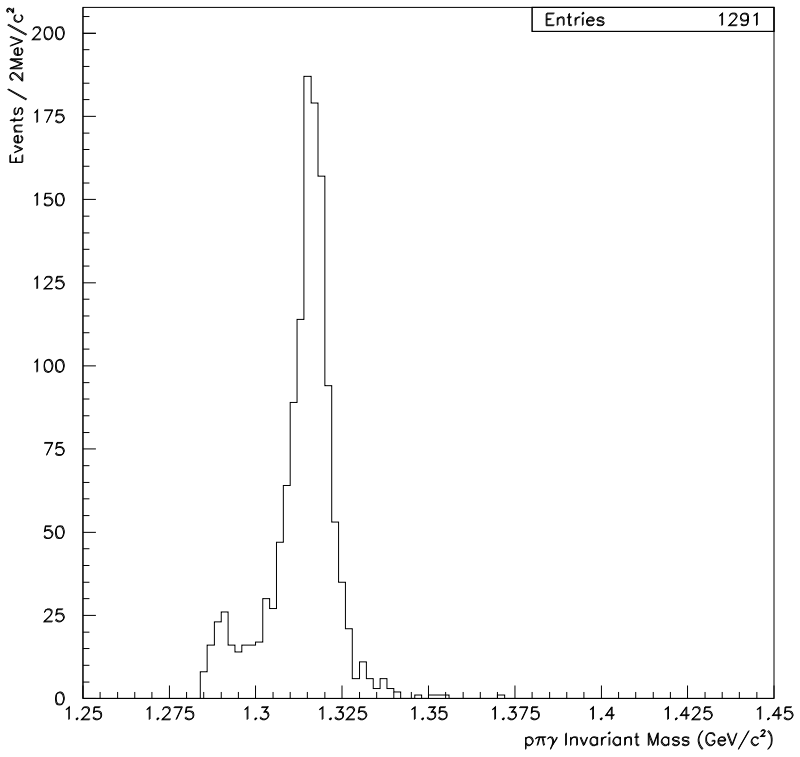

Figure 1.1: The radiative decay of $\Xi^\circ \to \Lambda^\circ\gamma$ for the E799-II winter run.

1.5 2-Body WRHD Experimental Results Prior to 2002

The hyperon readiative decays have been of theoretical interest for some time, because of their simplicity compared to other hyperon decays. The experimental data, however, have been sparse, so there are not many checks on the prediction from any models.

The first measurements for $\Sigma^+ \to p\gamma$ were done using bubble chambers by Gershwin and others [1] in 1969. They got the Branching Ratio $(1.91 \pm 0.4) \times 10^{-3}$ and the large asymmetry number $\alpha_\gamma = -1.03^{+0.54}_{-0.42}$. This was the first evidence for large negative asymmetry which was contrary to the expectation based on Hara's theorem [2].

In the past 40 years, only several weak radiative hyperon decays were well studied. The Table 1.3 shows the experimental results up to 2004 [8] from Particle Data Book .

The KTeV neutral beam contained a copious amount of neutral hyperons which made KTeV an unique facility to study these rare decays. The importance of a good theoretical understanding of the weak radiative decays has been empahsized by some physicists [18]. The analysis of these decays invloves putting the strong QCD, weak interaction, and electromagnetic interaction together. It is crucial to understand how they fit together in a process that we can study in detail.

Table 1.3: 2-body WRHD Experimental Results Prior to 2002 [8]

Mode	$\frac{No.of}{Events}$	$\frac{Branching}{Ratio(10^{-3})}$	$\frac{Asymmetry}{parameter}$	Laboratory
$\Sigma^+ \to p\gamma$	24	1.91 ± 0.41		BNL(1965)
	31(61)	1.42 ± 0.26	$-1.03^{+0.54}_{-0.42}$	Berkeley (1969)
	45	1.08 ± 0.15		CERN (1969)
	30(46)	1.09 ± 0.20	$-0.53^{+0.38}_{-0.36}$	CERN (1980)
	155	$1.27^{+0.15}_{-0.18}$		CERN (1985)
	190	1.30 ± 0.15	$-0.86 \pm 0.13 \pm 0.04$	KEK (1987)
	408	1.45 ± 0.20		BNL (1989)
	35K		$-0.720 \pm 0.086 \pm 0.045$	Fermilab (1992)
	32K	1.26 ± 0.06		Fermilab (1995)
$\Xi^- \to \Sigma^-\gamma$	9	0.23 ± 0.10		CERN(1987)
	211	0.122 ± 0.023	1.0 ± 1.3	Fermilab(1994)
$\Xi^\circ \to \Sigma^\circ\gamma$	4045	3.35 ± 0.10	-0.63 ± 0.09	Fermilab(2001)
$\Xi^\circ \to \Lambda^\circ\gamma$	672	1.17 ± 0.07	-0.78 ± 0.18	NA48(2004)
$\Lambda^0 \to n\gamma$	24	1.02 ± 0.33		CERN(1986)
	287	1.78 ± 0.24		BNL(1992)
	1816	1.75 ± 0.15		BNL(1993)
$\Omega^- \to \Xi^-\gamma$		< 2.2 at 90% C.L.		CERN(1984)
		< 0.46 at 90% C.L.		Fermilab(1994)

1.6 3-Body Weak Radiative Hyperon Decay $\Xi^\circ \to \Lambda^\circ\pi^\circ\gamma$

In this three body Weak Radiative Hyperon decay $\Xi^\circ \to \Lambda^\circ\pi^\circ\gamma$, both the initial and final state particles are neutral, and thus a simple inner bremsstrahlung process is presumably not applicable. This means that the branching rate is dominated by some other processes. No previous observation or limit has been placed on this decay [2] and there is no published theoretical work.

From an extensive search we did based on the Particle Data Book, the decay mode $\Xi^\circ \to \Lambda^\circ\pi^\circ\gamma$ seems to be the only examle of a weak (long lifetime) decay that is all-neutral and which has a corresponding allowed non-radiative decay (e.g. $\Xi^\circ \to \Lambda^\circ\pi^\circ$).

The major problem in any of these experiments is to separate the rare radiative decay mode from a background of one or more of the dominant decay modes. The task is made more difficult by the fact that the radiative and dominant decay modes often differ by only a single daughter particle; in our case they differ by a γ, 1 extra gamma from the radiative decay in addition to two γ's from a π°. An experiment's ability to separate the radiative decays from a background of the dominant decays will depend on the design of the experiment.

For decay mode $\Xi^\circ \to \Lambda^\circ\pi^\circ\gamma$, the γ directly from Ξ° has pretty small momentum space. In the CM system of Ξ°, we have 4-vector momentum conservation equation.

$$P_{\Xi^\circ}(M_{\Xi^\circ}, \vec{0}) = P_{\Lambda^\circ} + P_{\pi^\circ} + P_\gamma \tag{1.14}$$

[2] This decay is not listed in PDG [8]

For the extreme case, we have the $P_\gamma \leq 63MeV$. Based on this maximum P_γ, we can make some guess further. For a "stable" particle, the radius is:

$$r = 1.4fm. \tag{1.15}$$

$$\Delta P \Delta x = \hbar \tag{1.16}$$

$$\Delta Pc = \frac{\hbar c}{\Delta x} \approx 140MeV \tag{1.17}$$

This means that a γ with less than 140 MeV momentum cannot probe less than about 1.4 fm. If we require the smaller size of the particle, the corresponding momentum will be much larger than 60 MeV. This rough calculation gives us an impression that the possibility that the γ sees the quarks inside the Ξ° is low.

Fig 1.2 shows us some possible Feyman Quark Diagrams for the decay mode which I am trying to observe. Because our photon has such low energy, these may not play a significant role in our decay.

If might consider this decay mode at the particle level. From Particle Data Book, we know that the Ξ° has the magnetic moment $\mu = -1.250\mu_N$, and the Λ° has the magnetic moment $\mu = -0.613\mu_N$. The change of the magnetic moment during the decay process can possibly radiate a γ. Fig 1.3 shows us a possible decay diagram at the particle level. You can also see the reference [3] by Lach and Zenczyskowski for a discussion about this.

The KTeV experiment was not designed initially to detect a rare hyperon radiative decay. Experiment 799 at Fermilab was a measurement of CP violation of kaons. However, a copious amount of neutrons, and some very high momentum hyperons entered the detector along with K_L's. The Λ° and Ξ° were the only two

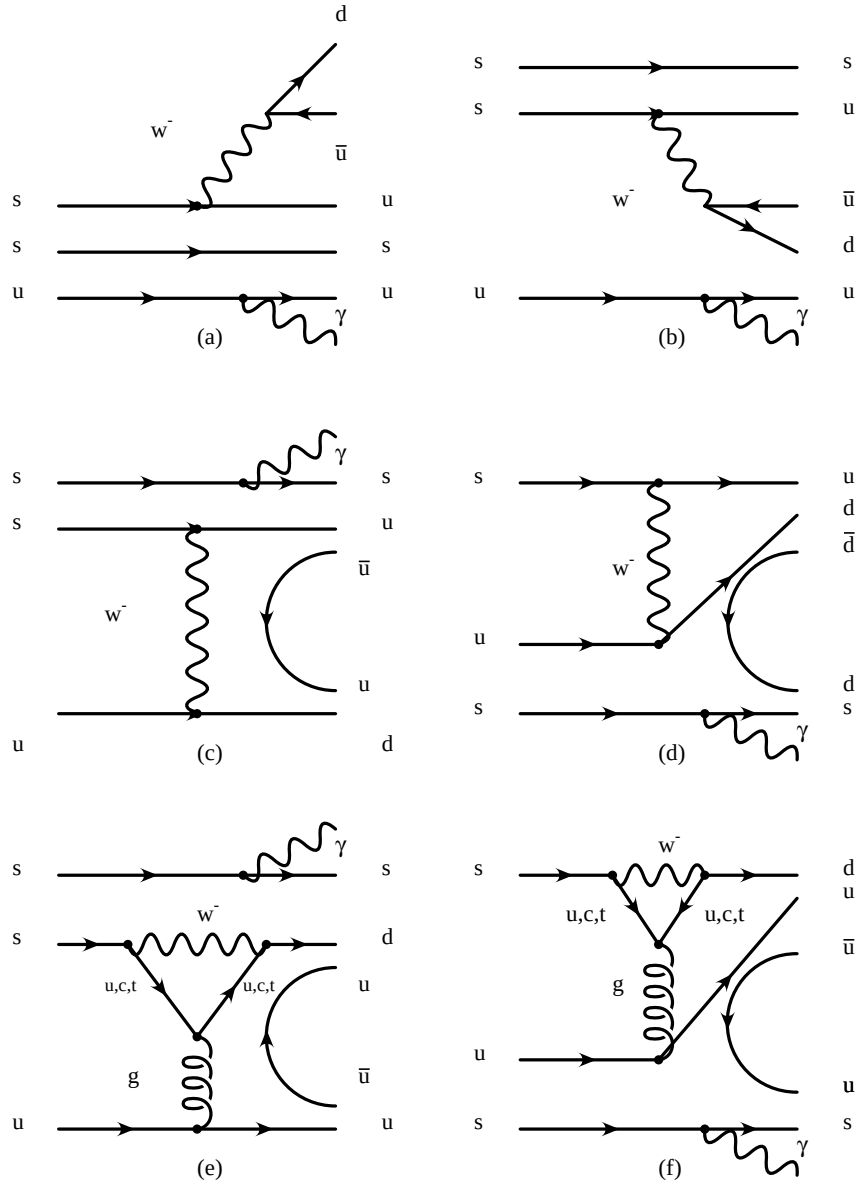

Figure 1.2: Feyman Quark Diagram for $\Xi^\circ \rightarrow \Lambda^\circ\pi^\circ\gamma$

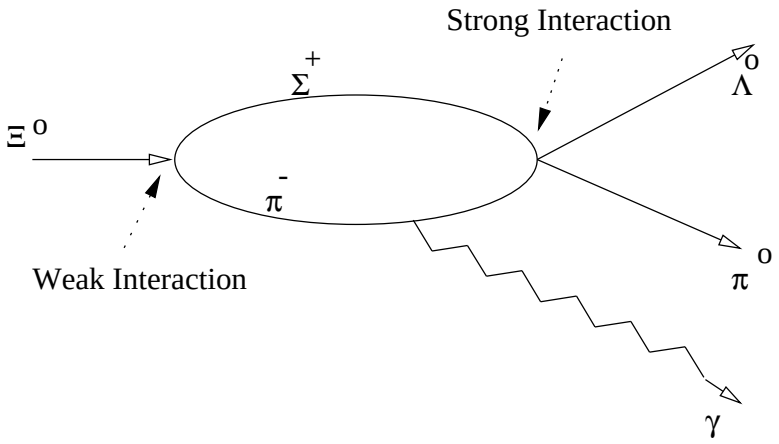

Figure 1.3: A Possible Particle Level Digram for $\Xi^\circ \rightarrow \Lambda^\circ\pi^\circ\gamma$

neutral hyperons with lifetimes long enough to be observable at KTeV. Table 1.4 presents a list of some hyperon topics which have been studied at KTeV.

Table 1.4: Neutral hyperon program at KTeV. N_{event} is the number of events observed in the previous experiments and N_{KTeV} is the number of candidates at KTeV.

Decay mode	N_{event}	N_{KTeV}	Physics Interest
$\Xi^0 \to \Sigma^+ e^- \bar{\nu}_e$	0	1100	BR, Form Factors
$\bar{\Xi}^0 \to \bar{\Sigma}^+ e^+ \nu_e$	0	66	BR, Form Factors
$\Xi^0 \to \Sigma^+ \mu^- \bar{\nu}_\mu$	0	5	BR
$\Xi^0 \to \Lambda\pi^0,\ \Lambda \to p e^- \bar{\nu}_e$	Many	6000	Form Factors
$\Xi^0 \to \Lambda\pi^0,\ \Lambda \to p \mu^- \bar{\nu}_\mu$	28	NA	BR, Form Factors
$\Xi^0 \to \Sigma^0\gamma$	85	7000	BR, Asymmetries
$\Xi^0 \to \Lambda\gamma$	116	1000	BR, Asymmetries
$\Xi^0 \to \Lambda\pi^0\gamma$	0	NA	BR
$\Lambda^0 \to p\pi^-\gamma$	72	7000	BR
$\Sigma^0 \to \Lambda e^+ e^-$	314	10	BR, Σ^0 Parity
$\Sigma^0 \to \Lambda\gamma\gamma$	0	NA	BR
$\Xi^0 \to \Lambda\pi^0$ and $\bar{\Xi}^0 \to \bar{\Lambda}\pi^0$	Many	Many	Precise mass, Polarization
$\Xi^0 \to p\pi^-,\ \bar{\Xi}^0 \to \bar{p}\pi^+$	0	0	$\Delta S = 2$ (SM test)

Chapter 2

The beamline and KTeV detector

KTeV is the name given to a collaboration of two different experiments: E799 and E832. The E832 experiment was built to measure direct CP violation in $K_{L,S} \to \pi^+\pi^-$ and $K_{L,S} \to \pi^\circ\pi^\circ$ decays. The E799 experiment was designed to look at rare $K_{L,S}$ decays. Since there are also a large number of Ξ° and Λ° produced (and their anti-particles), decays such as $\Xi^\circ \to \Lambda^\circ\pi^\circ$, and the radiative decay modes $\Xi^\circ \to \Lambda^\circ\gamma$, $\Xi^\circ \to \Sigma^\circ\gamma$ can also be studied in E799.

To accomplish these purposes, the KTeV detector facility was designed to produce a neutral beam of $K_{L,S}$ and hyperons, to reconstruct the momenta of the decay products of the $K_{L,S}$ and hyperons, and to detect decay products escaping or staying in the detector volume.

The KTeV experimental facility is located parallel to the neutrino-muon (NM) beam-line at the Fermi National Accelerator Laboratory (Fermilab) in Bativia, Illinois. The data used in this analysis were recorded between September 1999 and January 2000.

2.1 The Beamline

2.1.1 Proton Beam

A diagram of the KTev secondary beam system[20] appears in Fig. 2.1. The Fermi National Accelerator Laboratory (Fermilab, or FNAL) Tevatron provided a beam[19] consisting of 800 GeV protons with a 23 second period "spill", approximately once every minute. With each spill, there was a 53 MHz "bucket" structure due to the accelerator radio frequency (RF) of the Tevatron. The buckets were separated by 19 nsec, and the protons arrived in a 2 nsec period at the beginning of each bucket. Over an entire spill 2.5×10^{12} protons arrive at KTeV's target in the Neutrino Muon beam line.

2.1.2 Target and KTeV Coordinate System

When protons reach KTeV, they hit the beryllium oxide target which was 30.5 cm long ($\sim$ 0.9 nuclear interaction lengths) with a cross section of $3.0mm \times 3.0mm$ [20]. BeO is used (instead of, say, copper or tungsten) because of its resistence to the thermal stressses of the proton beam enviroment and its large production ratio of K°/n. The targeting angle was chosen to be 4.8 mrad in the vertical plane so that we could eliminate most of neutrons from the beam and still maintain a high neutral kaon flux to reach the decay volume of the experiment. The center of the target forms the origin of the KTeV coordinate system. The positive Z axis extends from the target towards the detector. +Z is referred to as "downstream" while -Z is "upstream". The positive Y direction points vertically up, and the positive X direction is defined in the conventional ($\vec{y} \times \vec{z} = \vec{x}$).

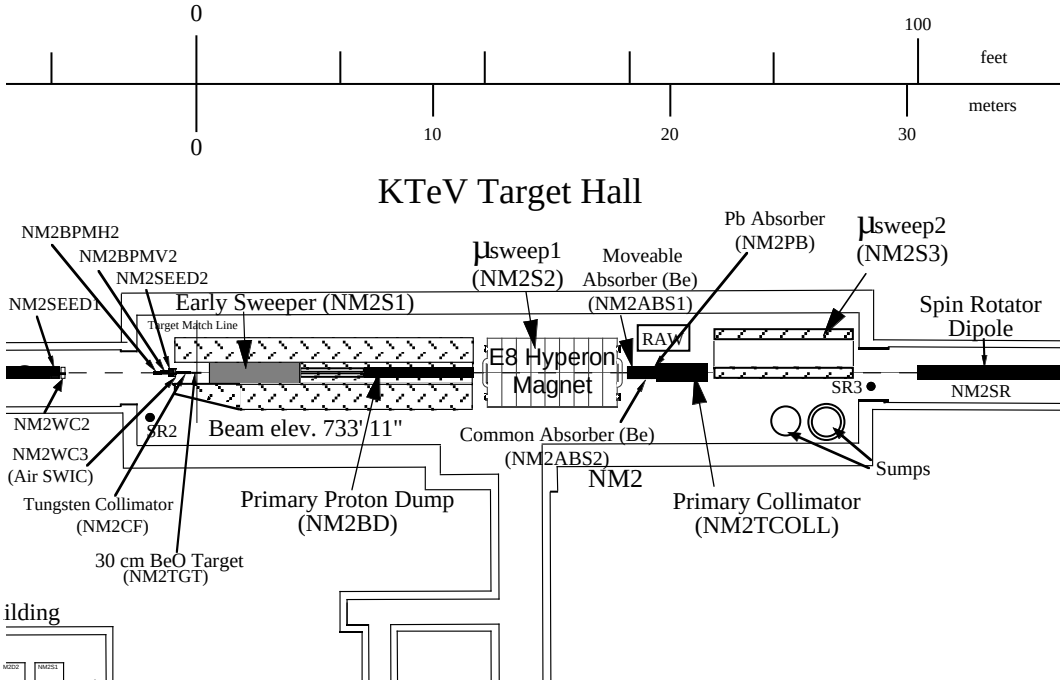

Figure 2.1: Schematic plan view of the collimation and sweeping system.

2.1.3 Sweeping Magnet, Absorbers

In order to purify the beam, charged and some neutral particles, like the neutron, must be removed from the beam. This is achieved by a series of sweepers and absorbers. Absorbers are placed in the beam mainly to remove neutrons and photons.

In Fig. 2.1, one can see there are several sweeping magnets, The "Sweeper" magnetic fields were used to deflect charged particles out of the beam. The first sweeper magnet with the +Y field direction is the Target Sweeper, which operated between about 0.6 and 4.4 meters in Z, and gave primary protons a momentum kick of $475 MeV/c$. Downsteam of the Target Sweeper was Primary Proton Dump, which absorbed primary-beam protons. It was located between 7.2 and 11.8 meters in Z, water cooled, and made of copper. The target Sweeper deflected protons into the Dump. The other sweeping magnets are desinged basically to remove muons from the kaon beam. The μ-sweeper-1 followed the traget Sweeper, between 12.3 and 17.8 meters in Z, its field is also in the +Y direction. The photons from the target are absorbed by a layer of lead 3 inches (14 X_0) thick at Z=19m, it was called the "Pb" Absorber. The μ-sweeper-2, between 21.9 and 27.7 meters in Z with its field also in +Y direction, removed the particles created by interactions in the lead absorber and the primary collimator. The latter will be introduced in the next subsection. Detailed discussions of the design specifications of the sweepers are to be found in [21].

2.1.4 Collimating System

The Collimating system in Fig. 2.2 included Primary Collimator, Slab Collimator and Defining Collimator. It defined the beams in the transverse direction with increasing precision. The primary collimator at Z=20m was made of brass and had two tapered rectangular cylinders cut through it to create and shape roughly the two kaon beams. The centers of the two beams are separated by 1.6 mrad with respect to the ratget. The next collimator is the slab collimator at Z=38 m. It was a single wedge of stainless steel and sat between the two beams. It prevented the particles from crossing one beam into the other. The last element defining the beams was the defining collimator. It was at Z=85 m and had a similar geometry to the Primary Collimator but was made of iron. It defined the beam shape and set the beam divergence at 0.8 mrad.

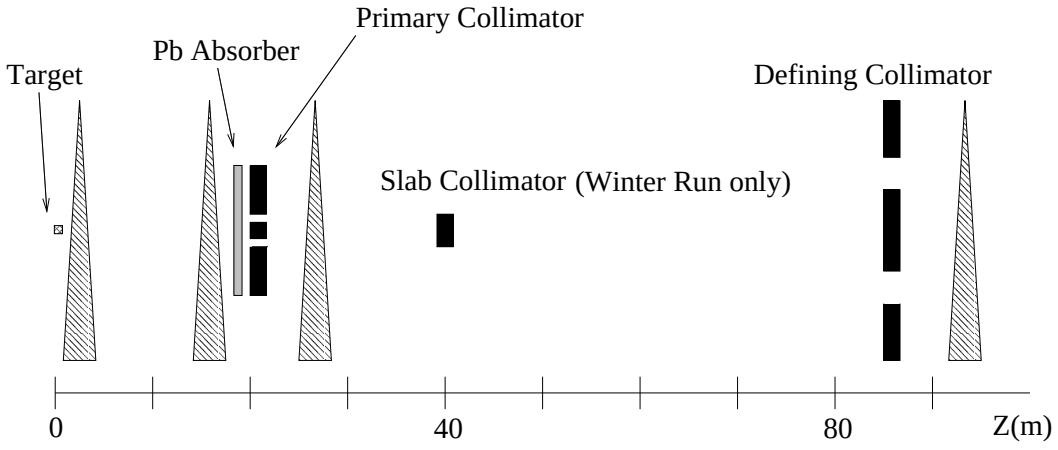

Figure 2.2: Schematic plan view of the collimation system.

2.1.5 Spin rotator magnet

For the hyperon study the spin of the particle is also very important. The 3 manget sweepers served the dual purpose of precessing the spin of the Ξ° produced at the target. The direction of the incoming proton beam is:

$$\vec{p} \simeq \vec{z} - 4.8 \times 10^{-3}\vec{y} \tag{2.1}$$

$$\vec{\Xi^\circ} \simeq \vec{z} \tag{2.2}$$

Since Ξ° are produced by the strong interaction, which conserves parity, the Ξ° can only be polarized along $\vec{p} \times \vec{\Xi^\circ}$, that is along $\vec{x}$ axis.

Once the Ξ°'s reached the Spin Rotator, they were polarized in the z direction. The magnetic field of Spin Rotator magnet was along the X axis (This is different from the other 3 Sweepers). It precessed the Ξ° spin into the $\pm y$ direction, depending on the polarity, which was switched regularly to obtain equal amounts of data for the two polarization directions. Spin Rotator had no effect on the mesons, like kaons.

2.1.6 The Secondary Beam

After passing all the beam parts, short lived particle in the neutral beam, like $K_S(c\tau \sim 2.7cm)$ and to a lesser extent $\Lambda^\circ(c\tau \sim 7.9cm)$ and $\Xi^\circ(c\tau \sim 8.7cm)$, decayed before reaching the decay volume of the experiment about 94 m downstream of the target. It enhanced the percentage of $K_L(c\tau \sim 15.5m)$. Flux calculations show the number of Λ and Ξ° reaching the decay volume were approximately 2% and 0.2% of the number of K_L's respectively, the ratio of numtrons to the number of K_L's was about 3 for E799 beam.

Due to their short life time, only high momentum Λ° and Ξ° survived into the decay volume. Figure 2.3 shows the momentum spectrum of Ξ° in the decay volume of the experiment.

Detailed discussions of the design specifications of the KTeV secondary beam are to be found in [22, 23]

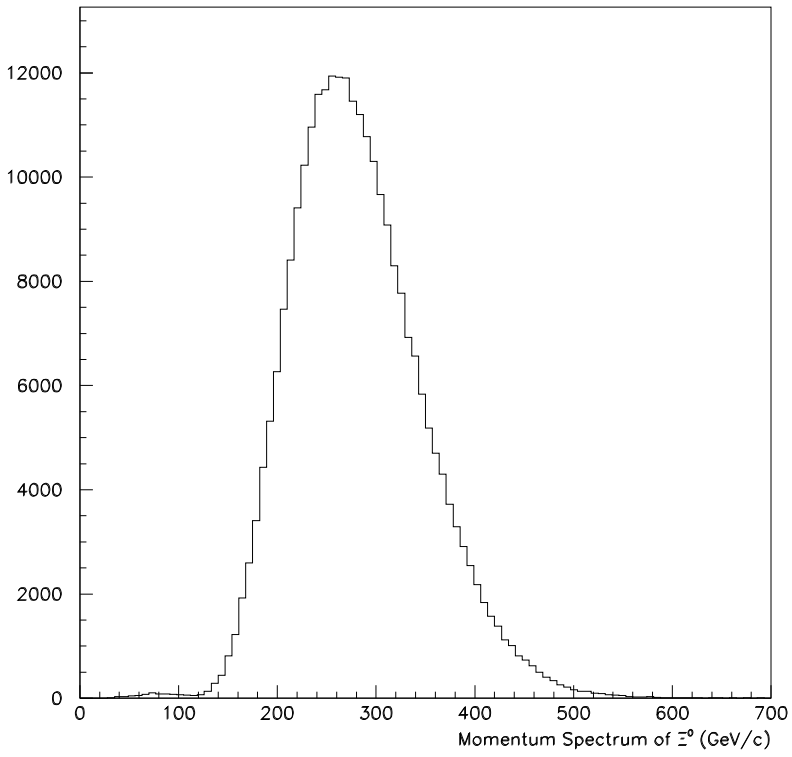

Figure 2.3: The momentum spectrum of Ξ°particle. Only high momentum hyperons reach the KTeV detector. The kaon spectrum peaks at about 40 GeV/c.

2.2 The Main E799 Detector Brief Introduction

An overview of the detector is shown in in Fig. 2.4 and Fig. 2.5. Beginning upstream, there was the decay region and ring vetoes. Next comes the charged-particle spectrometer (including 4 Drift Chambers, and 1 Analyzing magnet) and its accompanying vetoes. They are followed by the TRD system (e^-/π^- discrimination). In front of the Cesium-Iodide calorimeter there was a pair of scintillator hodoscopes to trigger the events. Downstream of that are more vetoes, including the muon system. Also listed in Table 2.1 are the z positions and the transverse dimensions of the detector elements most relevant for hyperon analysis.

The first part of the main detector is a 65 m vacuum tank, which was from Z=93.0 m to Z=158.9 m. It started as a 45.73 cm diameter vacuum pipe and grew progressively larger downstream to a size of 243.84 cm in diamster. The pressure inside the tank was maintained at 10^{-6} torr to reduce the interactions between the neutral beam particles and any surounding matter and to reduce scattering of the charged decay products. A strong but thin mylar-kevlar window is placed at the downstream end of the decay region to prevent air from leaking in. The window is 0.0015 radiation lengths thick.

2.3 The Spectrometer

The purpose of the spectrometer is to measure the momentum and postion of charged particles, as part of event reconstructing. This is done with a set of four drift chambers (DC's), two on each side of the analyzing magnet as shown in Figs. 2.4 and 2.5. Helium bags were placed between the drift chambers to reduce

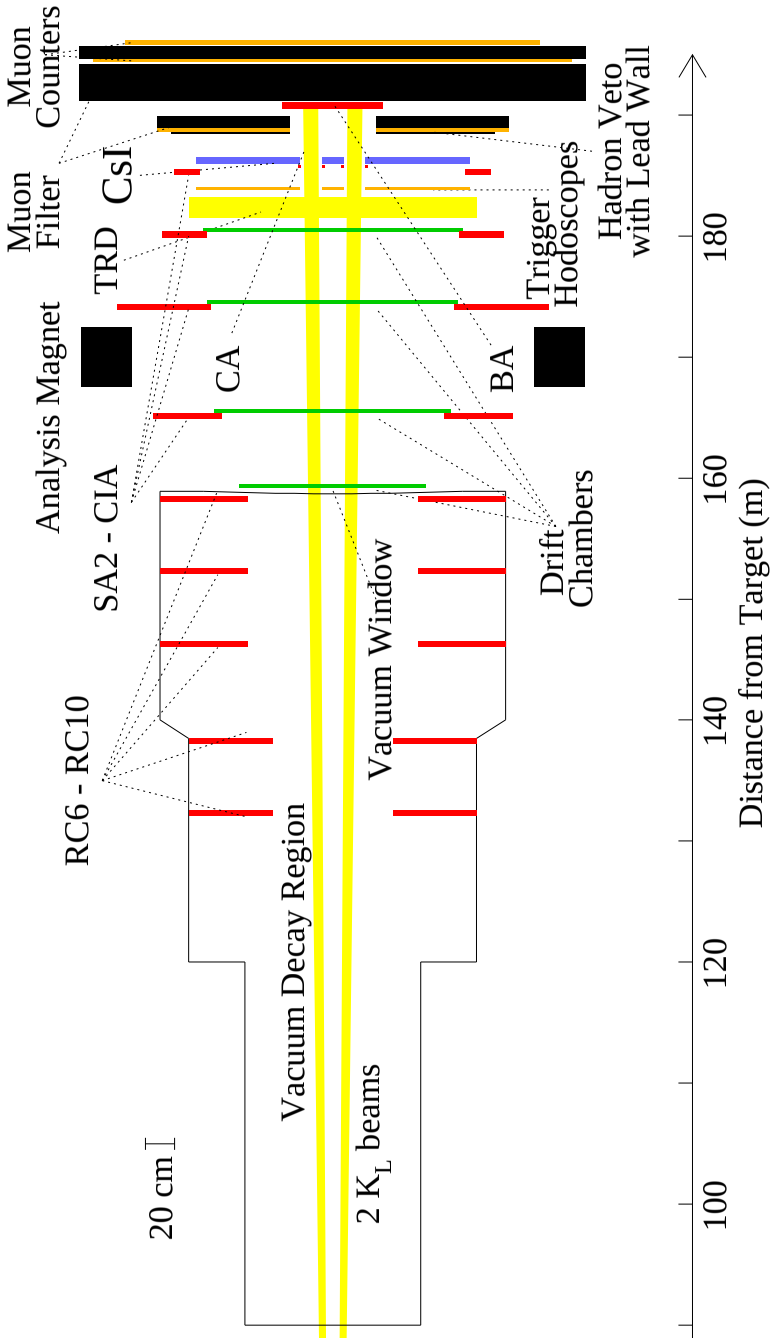

Figure 2.4: Schematic drawing of KTeV detector (E799), not in scale.

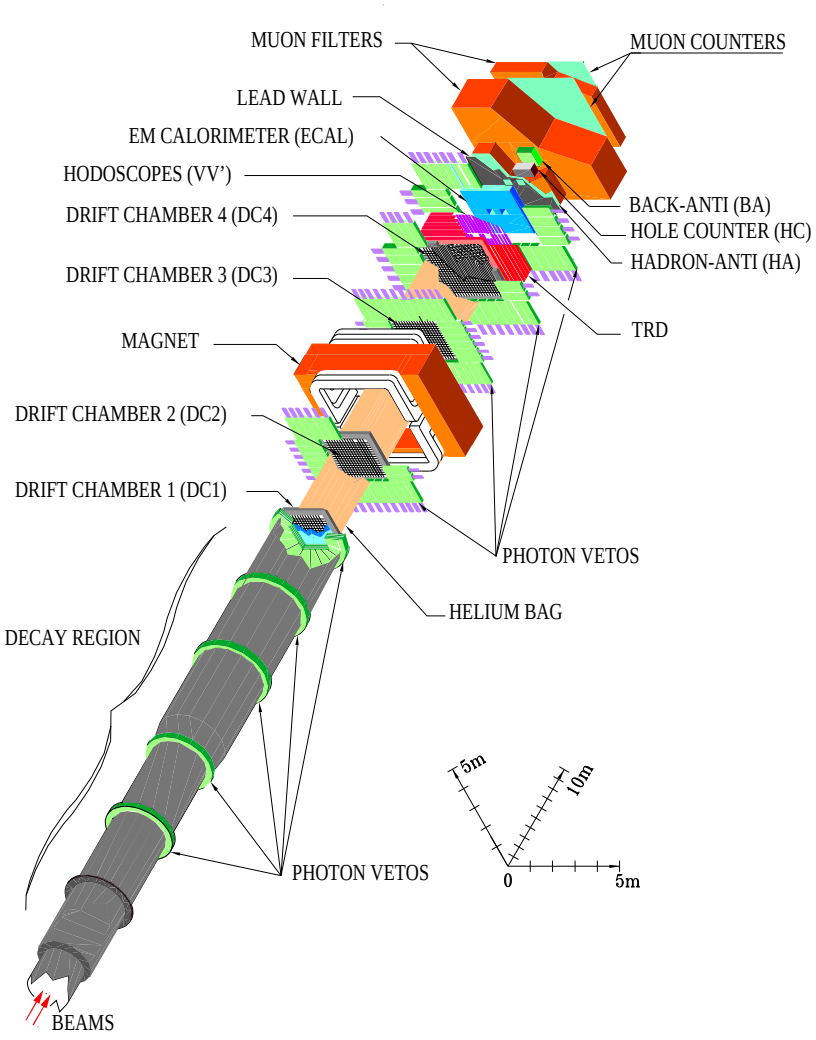

Figure 2.5: Three dimensional view of KTeV/E799 detector.

Table 2.1: Z-Positions and Transverse Dimensions of the main detector parts. The positions are given at front face of the detector with respect to the traget.

Detector Element	Position(m)	Transverse Size(m)
Vacuum Window	158.89	-
DC1(x plane)	159.42	1.30×1.30
DC2(x plane)	165.56	1.64×1.44
Analyzing Magnet	170.01	inner: 2.9×2.0
DC3(x plane)	174.59	1.74×1.64
DC4(x plane)	180.49	1.90×1.90
TRD1	181.17	2.18×2.18
TRD8	183.36	2.18×2.18
V bank	183.90	1.90×1.90
V' bank	183.95	1.90×1.90
CsI	186.01	1.90×1.90
HA	188.97	2.24×2.24
Mu2	194.83	3.93×2.99
Mu3X	196.59	3.93×2.99
Mu3Y	196.63	3.93×2.99

the effects of multiple scattering on the measurement of particle trajectories and momenta.

2.3.1 Analyzing Magnet

The manget [24] was centered around at Z=170 m, and the size of the magnet was about 2.9×2.0m. It was an electromagnetic dipole that produced a vertical field of $\sim$2000 gauss. The field strength can be mapped using a Hall effect probe stepped around inside the magnet. That was done before KTeV starting running to obtain the field strength with to about $\pm 1\%$ accuracy before other means could be used. The field diretion was flipped between up and down daily. A relativistic, charged particle crossing this field received a transverse momentum "kick" in the $\pm$X direction. By measuring the change in the angle of the trajectory of the particle in the X-Z plane, the momentum of the particle can be easily calculated.

2.3.2 Drift Chambers

Drift chambers are basically volumes of gas across which anode and cathode wires apply an electric potential. Charged particles pass through the gas, ionizing gas atoms and freeing electrons. While the ions drifted towards the field wires, the free electrons were accelerated by the electric field towards the nearest anode wire. Gaining energy, the electrons ionize yet more gas atoms, freeing more electrons and forming an avalanche in the high field region near the sense wire. When the electron avalanche reaches an anode wire, it creates a detectable signal voltage. From the position of the anode wires and the time that the signal arrives, the position where the particle passed through the drift chamber can be reconstructed.

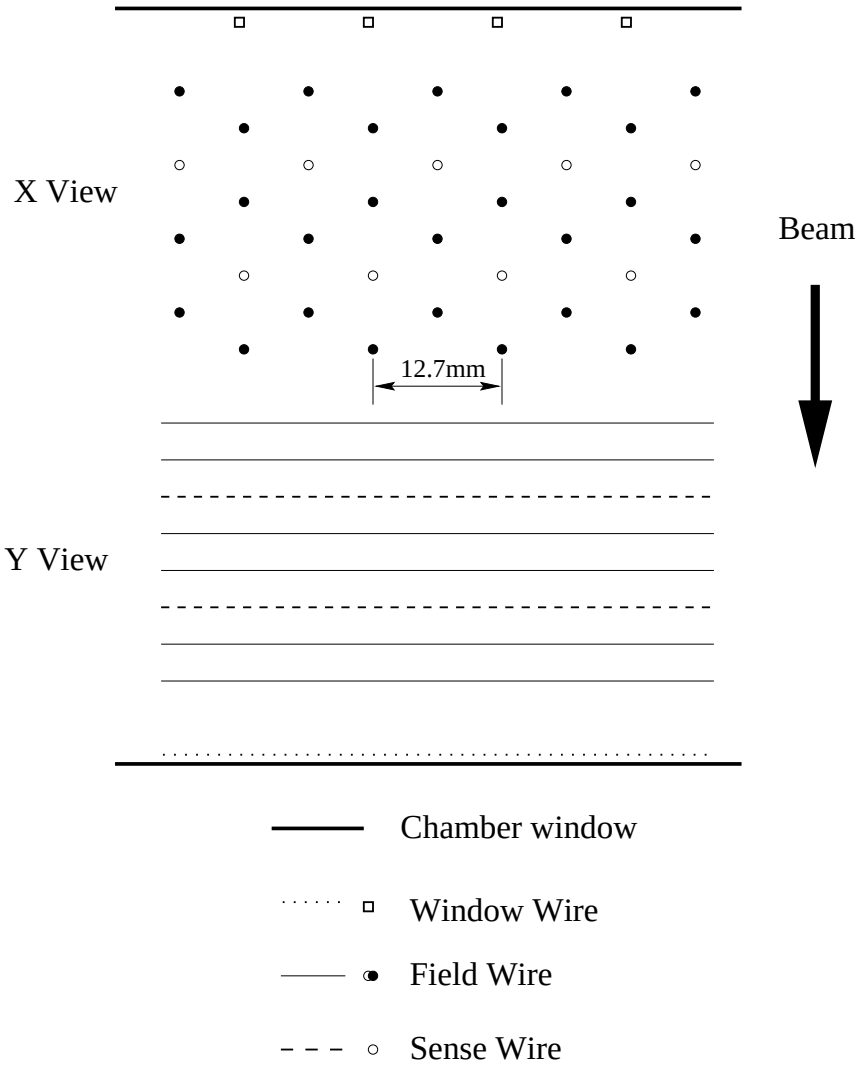

Figure 2.6: Schematic Drawing of Drift Chamber, viewed from the above, along the vertical x-sensing wires.

Each chamber contained four planes of sense wires, two each in the x and y views referred to as X, X', Y, and Y' planes. The sense wires were 25 μm gold-plated tungsten, while the field shaping wires were made of 100 μm gold-plated aluminum. The field wires formed a hexagonal "cell" around each sense wire as shown in Fig. 2.6.

The wires in a sense plane were separated by 12.7 mm. The two sense planes in each view, offset by 6.35 mm or a half cell size were staggered to resolve the two-fold ambiguity that results from ionization drifting towards the nearest wire.

The four chambers were of different sizes (Table 2.2), with the largest downstream, to increase acceptance for high angle tracks.

The gas of the chambers was a mixture of 49.75% Argon, 49.75% Ethane, and 0.5% to 1.0% isopropyl alcohol by volume. The purpose of isopropyl alcohol was additional quenching. The typical voltage applied to the chamber was: -2450 to -2550V for the field wires relative to the sense wires. The electron drift velocity was of the order of 50 μm/nsec and was roughly constant over much of the active chamber volume.

The signals from the four drift chambers were then amplified and discriminated by electronics located on cards mounted on the chamber frames [25]. The discriminated signals with 40 nsec width were fanned out to the trigger system and a set of LeCroy 3377 time to digital converters (TDC's) with a resolution of 0.5 nsec.

By converting the drift time measured at the TDC's to a drift distance, a position measurement could be made from each chamber wire hit with an accuracy of about 100 μm. Good tracks should construct to a Sum-Of-Distance (SOD) =

6.35 mm for the first electron, where SOD = the sum of the x and x' measured distance to a sense wire.

Table 2.2: Drift chamber sizes, measured in wires per sense plane.

DC number	View	Number of sense wires per plane	Cables
1	X	101	7
1	Y	101	7
2	X	128	8
2	Y	112	7
3	X	136	9
3	Y	128	8
4	X	140	9
4	Y	140	9

The momentum resolution of the drift chambers basically had two parts. In the Equation 2.3, the first part was caused by finite resolution of the hit position which is about $100\mu m$, and the other was caused by multiple-scattering. In our experiment, it was:

$$\frac{\sigma_p}{p} = 0.016\% \times p \oplus 0.38\% \tag{2.3}$$

where p is the momentum of a charged particle in GeV/c.

2.4 The Transition Radiation Detectors

When a particle passes between two regions of very different dielectic constant material (for example, a dielectic from the vacuum or from air), transit currents and fields arise. This can lead to emission of radiation known as transition radiation, i.e., An x-ray comes out. The energy loss is a very small part of the total energy loss of charged particles.

The attractive feature of TRD is that the radiated energy by TR photons increases with γ of the particles, not with their velocity. Since most processes used to identify particles depend on the velocity, γ dependence is different and is valuable for the highest high energy particles. Other properties of the Transition Radiation photons is that they are emitted in x-ray range, and the photon is strongly forward with $\theta \simeq 1/\gamma_{particle}$. Generally the useful threshold for TR is about $\gamma \simeq 1000$, i.e. if $\gamma < 1000$, almost no TR photons are emitted. This feature makes it possible to do the π^-/e^- discrimination, since the π^- mass is more than 200 times larger than electron mass, at the same energy there will be very different γ's.

In the KTeV experiment the TRD components were used to enhance the π^-/e^- discrimination by adding a 276:1 rejection factor for 90% electron acceptance typically.

The size of all the eight TRDs was $2.1m \times 2.1m$. They were placed between drift chambers and the trigger hodoscopes. The TRDs account for roughly 11.5% of radiation length (X_0) in the acceptance region (8 TRDs). Figure 2.7 shows the schematic layout of the TRD design. Further details about the TRDs are available

in [26, 27]

Each TRD, Fig. 2.7, consisted of radiator, an active MWPC volume, and two buffered gas volumes. The radiation material in KTeV was a mat of ploypropylene fiber (density of 0.5 g/cm^3). A low-Z material, polypropylene, was used to minimize absorption of x rays in the radiator. There were two beam holes in the radiator with a size of 15.5 cm $\times$ 15.5 cm each to reduce beam interactions.

The gas volumes and radiators were segmented by aluminized mylar, called entrance window. MWPC consisted of vertically mounted cathodes and anodes. The cathode was a wire plane consisting of 85 μm diameter Be-Cu wires with 2.5 mm spacing. The entrance window was kept at a slightly higher voltage than the cathode forming a 1.5 mm mini-drift gap. The anode to cathode gap was 6.5 mm, and the anode was a wire plane consisting of 25 μm diameter gold plated tungsten wires with a 5 mm spacing. The planes were lined up so that each anode wire sat directly behind a cathode wire.

The anode wires were ganged into channels consisting of two wires each in the central 60 cm covering the two beam holes with an effective pitch of 1 cm. In the outer region, 4 wires were summed into a channel with an effective pitch of 2 cm. This gave a total of 112 channels/plane, or 224 channels/chamber. Therefore, there were 1792 channels for the 8 chambers.

Following the radiator was the MWPC. The MWPC must be very efficient for absorbing the x-ray photons, so it is normally filled with a high-Z gas. In the KTeV experiment the gaseous detector needed at least 24 mm of Xenon gas. The ionization energy loss could fake a TR signal and reduce the π/e separation ability.

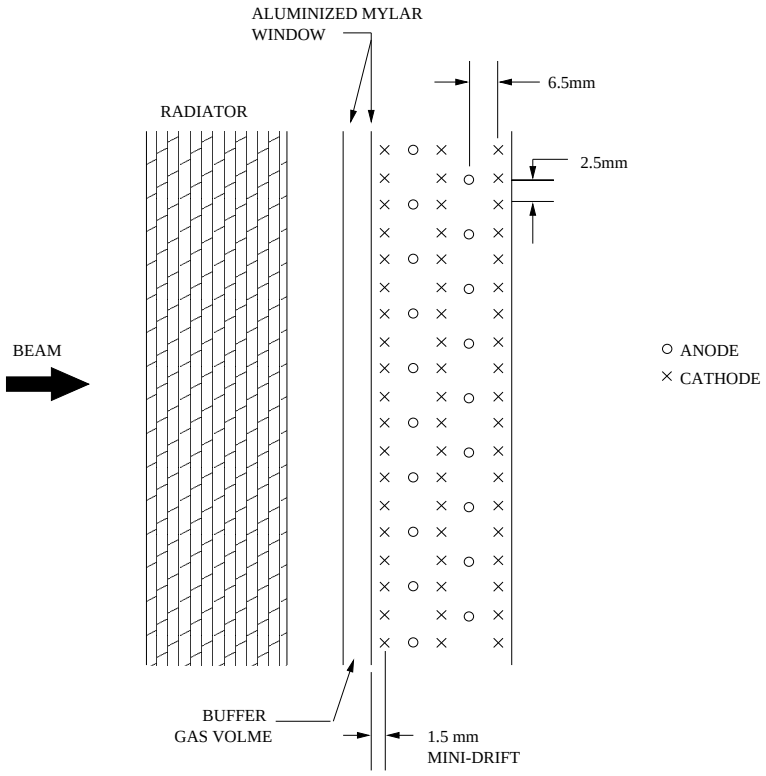

Figure 2.7: The schematic layout of the TRD detector.

To achieve a high yield of TR and to minimize the ionizing energy deposit, a gas mixture of 80% Xe and 20% CO_2 was chosen.

The gas purity was very important to the accuracy of the TRD, for example, a 0.1% change in concentration of main components could result in a 1% change in gain. The composition of active volume gas was monitored by a gas chromatography system at 100 ppm levels. With the operating high voltage of -2400V, the gas mixture gave a drift velocity of 5 cm/μsec.

The voltage was automatically regulated by monitoring the gas pressure so that each chamber maintained the same gain. This was necessary for two reasons. First, since a TRD is a detector that measures the pulse height to look for X-rays above a miminum ionization signal, any variation in gain would have caused changes in the π/e rejection and the performance for particle identification would vary with temperature and pressure variations. Secondly, the TRD system also used the pulse height information on-line to generate a level 2 trigger. Variation of the gain would cause changes in triggr condition which would be unacceptable for physics analysis.

The buffer volume was filled with a safe gas of C_2F_6 that was X-ray transparent and had the same order of density as Xenon so that it helped to support the entrance window. This kept the inner aluminized window flat to within 100 μm.

The pulse from each channel was preamplified and sent out. The amplifier produced an output voltage directly proportional to the input charge. The preamp had a high gain of $\sim$ 40. The output of the preamp was differential to improve noise rejection, and was passed into a postamp by a cable whose length was a part

of the time delay requirement of the trigger system. The postamp first translated the differential input into a single-ended signal. Next, the pulse was shaped so that the length of the pulse tail was reduced. That would keep the ADC gate width as narrow as possible to minimize accidentals. The shaped pulse was finally sent to a low gain amplifier stage. This additional stage of amplification allowed the signal channel to be tuned for optimizing its gain.

2.5 The Trigger Hodoscopes

In order to provide fast signals (in 15 nsec) for use with trigger logic that the drift chambers could provide, two planes of scintillator hodoscopes were installed in front of the CsI calorimeter. These could be used to count the number of charged particles [20, 28] in trigger level 1.

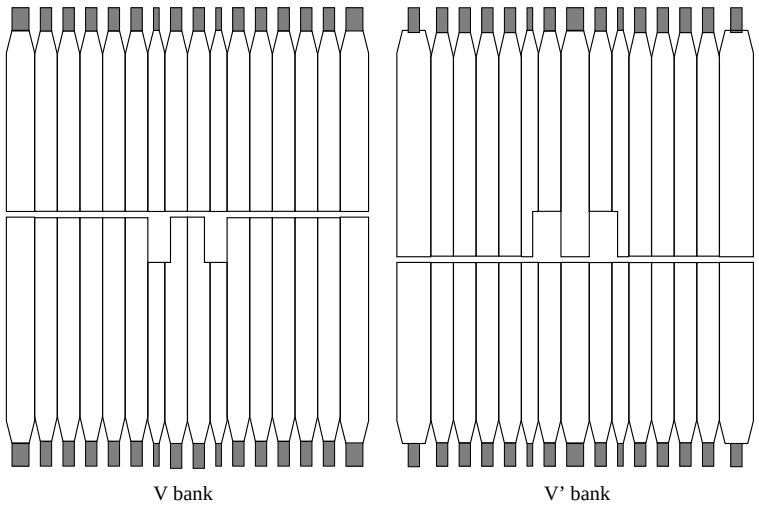

Figure 2.8: Schematic drawing of V and V' bank front view.

Figure 2.8 shows the geometry of the hodoscopes. The upstream hodoscope was called the V bank, and the other one was called the V' bank. Both the V and V' bank consisted of 1 cm thick scintillators viewed by PMTs which were mounted through light guides. There were no overlaps between the counters in each bank in order to avoid a double counting by a single particle, but the V and V' planes were offset by one-half counter to prevent the particles slipping through the possible cracks between them. The size of the two hodoscope planes was 1.9 m $\times$ 1.9 m. Two beam holes were cut in the counters. There were five different counter widths used: 9.92 cm, 11.82 cm, 13.74 cm, 15.63 cm and 17.76 cm.

2.6 The Photon Veto System

The Photon Veto system was used to veto the events where a decay product (such as photon or charged particle) left the fiducial volume of the detector. Basically, in E799, there were at least 4 types of photon veto components. They were Ring Counters (RC6-RC10), Spectrometer Antis (SA2-SA4), CsI Anti (CIA), and Collar Anti (CA). Each photon veto counter had a sandwich structure of Pb radiators and scintillators [29]. The light yield in the scintillator was detected by PMT's.

2.6.1 Ring Counters

The Five "Ring Counters" (RC6-RC10), Fig. 2.9. were located inside the vacuum decay volume. The locations of the RC's are listed in Table 2.3. These counters are circular on the outside and were placed flush with the vacuum vessel walls. The inner aperture is square. The RC's were made of 24 alternating layers of

2.5 mm lead and scintillator. For the first 16 layers, the lead sheets were 0.5 radiation length each, for the other 8 layers, the lead was 1 X_0 thick each. The total radiator was equivalent to 16 radiation lengths.

Table 2.3: Positions and Dimensions of the RC's. The positions were with respect to the traget.

Veto Element	Position(m)	Transverse Size(m)
RC6	132.60	inner: 0.84×0.84, outer radius: 1.00
RC7	138.60	inner: 0.84×0.84, outer radius: 1.00
RC8	146.60	inner: 1.18×1.18, outer radius: 1.44
RC9	152.60	inner: 1.18×1.18, outer radius: 1.44
RC10	158.60	inner: 1.18×1.18, outer radius: 1.44

2.6.2 Spectrometer Anti's

Three Spectrometer Anti's (SA's), Fig. 2.10,Table 2.4, define the apertures around drift chambers 2, 3, 4, and were located just upstream of these chambers. Just as Ringer Counters, the SA's also had 16 radiation lengths of Pb. There were 32 layers of 0.5 radiation length Pb and scintillator. They are capable of detecting stray photons down to energies of 100 MeV. Light was gathered and sent out by glass fibers to PMT's.

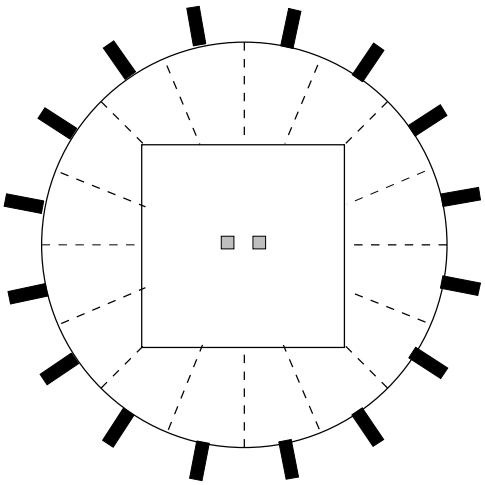

Figure 2.9: A typical RC viewed from upstream, located inside the vacuum region. The RC's dimensions are shown in Table 2.3.

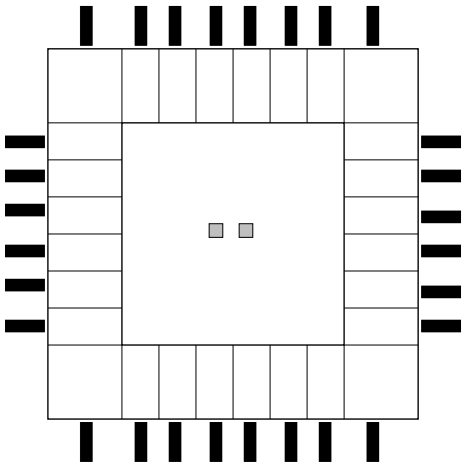

Figure 2.10: SA4 viewed from upstream. SA's and CIA had different dimensions as shown in Table 2.3.

Table 2.4: Positions and Dimensions of the Spectrometer Antis. The positions are given at front face of the detector with respect to the traget.

Veto Element	Position(m)	Transverse Size(m)
SA2	165.12	inner: 1.540×1.366, outer: 2.500×2.500
SA3	173.99	inner: 1.692×1.600, outer: 3.000×2.400
SA4	180.02	inner: 1.754×1.754, outer: 2.372×2.372

2.6.3 Cesium Iodide Anti and Collar Anti

The Cesium Iodide Anti (CIA) and Collar Anti (CA) are the two veto counters around the outer and inner edges of the calorimeter respectively. The CIA used the very similar configuration like SA's, and had 16 radiation lengths with 32 layers of 2.5mm Pb and scintillator sandwich structure. It also provided signals to Level 1 Trigger to veto events.

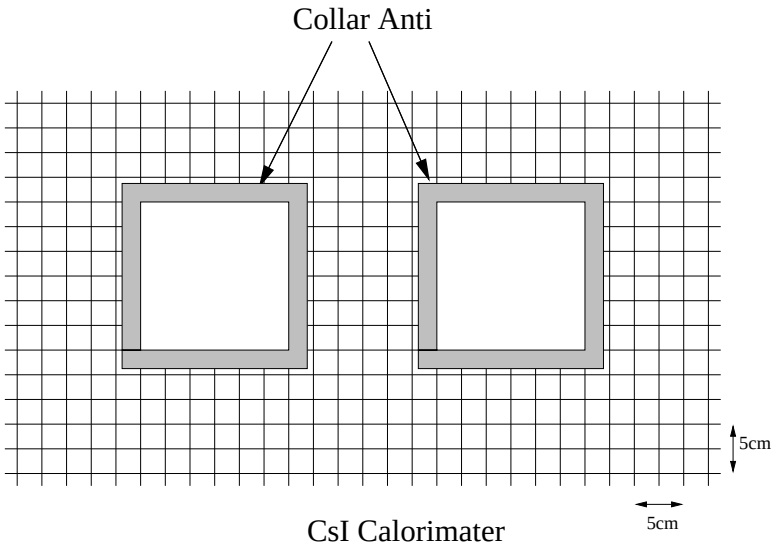

Figure 2.11: The Collar Anti located just upstream of the CsI calorimeter.

The "Collar Anti" (CA) was located in front of the calorimeter and just around the beam holes like a picture frame (Fig. 2.11,Table 2.5) to catch the events that wouldn't deposit energy in the CsI completely. Events with such photons were rejected. The CA included two identical square annular detectors and overlaps the crystals immediately adjacent to the beam hole by 1.5 cm. It consisted of 3 layers of 1 cm thick scintillator each followed by a layer of $2.9X_0$ tungsten.

Table 2.5: Positions and Dimensions of CA and CIA. The positions are given at front face of the detector with respect to the traget.

Veto Element	Position(m)	Transverse Size(m)
CIA	185.19	inner: 1.842×1.842, outer: 2.200×2.200
CA	185.91	inner: 0.150×0.150, outer: 0.180×0.180

2.7 The Electromagnetic Calorimeter

2.7.1 The Purpose of CsI

The primary purpose of electromagnetic calorimeter was to measure the energy and position of photons. The second purpose was particle identification, namely e^-/π^- separation. In addition, measuring the charged particle position at the calorimeter enabled us to resolve the x-y ambiguity in the track reconstruction.

2.7.2 The CsI Crystals

Instead of Lead-glass, CsI crystals were found to be a better substitute material with excellent energy and position resolution, quick signals and good radiation hardness (Cesium-Iodide is much more resistant to radiation damage as compared to the lead glass used in previous experiments [30]).

The front face of the KTeV electromagnetic calorimeter was located two meters downstream of the trigger hodoscopes, at z =186 m.

The calorimeter, Fig. 2.12, was composed of 3100 pure CsI crystals with a length of 50 cm ($\simeq 27X_0$). There were two sizes of crystals. For the inner part of

$1.2m \times 1.2m$ area, 2232 of $2.5cm \times 2.5cm$ crystals were placed with two beam holes whose sizes were $15cm \times 15cm$ each. For the outside of the $1.2m \times 1.2m$ area, 868 $5cm \times 5cm$ crystals were stacked. About 80% of all crystals were composed of two halves (25 cm long each) glued with Epo-Tek 305 epoxy, which was chosen for its high UV transmission. The remaining 20% were 50 cm long single crystal without connection.

The CsI light yield depends on the temperature with -1.5% per degree Celsius. In order to reduce the gain fluctuations due to the temperature variation, the array was placed in a light-tight blockhouse where the temperature was controlled to ± 0.1C. Besides, the blockhouse environment was kept dry with a humidity of 4% or lower to protect the crystals which were slightly hygroscopic.

Each crystal was wrapped in $13\mu m$ thick mylar film, part of which is aluminized. By choosing where we put the reflective mylar, the light collection was tunned to be uniform to within $\pm 5\%$.

The CsI crystal yielded typically 20 photoelectrons per MeV. The scintillation spectrum can be approximately characterized by a 'fast' and a 'slow' component. The fast spectrum peaked at 315 nm with a time constant of 20 ns. The slow one peaked at 420 nm and had a time constant of 1 us. From 80 to 90% of the scintillation light was emitted with in 100 ns. The energy deposited by particles that interact electromagnetically, such as photons and electrons, is almost entirely contained within the calorimeter because the CsI is $\simeq 27X_0$ long. However, showers due to hadronic backgrounds such as protons and pions are not fully contained by the calorimeter because it is only 1.4 hadronic interaction lengths long. By

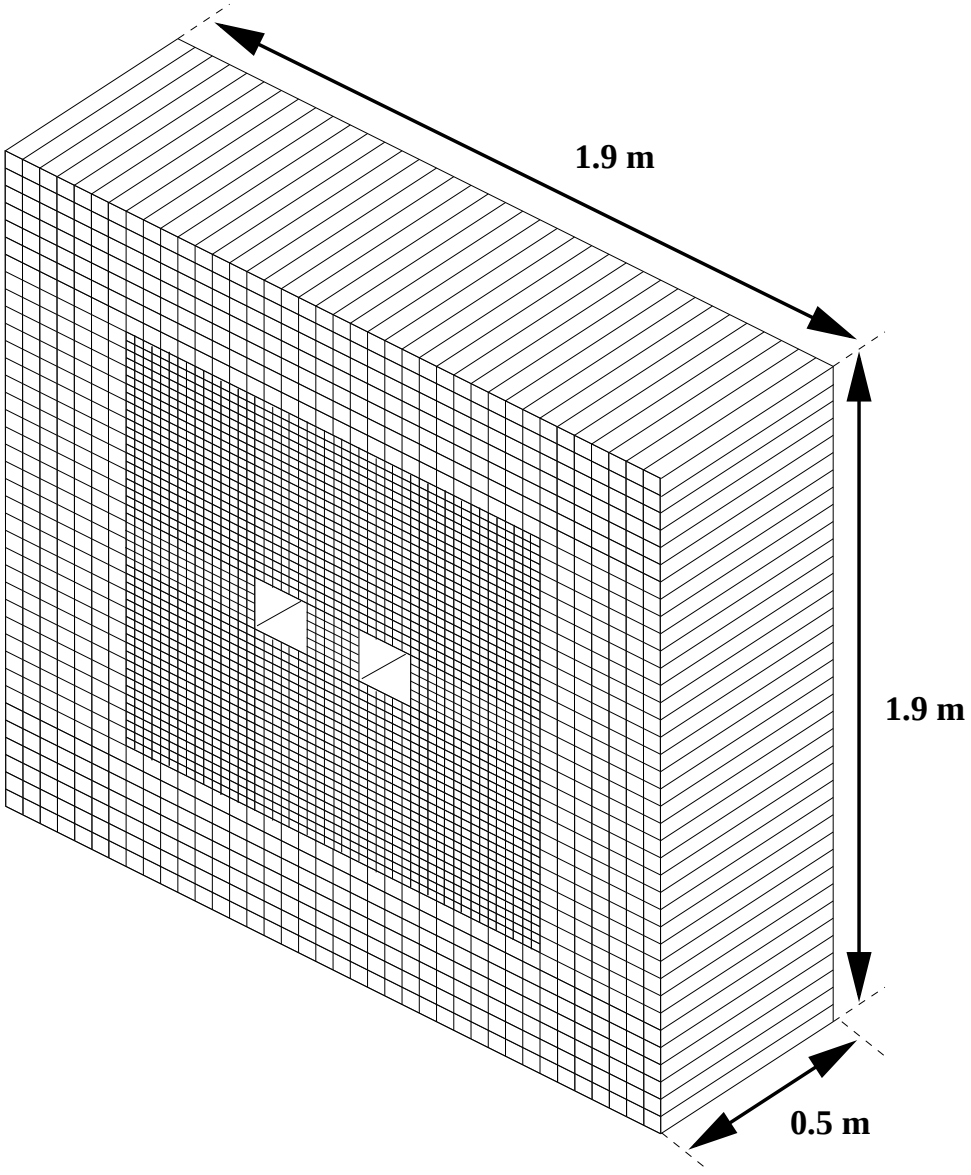

Figure 2.12: Beam view of the KTeV CsI calorimeter array.

looking at the ratio E/p, with E the energy measured in the calorimeter and p the momentum as determined by the spectrometer, electrons may be effectively distinguished from charged pions.

2.7.3 The PMT and DPMT

The scintillation light produced by electromagnetic showers in the CsI crystal was detected by the PMT mounted on the back of each crystal. The large crystal was viewed by 1.5 inch Hamamatsu R5330 PMT with six stage dynodes, and the small crystal was viewed by 3/4 inch Hamamatsu R5364 with five stage dynodes. Both type of the PMTs had a gain of 5000 with a typical high voltage of $-1200V$. The signals from each crystal were then digitized by a Digital PMT base, or DPMT.

The DPMT Fig. 2.13 was an auto-ranging device. The input current, I, was split into eight binary ranges, i.e. into I/2, I/4, I/8, I/16, I/32, I/64, I/128, and I/256. Then each of the eight split currents was integrated. Next, it was determined which of the eight binary ranges were *inrange*, and the integrated current from this range was digitized with an 8-bit FADC. Thus the DPMT produced an 8 bit mantissa and a 4 bit exponent, for 16 bits of dynamic range. The DPMT's had a very low noise level (less than 1MeV), and they had a wide dynamic range. The DPMTs were calibrated using a laser flasher system. After calibration, additional nonlinearity due to the DPMT was well under 1%. Detailed information about DPMT can be found [31, 32].

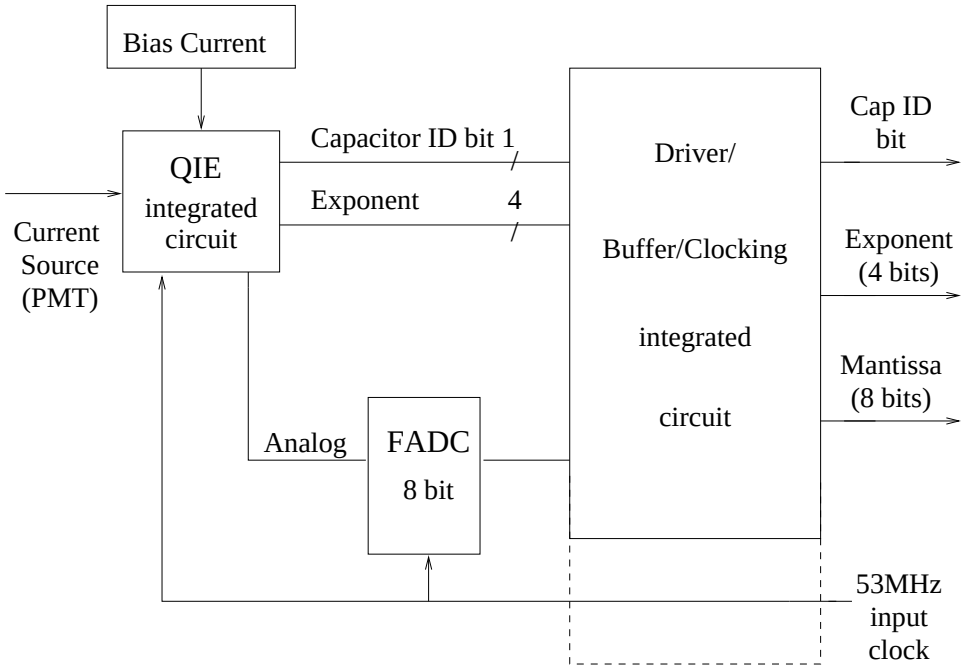

Figure 2.13: Block diagram of DPMT.

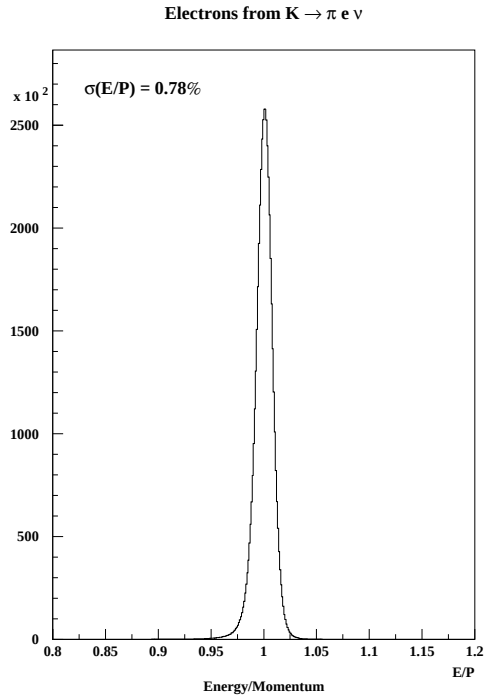

Figure 2.14: E/p for electron in K°_{e3}'s, where E is the energy measured at the calorimeter, and p is the momentum measured by the spectrometer.

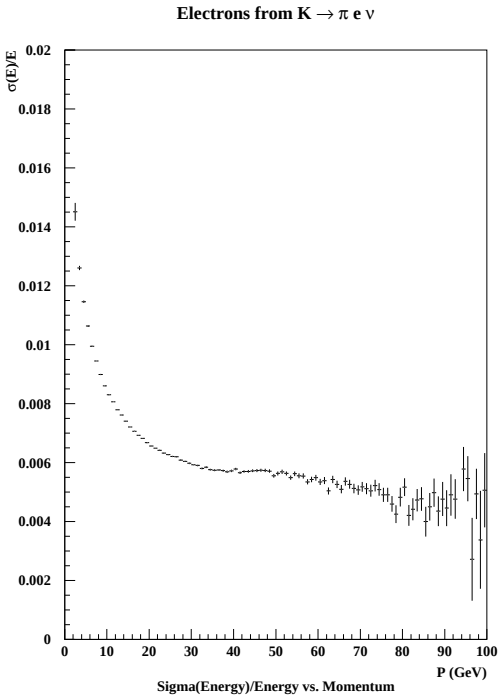

Figure 2.15: The calorimeter's intrinsic energy resolution measured in K°_{e3} events as a function of electron momentum.

2.7.4 The resolution of CsI

The CsI calorimeter was also used as a particle identification detector for e^-/π^- separation. Figure 2.14 shows E/p for electrons in K°_{e3} events, where E is the energy measured by the CsI calorimeter and p represents the electron momentum measured by the spectrometer.

As discussed before, the CsI crystals were 27 radiation lengths long. Electrons deposited almost all of their energy in the calorimeter and had a peak of unity in

the E/p distribution.

The intrinsic resolution of the calorimeter is shown in Fig. 2.15 as a function of electron momentum. The energy dependence had a form of

$$\frac{\sigma_E}{E} = 0.6\% \oplus \frac{0.6\%}{\sqrt{E}} \,. \tag{2.4}$$

Here, the $1/\sqrt{E}$ dependence resulted from photon-statistics in scintillation light. The constant term of 0.6% accommodated other effects such as non-uniformity in light collection efficiency, internal calibration error, fluctuation of light yield due to temperature variation, uncorrected light leakage, electronic noise [33].

From Fig. 2.15, one can see that the typical E resolution was better than 1% for energy above 4 GeV. e/π rejection was about 500:1.

The position resolution was measured to be approximately 1 mm in the small crystals, and about 1.8 mm in the large crystals.

2.8 The Hole Counters

For a hyperon decay, one of its properties was that there was a high momentum proton or anti-proton in the beamline. In the KTeV experiment there was a small fast scintillation counter, known as a "Hole Counter [34, 35]", placed in each beamline behind the CsI calorimeter in the hole of the Hadron Anti steel filter.

The HC's size was 6.296×6.296 in^2 (16×16 cm^2), and 0.0625 inch thick. The scintillator material was Bicron 404 plastic organic scintillator. Lucite light pipes of 0.0625 in thickness were bent at a right angle and then twisted by heat treatment to map on the 0.75 inch diameter photo cathode of a Hammamatsu R3082 photo tube.

The efficiency [38] of the hole counter paddles in the Monte Carlo was assumed to be 0.96 across the entire surface of the paddle. Using two track events in the accidental trigger, the hole counter efficiency was measured as 0.950± 0.005 for the right hole counter, and 0.952 ± 0.005 for the left hole counter.

2.9 The Hadron Anti

A 15 cm thick Pb wall was located just downstream of the calorimeter. After the Pb wall, there was a bank of scintillator hodoscopes, called "Hadron Anti" (HA)[36] at z=188.5 m. The purpose of the Pb wall was to absorb all the leakage in the the electromagnetic events from CsI, and also induce a hadronic shower when the hadron, such as $\pi^{\pm}$ passed through it. The purpose of HA was to veto the events producing charged pions or muons. In particular, for the hyperon trigger, HA reduced the trigger rate by a factor of about 3.5 by vetoing on the higher energy pions from the decay of lambda, $\Lambda^{\circ} \rightarrow p\pi^{-}$. Figure 2.16 shows HA's configuration and dimensions.

The HA was placed upstream of the BA as far as possible to minimize the rate due to backsplash radiation from the BA and the neutral beam dump. Both the lead wall and the HA had a single large (34 cm × 64 cm) beam hole to let the beam go through. Also, there was a 1 m thick steel wall with a proportionally large hole placed downstream of the HA to shield it from the BA backsplash. The photons going into beam holes were detected by the BA. This 10cm Pb wall was used to produce hadron showers and to absorb leakage of electromagnetic showers from the calorimeter. The thickness of that was chosen to be 15 cm (0.9 interaction

lengths).

The light yield produced by the HA scintillation counter was detected by PMTs. The first level trigger used an analog sum from all the HA counters as an input.

In this way, events with a $\pi^{\pm}$ could be vetoed by the Hadron Anti. In particular, for the hyperon trigger, HA reduced the trigger rate by vetonig on the pions from decay of lambda, $\Lambda^{\circ} \rightarrow p\pi^{-}$.

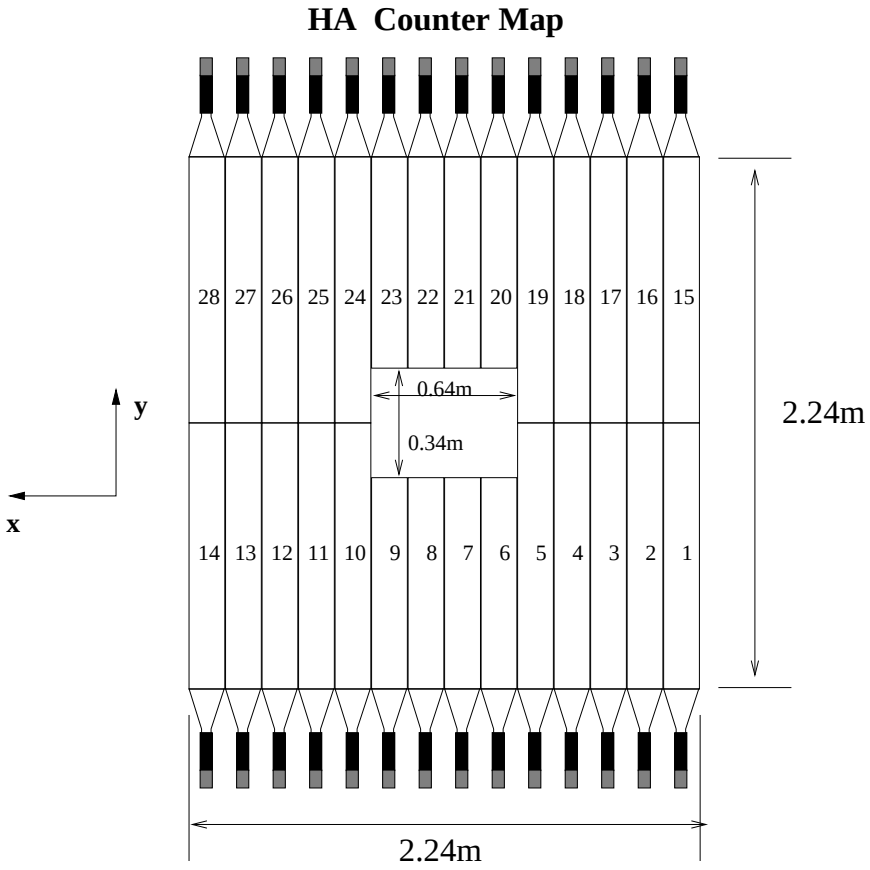

Figure 2.16: The HA hodoscope composed of 28 scintillation counters.

2.10 The Muon System

One purpose of Muon System, Figure 2.17, was to reduce the trigger rate by rejecting events that decay to muons, which was not the desired decay mode in some cases. Also, it served some other purposes, for example, M2 Filter (3 m steel) also served as the neutral beam dump.

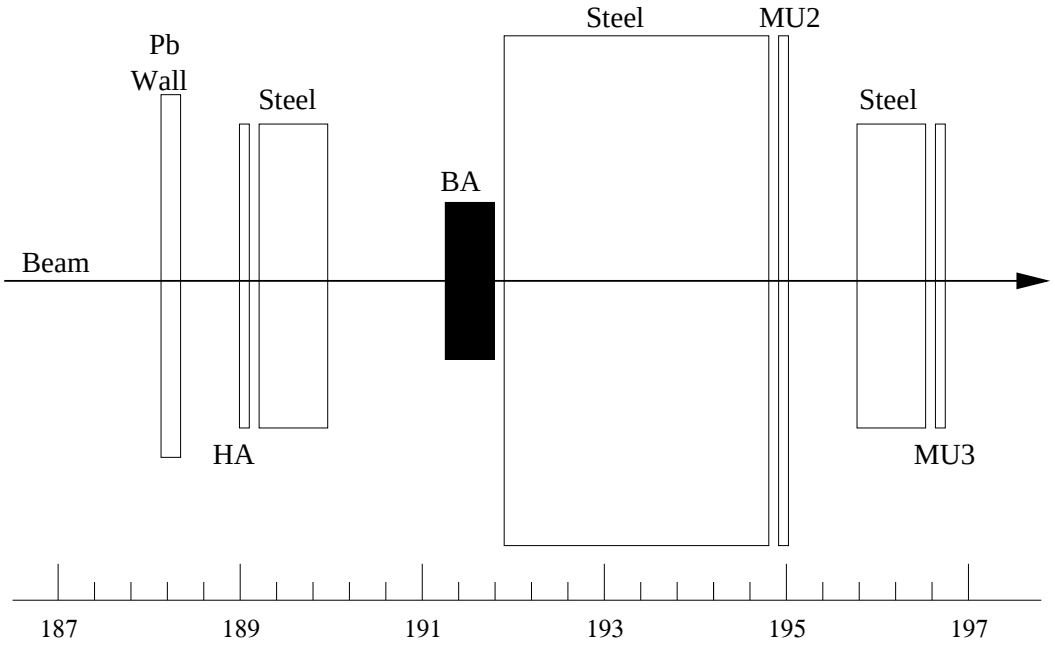

Figure 2.17: The Schematic Drawing of Muon System.

The Muon system [37] contained the most downstream detector components in KTeV. There are three Muon counters (MU2, MU3Y and MU3X). (MU1 was discussed in Hadron Anti Section, which included a 15 cm Pb Wall and a 1 m Steel.)

In front of MU2 hodoscope, there was a 3m deep, 3.4 m high and 4.3 m wide,

44 cubic meters of steel. It served as the neutral deam dump, and it stopped most of the hardronic shower activity. The MU2 hodoscope was a 3.93m $\times$ 2.99 m plane of 56 overlapping counters located immediately behind the steel. Mostly Muons were expected to survive such a large amount of material. MU2 was designed to reduce the trigger rate by rejecting events decaying to muons. It had to have a very large transverse dimension to be able to catch the muons which were further scattered in the steel.

There was another 1m steel in front of MU3. The steel was designed to stop as much non-muon activity as possible that leaked through. MU3Y and MU3X consisted of horizontal and vertical counters respectively. They were used at trigger level.

Chapter 3

The Trigger System and the Run

In this chapter, we discuss the KTeV E799 three-level trigger system [39, 40, 41, 42, 43] first, and then we will pay much attention to the important hyperon triggers, i.e. trigger10, trigger11 and trigger12.

There were two types of three-level triggers. The "CALIBRATION Triggers" designed to collect data for cosmic muons, pedestal measurements and the CsI laser calibration.

The "BEAM Triggers" designed for the physics trigger. Each of the 16 beam triggers was optimized to collect one or more specific rare decays.

Event selection included an online trigger and offline data reduction. The trigger system includes two hardware stages, Level 1 and Level 2, and software trigger Level 3. Offline data reduction consists of a data split to separate data according to general physics topics and a data crunch to identify roughly and remove uninteresting events.

Basically different runs in KTeV had their own specific decay modes to study. Most decays proceeded to final states that were not useful for calibration or interesting to study. The purpose of the trigger system was to decide which were the most interesting events for the data acquisition system to read out of the detector

and record onto the tape.

3.1 Level 1 Trigger

Level 1 trigger [44] uses the fastest Boolean sources in simple logical combinations to make decisions. The sources of these signals can be from scintillator counters, calorimeter total energy sum and the logical OR of the drift chamber signals. The Level 1 trigger rate was from $\sim$ 80 kHz to $\sim$ 20 kHz. Hence, it was very fast and available for each 19 nsec bucket (no dead time) in the spill structure.

The 16 beam triggers used different combinations of 80 Level 1 logic sources. These trigger sources were sent to a series of LeCroy 4508 Programmable Lookup Units (PLU) and LeCroy 4516 Programmable Logic (PL), which were programmed and could be changed via CAMAC.At the same time, the RF signal provided by the accelerator was passed into the PLU and PL to strobe the trigger sources. We call the time strobed RF bucket as "in-time" bucket. A combination of PLU and PL generated an output signal by looking at the firing pattern of the Level 1 trigger sources.

Finally, decays with high rate were prescaled before reaching the second level, which means 1 out of the prescale factor would be selected.

3.2 Level 2 Trigger

When the event satisfied the Level 1 requirements, the output signal from Level 1 trigger started a digitization of ADCs and provided a stop signal for TDCs. The trigger system went to the next stage, called Level 2 trigger [45]. The Level 2

trigger consisted of information which took a longer time to obtain, either because the detector element had a slow response like the drift chamber, or because the pattern recognition took some time like HCC, or the TRD information.

These input signals from Level 2 sources were sent to another series of PLUs(LeCroy 2373) with a Level 1 signal. Again, PLUs did a pattern recognition of trigger sources, and determined whether to go to the next stage of the triggering. When the event satisfied the Level 2 requirements, each PLU generated the outputs, which were used to form a 16 bit trigger mask; the bitwise-AND of all the lookup units was the final 16 bit trigger mask. This means that we could have 16 Beam triggers in maximum. If an event failed at this stage, that event would be aborted before finishing ADC digitization, and would go to the next event.

If the event rate was too high after the Level 1 trigger, some types of triggers were prescaled by an additional module with an integer prescaling factor before the Level 2 trigger.

Since the Level 2 decision took 3.3 μsec on average and the Level 1 trigger rate was $\sim$ 80KHz, Level 2 dead time was 3.3 μsec $\times$ 80 KHz $\simeq$ 26%.

3.2.1 The Stiff Track Trigger

We have to mention the Stiff Track Trigger [46, 47] for hyperon decays. We know that for hyperon decays, there was a high momentum proton (or anti-proton) in the beamline all the time. The "Stiff Track Trigger" was used to exactly trigger this kind of property. The STT was used to select events with a high momentum track ($\geq 50 GeV/c$) going down the left or the right beam hole and to determine

the track's change in slope before and after the analysis magnet from the pattern of latched drift chamber hits in the center of the beam hole regions in the horizontal view.

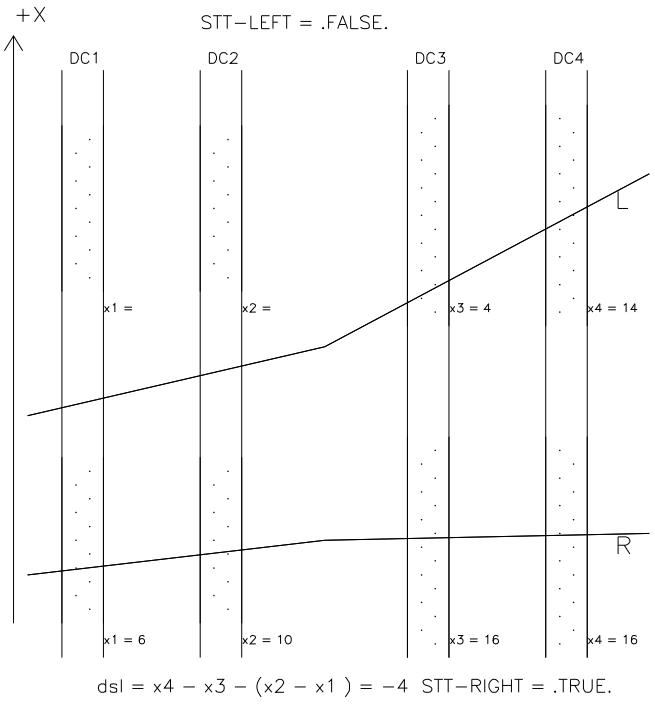

Figure 3.1: STT Trigger. The dot areas denote the beam hole. In the right beam hole, the STT result (-4) for the right side is TRUE. On the left side, the STT result (10) for the left side is FALSE. Thus the event is accepted.

If there was either 1 or 2 adjacent wires hit in the instrumented area for each chamber, the STT computed the corresponding horizontal position, "x_{DCn}", in

each drift chamber and then calculate the quantity "$x_{DC4} - x_{DC3} - (x_{DC2} - x_{DC1})$". This quantity is proportional to the change in slope of the track. If its value was between -7 and +7 inclusive, the event was selected by the STT, otherwise the event was rejected. Any other combination of inputs caused the STT to reject the event. Accidental in-time activity in the instrumented area would as well cause the STT to reject the event. It was also possible for a track to travel down the beam hole and miss the area instrumented by the STT.

3.3 Level 3 Trigger

The events that satisfied the Level 2 requirements were sent to the final stage of triggering(Level 3 trigger), where they were reconstructed in the UNIX machine with software. Therefore, all the readout including digitization was completed before the Level 3.

Each input event to Level 3 contained the Level 2 mask. The Level 3 made a final decision of writing it out to magnetic tapes (DLTs), based on the selection criteria imposed on the tagged trigger. The software in Level 3 shared most codes with offline use; however, it was tuned to minimize the processing time. A total of 24 Challenge SGI CPUs(200MHz$\simeq$160mips each) was used to process and filter the events.

The resulting time to process was 3 ms per event.

3.4 Hyperon Trigger

Most of the 16 triggers used for E799 running were dedicated to kaon decays, only three triggers were dedicated to collecting hyperon data.

They were Tirgger 10, 11 and 12. The "Hyperon Minimum Bias" trigger (bit 12) had a large prescale of 2000 and loose trigger conditions to study the efficiency of the other two hyperon triggers. The "Λ-trigger" (bit 11) was built to trigger on hyperon shape events and selected mainly $\Lambda^\circ \to p\pi^-$ events and $\Xi^\circ \to \Lambda^\circ\pi^\circ$ events where $\Lambda^\circ \to p\pi^-$. It had a prescale of 7 and was mostly used to study the principal decay of Ξ°'s as the normalization mode for most of the Ξ°rare decays. The main hyperon trigger (bit 10), called "Ξ°-beta-trigger" was a subset of the "Λ-trigger" to select hyperon beta decays.

The first and second trigger requirements for the hyperon triggers were:

- $\Xi^\circ \to e^-\bar{\nu}_e$ were collected in Trigger 10

$$1V * L1HOLETRK * ET_2 * \overline{HA\_DC} * \overline{PHV1} * \overline{CA} \qquad (Level\ 1)$$

$$*2HCY\_LOOSE * LAMBDA\_RA * HCC\_GE2 \qquad (Level\ 2)\,,$$

$$(Prescale\ 1/1)$$

- $\Xi^\circ \to \Lambda^\circ\pi^\circ$ with $\Lambda^\circ \to p\pi^-$ were collected in Trigger 11

$$1V * L1HOLETRK * ET_2 * \overline{PHV1} * \overline{CA} \qquad (Level\ 1)$$

$$*2HCY\_LOOSE * LAMBDA\_RA * HCC\_GE2 \qquad (Level\ 2)\,,$$

$$(Prescale\ 1/7)$$

- $\Lambda^{\circ} \rightarrow p\pi^{-}$ were collected in Trigger 12

$$1V * DC12\_HOLE * DC34\_HOLE * ET_1 * \overline{PHV1} \qquad (Level\ 1)$$

$$*HCYDUM * STTDUM * HCC\_GE1 \qquad (Level\ 2)\,,$$

$$(Prescale\ 1/2000)$$

Below is the explanation of these trigger elements:

$1V$: A hit in one of the two hodoscope planes.

$L1HOLETRK$: A track down the beam hole. A fast OR of the vertical wires in the beam region in the first and second drift chambers is performed and combined with the activity in the hole counters. A track is said to have gone down the beam hole if there is at least one of these hits in each of the two first chambers and enough activity in the hole counters. For the minimum bias trigger12, only activity in the hole counters is required. This beam hole requirement in addition to 1V means that at least two charge tracks are in the event.

$\overline{PHV1}$: The various photon vetoes – ring counters (RC), CsI calorimeter anti (CIA), spectrometer anti (SA) – are quiet, according to the standard minimum ionizing particle thresholds used. It means that no photon or charged particle has escaped the fiducial volume of the detector.

$LAMBDA\_RA$: There is a high probability to have a high momentum track down the beam hole. This is the Stiff Track Trigger explained in section 3.2.1. It is not used in the minimum bias trigger.

$ET_2(ET_1)$: There is at least a total of 18 GeV (11 GeV) of energy deposited in the electromagnetic calorimeter. The lower threshold of ET_1 was used for the beta

trigger in the winter as well, but it was raised to ET_2 since Cascade beta events deposit a total energy of typically greater that 20 GeV in the CsI.

$\overline{HA\_DC}$: There is no activity in the hadronic scintillator plane named the hadronic anti (no energy deposited above the higher threshold). This means that the event has no hadronic activity in the fiducial region excluding the beam region.

HCC_GE1: There are at least 1 online hardware clusters in the calorimeter. HCC_GE2: There are at least two online hardware clusters in the calorimeter.

$2HCY\_LOOSE$: There are two or more hits in each drift chamber horizontal wire planes, with a possible hit missing in one of the two upstream chambers.

$STTDUM$ Stiff Track Trigger Dummy requirement, wait for STT to finish processing.

HCY_DUM: Wait for all the Drift Chamber's 4 horizontal wire planes (Y-view) to finish the hit counting processing.

$DC12\_HOLE$: There is at least one hit in the DC_OR chamber 1 and 2's left and right holes.

$DC34\_HOLE$: There is at least one hit in the DC_OR chamber 3 and 4's left and right holes.

3.5 The Runs

The E799 experiment took data in two stages: the 1997 Run spanned the Jan. 1997 to Sept. 1997 time period, and the 1999-2000 Run extended from Sept. 1999 to Jan. 2000. This analysis uses the data collected in the 1999-2000 Run. The 1999-2000 period of data-taking spans the runs 14625 to 15548.

Each uninterrupted period of data collection in the larger E799-II Run is also called a run. A single run typically lasts for about eight hours. This is about the length of time it takes for output tapes to fill during normal running conditions and beam intensity.

During the data taking phase, data that pass any level 3 trigger were written to digital linear tape (DLT). Each event was written to one of 10 DLTs. Each DLT can hold about 15 Gigabytes of data. Although the trigger system makes efficient decisions about which events to write to tape, there was still an enormous amount of raw data recorded. The purpose of the data split is to seperate the raw data by trigger type and level 3 tags into small sets of output tapes. All the hyperon triggers were split off to about 60 DLTs. The tape names in KTeV database were called UPH01 to UPH60. This is the data I study.

Chapter 4

Event Reconstruction

The Event reconstruction is very crucial to the data analysis. Roughly speaking, the event reconstruction proceeds as follows. First, track candidataes in the x- and y-views are indentified. If the right number of track candidates were found (it depends on different runs), then the energy clusters in the CsI are reconstructed. Correction to the tracks were then calculated and kinimatic quantities evaluated.

In this chapter, a track-finding algorithm using drift chamber hits to reconstruct the trajectories and momenta of chaged particles will be discussed. Then we will discuss the CsI clustering algorithm which reconstructs the energies of clusters in the calorimeter.

4.1 Tracking

An algorithm, called "T3" tracking algorithm, was developped for finding the track candidates. We will discuss about how the charged particle tracks in the spectrometer are reconstructed.

4.1.1 Hit pairs and SODs

When a charged particle went through the spectrometers, it caused the ionization and avalanche, and the signals were recorded. The first task to the tracking code was to find the drift distance of the track to nearest wires.

At first, this information was extracted from the raw drift chamber TDC hits by subtracting a wire-dependent time offset from the TDC value, and then using a look-up table to map the time to a drift distance. If hits are outside a 170 ns wide time window, they are considered to be out-of-time. No drift distance is calculated for such hits. Only the first in-time hit on each wire is used.

When we discussed the detector part earlier, we noted that there are two complementary planes in each view of the drift chamber. If a charged particle left a hit in both planes of a pair, the two hits were considered a "hit pair". The tracking code would deal with them according to the quality of their "sum of distances" (SODs). Since the two planes in each view were offset by half a cell spacing, or 6.35 mm, the SOD of any hit pair should be equal to this distance, within resolution. Drift distance resolutions are typically $\simeq 100\mu m$, so the SOD resolution used is $\sim 140\mu m$.

Different hit pairs were classified according to their SODs as shown in Fig. 4.1. There were several kinds of SODs, e.g. "good SODs", "Low SOD", "High SOD" and "Isolated SOD". Detailed discussion of SOD can be found [48, 49, 50]

For the "Good SOD", here it means that the hist pair is close to the nominal 6.35 mm within 1 mm, and "Low SOD" pairs where the SOD was less than 5.35 mm. This low value could be due to the traversal of two tracks through the same

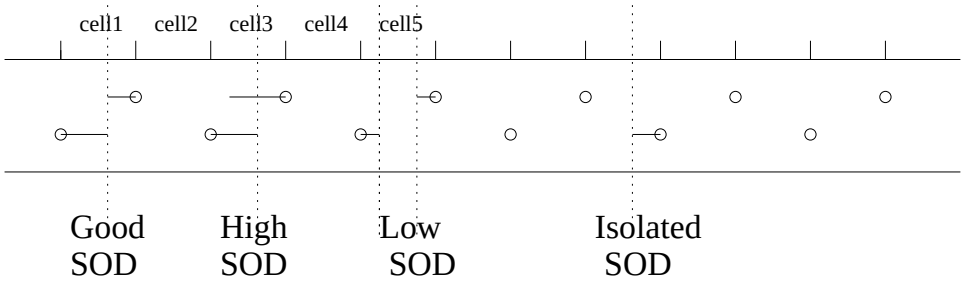

Figure 4.1: Beam view of the KTeV CsI calorimeter array.

cell. This causes the SOD to be low because each sense wire sees the charge from the nearest track, resulting in a SOD lower than the nominal value. Another possibility of the Low SOD was due to a single track which emits a δ-ray, from an electron knocked off an atom.

The "high SOD" pairs where the SOD was greater than 7.35 mm. These pairs can arise when a tracks pass close to a wire in one of the complementary planes. They were also caused by infficiencies near the sense wire due to radiation damage and insufficient signal gain.

The "Isolated SOD" hits carry information only on the distrance from the track to one side wire, but not its opposite direction. Basically it was due to intrinsic infficiencies in the drift chamber planes because of defects on the sense wires. There was no measurable SOD for isolated hits.

Figure 4.2 shows a typical sum-of-distances plot.

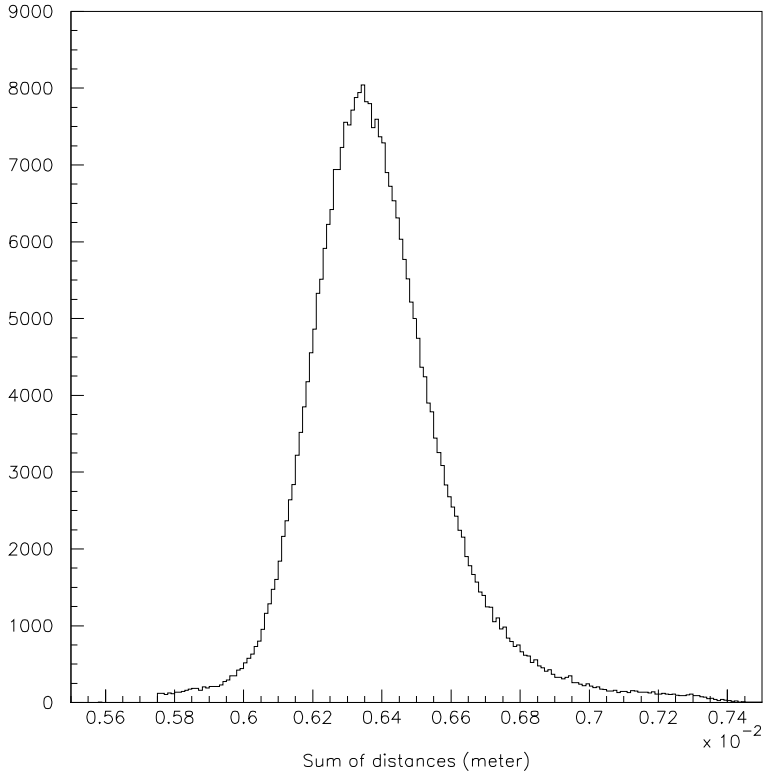

Figure 4.2: A typical Sum-of-Distances distribution in Chamber 1, X view. The mean of the distribution should be the constructed cell size of 6.35 mm and the width is proportional to the resolution.

4.1.2 The X and Y Track Candidates

After the hit pairs were identified and a quality SOD was calculated for them, the next step in the tracking algorithm was to look for track candidates. Track candidates were searched separately in the x and y-views. No constraints were placed on track candidates at this stage; up to now, they were not required to originate from the beam or to point to the calorimeter, and the same hits or hit pairs maybe be shared by more than one trcak candidate.

4.1.3 Finding Y tracks

We know that the analysing magnet's field is in the y direction in our coordinate system, so it didn't bend the particles in the y plane. This property made the y track algorithm more straightforward.

The algorithm looked for one pair of hits in DC1 and one pair in DC4 first, and drew a line between them. Any pairs in DC2 and DC3 which were less than 5mm distance from this line were found and the quality values of the pairs from the four chambers were added. To qualify as a Y track candidate, a track need not have the quality sum of a perfect track (4 good SODs), which is 16 (4 good SODs $\times$ quality value of 4 per good SOD). If the sum was 11 or larger, the four pairs were considered as a Y track candidate. Here the sum of 11 corresponded to two good SODs, one low or high SOD, and one isolated hit.

After passing the quality sum test, it still needed to pass the χ^2 per degree of freedom fit-criteria, and it was required that the χ^2 was less than 4 mm^2, this would then be accepted as a y-track.

After all the Y track candidates are processed, the tracking algorithm decided whether to keep or reject the event.

4.1.4 Finding X tracks

The analyzing magnet bent the charged particle in the x-view, so findig the x track candidates was more complicated. The hit pairs in the x-view of the upstream and downstream chambers had to be examined independently.

The tracking algorithm first found track segments in the x-view between DC1 and DC2. The same was done for DC3 and DC4.

A line was drawn between each pair in DC1 and DC2. If the quality sum of the hit pairs is at least 4 and the line made an angle of less than 100 μ rad with respect to the Z axia, the pair qualified as a X track segment. We did same procedure for DC3 and DC4, but with the sum of the quality balues must be 5 or greater and angle with respect to the Z axis may not exceed 150 μ rad.

The x-track candidate was then defined as any combination of a downstream segment with an upstream segment which matched at the plane of the magnet kick with a separation distance smaller than 6 mm.

4.1.5 Track Vertex Candidates

At this point, there are at least two X and two Y track candidates that have been identified. The z positions where each pair of Y track candidates intersect are calculated, and the same is done for X track candidates. The algorithm then finds all combinations of two track candidates in each view intersecting at the same z

and located within the decay area. This is defined to be a vertex candidate. Requirements are kept fairly loose, so that some events have many vertex candidates. The two X tracks in a vertex candidate are required to bend in different directions at the analysis magnet, consistent with the hypothesis of two oppositely charged particles.

Up to now, it is impossible to decide which of the pairing combinations that result is the right one, since each Y track candidate can be paired with either of the two X track candidates. CsI calorimeter cluster position information is required in order to resolve this ambiguity.

4.1.6 Track-Cluster matching

The ambiguity caused by only using the DC would be solved by checking the calorimeter cluster information.

By searching for the closest cluster to the projected position at the CsI of each x-track/y-track combination, we obtain the help in vertex finding. The distance separation between the position of the track (x,y) at the calorimeter and the position of the cluster (known as track-cluster separation) was required to be less than 7 cm, in order to accept the matching.

For each vertex candidates, it was then determined whether the tracks matched to clusters in either (or both) of the two X-Y matching cases. For hyperon decays, one (and only one) track had to go down the beam holes in order to be triggered. In this case an x-track and a y-track were matched within a beam hole and no CsI cluster could be used.

Any cluster with energy above some threshold (3 GeV for Cascade beta decay) and not matched to a track was counted as an "extra cluster". Extra clusters were candidates for photons.

4.2 Cluster Finding, HCC algorithm

The HCC algorithm was designed to determine the number of isolated showers depsosited in the CsI calorimeter.

The basic idea of this algorithm is that an isolated cluster could be enclosed by a continuous perimeter. To make the perimeter, only the crystals which contained the energy above 1 GeV, based on the information from the E_t board, were used.

While traveling clockwise around the perimeter, if we assign $+1$ for every right turn and -1 for every left turn, the sum of right turn minus left turn should be four because our CsI calorimeter consists of rectangular crystals. If we apply this procedure to the whole calorimeter, the resulting number of right turns subtracted by the number of left turns should be four times the number of clusters.

The cluster finding algorithm took advantage of a pattern recognition and parallel processing technique to reach a relatively fast decision making under 2μsec.

Right or left turns were determined by examining the pattern of the hits in 2×2 arrays. Figure 4.3 shows all the possible configuration of hits in such a group and the assigned number for each pattern. Since each crystal belonged to four different 2×2 grids, each crystal was used to determine four different pattern values. The sum of all 2×2 pattern value was four times the number of isolated clusters in the arrays. The outer edge of the calorimeter as well as the boundary of the small

Patterns of Struck Blocks	Pattern Value
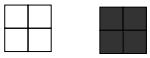	0- No turns
	+1 -one right turn
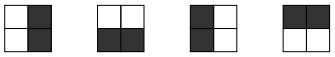	0- No turns
	-2 - Two right turns
	-1 -one left turn

Figure 4.3: Possible patterns for a 2×2 array of blocks.

and large blocks of CsI in which the 2×2 arrays contained a mixture of the two different sizes were treated in a special manner. Detailed discussion of the HCC algorithm can be found in [34, 35].

4.2.1 Cluster Position

The cluster shower generally covered several crystal blocks, and we need to find out where the center is. The distribution of energy deposited in the blocks of a cluster can be used to deduce where the particle struck the calorimeter. Ratios of the energy in the cluster seed block (The crystals with the greatest energy of all the neighbors were made cluster seeds) to the energies in neighboring blocks were first calculated. These ratios were compared to values in look-up tables, which return the x and y coordinates of the cluster position. There were a total of 12 tables, 6 for the small crystals, and 6 for the large ones, covering 6 different energy

regimes. To make these lookup tables, the $K_L \to \pi^+\pi^-$ data and Monte Carlo are used. The resulting position resolution is $\sim$ 1 mm in small blocks and $\sim$ 1.8 mm in large blocks [51].

4.3 Energy Measurement in CsI

KTeV used a set of lookup tables to reconstruct the energy of the incident particles. Just like the lookup table for position measurement, it was created from the $K_L \to \pi^+\pi^-$ data and Monte Carlo. There were several kinds of correction algorithm/methods applied to different situations.

Overlapping clusters were separated, i.e. the crystals which had contributions from multiple particles had their energy split by also looking at the table.

The readout threshold for crystals was 7 MeV. The outer crystals in a cluster often have energy below this threshold and were removed from the readout list. Becuase these crystals were not counted toward the cluster energy, it would slew the sum downwads. The threshold correction was applied to rectify this problem. For each cluster, the amount of energy deposited in crystals below the readout threashold is estimated. This correction is a function of the overall cluster energy and the crystal position in the cluster.

There were also some other corrections which were applied to the CsI, such as Intra-Block correction, Non-Linearity Fudge Correction, etc.

The total energy of the cluster was corrected for the energy leakage outisde of crystal array, through the back of those crystals, and energy loss in the wrapping materials based on a study by using GEANT simulation. The fraction of the miss-

ing energy was independent of the energy of the incident particle, and depended only on the size of crystals, 1.042 for the small and 1.059 for the large crystals (also for boundary region of large and small crystals), respectively.

4.4 Electron and π^- identification

4.4.1 Using CsI Calorimeter

For high energy decayes, there are 2 most important decay particles, one is electron, and the other is π^-. Both of them have the negative charge, but they have very different properties on some aspects. There are lots of experimental ways to tell them.

In KTeV, the CsI calorimeter was 27 radiation lengths X_0 long, so the electrons deposited most of their energy to the calorimeter in constrast to pions which deposited a small fraction of their energy because the CsI only had 1.4 nuclear interaction lengths long. This enabled us to identify electrons by looking at the E/P in the calorimeter, here E was the measured energy, and p was the measured momentum by spectrometer.

Here are some typical plots. The top plot in Figure 4.4 shows the E/p distribution in data. The low E/p tail was due to pions, and the high side tail was caused by overlapping clusters. Also shown is the E/p distribution in $K_L \to \pi^\circ\mu^+\mu^-$ MC. We required the E/p to be unity within $\pm 5\%$ which was roughly 5σ of a Gaussian fit to the signal simulation. The π/e separation factor obtained from the E/p requirement was estimated from data sample identified as $K_L \to \pi^+\pi^-\pi^\circ$.

The bottom plot in Figure 4.4 shows the E/p distribution for two charged

particles in $K_L \to \pi^+\pi^-\pi^\circ$ events. With our requirement, 99.6% of charged pions were rejected, whereas the efficiency for single electrons was calculated to be 93.7% from MC. Since we required two electrons to be identified in the signal, the efficiency for this requirement was 87.8%.

After we used E/P, there were still π^- remaining. We know that π^- deposited the energy mostly through hadronic interaction, instead of electromagnetic interaction by electron. The shower radius of these two interactions are pretty different. For electromagnetic interaction by electron, the shower lateral spread is characterized by the Moliere radius:

$$R_m = (21MeV) \times X_0/E_c \tag{4.1}$$

95% of the shower energy is within $\pm 2R_m$. For the hadronic activity, the transverse dimension in the hadronic shower tends to be larger than that in the electromagnetic shower. This difference in the transverse shower shape allowed us to discriminate electrons from pions. We can define the χ^2_{shape} as

$$\chi^2_{shape} = \frac{1}{N}\sum_{i=1}^{N}(\frac{E_i - E_i^{pre}}{RMS_i})^2 \ , \tag{4.2}$$

where N is the number of crystals in a cluster, E_i is the real energy in i-th crystal, E_i^{pre} is the expected energy from the electromagnetic shower, and RMS_i is the expected RMS for the i-th crystal. We can study the χ^2_{shape} variable from MC to make the appropriate cuts to distinguish these two particles.

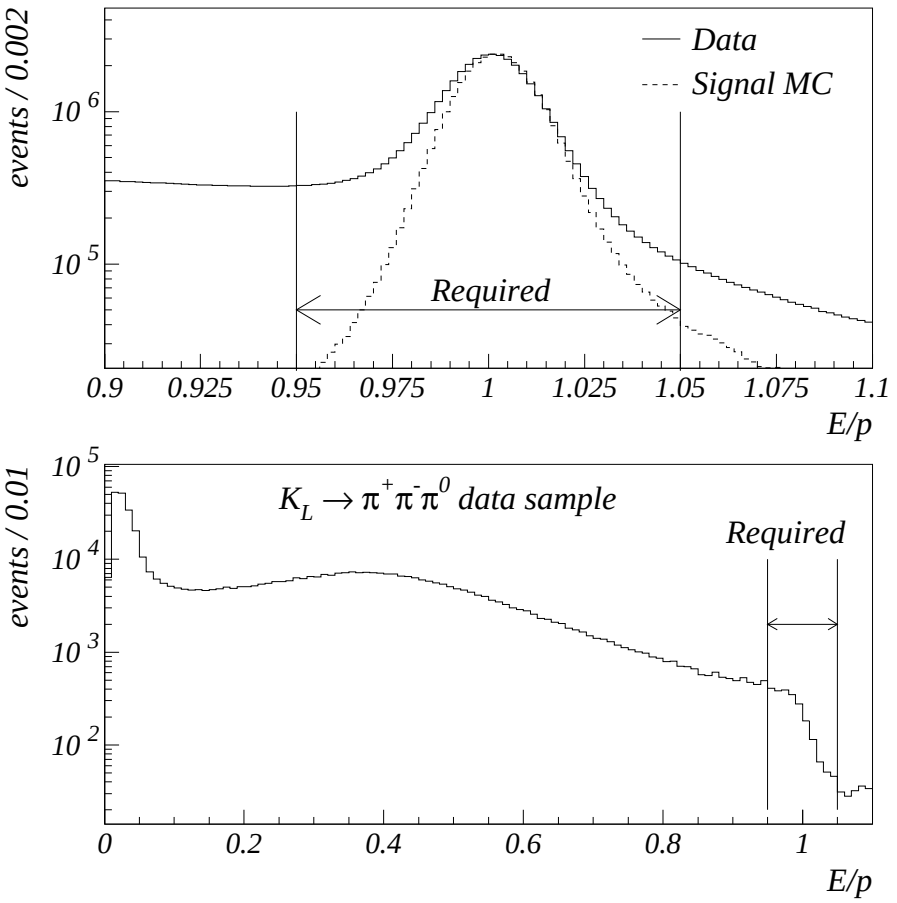

Figure 4.4: The top plot shows the E/p distribution for charged particles in data. Our requirement is indicated by the arrow. The bottom plot shows the E/p in data sample identified as $K_L \to \pi^+\pi^-\pi^\circ$, thus for charged pions.

4.4.2 Using TRD

In KTeV, there was a 2nd device for the pion rejection, Transition Radiation Detectors (TRDs). Please refer Section 2.4 about the detail information.

Chapter 5

Monte Carlo Simulation and Background Studies

MC simulation is very important in the data analysis. First, it will help us to get the acceptance ratio of signal and normalization mode, based on this we can get the flux of these modes. Second, MC will help us to simulate the background events. Third, MC will also help us to study various analysis cuts for event selection.

In KTeV, the output of the MC had the same format as the real data. This was important and helpful. It allowed us to use the same algorithm and software to analyze MC as real data.

In this chapter, I will discuss some fundmental MC simulations, such as kaon and some hyperon decay modes. Also I will discuss the simulation of the detector response, including the accidental activity or noise in the detector.

5.1 3 Steps of Event Generation

In KTeV, the event generation in the simulation can be devided into 3 parts, beam production at the target, decays of the particles, and propagation of the decay products. So in the next sections, we will discuss these 3 steps one by one.

5.2 MC of Beam Production at target

5.2.1 Hyperon Production

This thesis's purpose is to study the Ξ° hyperon decay mode, so let's see the hyperon production first. The production of $\Xi^{\circ}$by the proton beam is given by Pondrom [14, 15]:

$$E\frac{d^3\sigma}{dp^3} = exp(C_1 + C_2x^2 + C_3x + C_4xp_t + C_5p_t^2 + C_6p_t^4 + C_7p_t^6) \times (1-x)^{C_8+C_9p_t^2} \quad (5.1)$$

where $x = p/E_B$, p is the produced particle momentum, E_B is the beam energy, p_t is the transverse momentum of the produced particle relative to the incident beam direction and E is the energy of produced particle.

This formula was determined experimentally by Lee Pondrom from Fermilab Meson Center, so the coefficients are called the Pondrom parameters. Please refer the table 5.1.

In KTeV MC, the Λ spectrum was tuned so that the spectrum measured in $\Lambda \to p\pi^-$ events matched to that in MC. As a result, the MC spectrum was scaled by 90% in E. For Ξ^0, the Pondrom production spectrum paramters were used without corrections. The decay position of hyperons was simply determined by their proper lifetimes and their momenta.

5.2.2 Kaon Production

We know that after the 800 GeV proton beam hit the the BeO target, there were more kaons than hyperons, so the kaon decay modes were likely the important background.

Table 5.1: Coefficients in empirical fits for hyperon spectrum.

	Be $\to \Lambda$	Be $\to \Xi$	Be $\to \bar{\Lambda}$	Be $\to \bar{\Xi}$
C_1	1.68	-1.21	1.45	0.61
C_2	0.44	1.16	-0.79	18.1
C_3	0.28	-0.72	1.28	-22.5
C_4	-0.58	-0.48	-1.09	-1.46
C_5	-2.62	-1.85	-2.21	-1.24
C_6	0.40	0.17	0.45	0.00
C_7	-0.03	-0.008	-0.07	-0.00
C_8	0.86	2.87	0.74	-
C_9	0.20	0.04	0.61	-

Malensek [52] gave the parameterization for the K^+ and K^- spectrum for 400 GeV/c protons incident on a beryllium target. In this parameterization, the number of kaons with momentum p into a solid angle dΩ was:

$$\frac{d^2N}{dpd\Omega} = \frac{E_B}{400} B x \frac{(1-x)^A(1+5e^{-Dx})}{(1+p_t^2/M^2)^4} \tag{5.2}$$

$x = p/E_B$, and p is the kaon momentum, E_B is the beam energy, and p_t represents the transverse momentum of the produced particle relative to the incident beam direction. p and p_t are expressed in units of GeV/c. B, A, D, and M^2 are constants which were got experimentally (Table 5.2).

Table 5.2: Values of parameters describing the kaon production spectrum [52].

	K^+	K^-
A	2.924	6.107
B	14.15	12.33
M^2	1.164	1.098
D	19.89	17.78

Using quark-counting arguments (see reference [53] for example), K° and $\bar{K}^\circ$ production can be related to K^+ and K^-:

$$N_{K^\circ} = \frac{N_{K^+} + N_{K^-}}{2} \tag{5.3}$$

$$N_{\bar{K}^\circ} = N_{K^-} \tag{5.4}$$

People still need to tune the spectrum further, to match kaon momentum measured by $K_L \to \pi^+\pi^-$ events in the real data. The details can be found elsewhere ([54], [53], [55]).

5.3 Simulation of Decay Process

Once the decay vertex was found for a specific decay mode, the next step was a decay of the parent particle. The basic KTEVMC simulated Λ and Ξ^0 hyperon decays assuming unpolarized hyperons, and decays were generated according to a a isotropic phase space. Also the user could enable the following features [56]:

- The polarization of Λ and Ξ^0 hyperons produced at the target.
- Distribution of decay products according to physics form factors as in: $\Lambda \to p\pi^-$, $\Lambda \to pe^-\overline{\nu}$, $\Xi^0 \to \Lambda\pi^0$, $\Xi^0 \to \Sigma^+e^-\overline{\nu}$, $\Sigma^+ \to p\pi^0$, $\Xi^0 \to \Lambda\gamma$, $\Xi^0 \to \Sigma^0\gamma$, $\Sigma^- \to n\pi^-$, $\Lambda \to n\pi^0$, $\Sigma^0 \to \Lambda\gamma$.
- Polarization of decay products from hyperon decays as in: $\Sigma^0 \to \Lambda\gamma$, $\Xi^0 \to \Lambda\gamma$, $\Xi^0 \to \Sigma^0\gamma$, $\Xi^0 \to \Sigma^+e^-\overline{\nu}$, $\Xi^0 \to \Lambda\pi^0$.
- Production of anti-hyperons: $\overline{\Lambda}$ and $\overline{\Xi^0}$
- The decay $\Xi^0 \to \Lambda\pi^0$ with $\Lambda \to pe^-\overline{\nu}$ and the decay $\Xi^0 \to \Lambda\pi^0$ with $\Lambda \to p\mu^-\overline{\nu}$
- The decay $\Xi^0 \to \Sigma^+\mu^-\overline{\nu}$

Here, the 'polarization' means the ensemble average of the polarization vector of the particle in its own rest frame. The magnitude of this polarization vector is

equal to the amount of polarization, so a polarization of $\vec{P_\lambda} = 1.0\hat{z}$ refers to 100 % polarization in the z-direction in the particle's rest frame.

5.3.1 Distribution of Hyperon Non-Leptonic Decays

A lot of hyperons went through the decay mode like this: $B \to B'\pi$, where B and B' are initial and final state baryons, the final state baryon is distributed according to

$$\frac{1}{\Gamma} \cdot \frac{d\Gamma}{d\Omega_{B'}} = \frac{1}{4\pi} \cdot (1 + \alpha \vec{P_B} \cdot \hat{p_{B'}}) \tag{5.5}$$

where α is the decay asymmetry , $\hat{p_{B'}}$ is the unit vector of the final state baryon direction in the rest frame of initial state baryon, and $\vec{P_B}$ is the polarization vector of the initial state baryon. The numerical values of α for these decays can be found in [8]. The decays which implemented this were:

$\Xi^0 \to \Lambda\pi^0$, $\Lambda \to p\pi^-$, $\Lambda \to n\pi^0$, $\Sigma^+ \to p\pi^0$, $\Sigma^- \to n\pi^-$,

For anti-hyperon non-leptonic decays, we need to replace $\alpha \to -\alpha$ [14] with the same formula for decay distribution.

5.3.2 Polarization of Hyperon Non-Leptonic Decays

KTeV hyperon group [16] also did a study of the polarization direction in the production of cascade particles. For the decay $\Xi^0 \to \Lambda\pi^0$, where the Λ decays into $p\pi^-$, the polarization of the Λ is determined by the expression

$$\vec{P_f} = \frac{(\alpha + \vec{P_i} \cdot \hat{u})\hat{u} + \beta(\vec{P_i} \times \hat{u}) + \gamma(\hat{u} \times (\vec{P_i} \times \hat{u}))}{1 + \alpha \vec{P_i} \cdot \hat{u}} \tag{5.6}$$

Where α, β, γ are decay parameters, $\vec{P_i}$ and $\vec{P_f}$ are the polarizations of the initial and final state baryons, and $\hat{u}$ is the direction vector of the final state baryon in the rest frame of the initial state baryon.

For anti-hyperon non-leptonic decays, the same formulae are used with the replacement $\alpha \rightarrow -\alpha$, $\beta \rightarrow -\beta$, $\gamma \rightarrow \gamma$ [14] .

This topic is beyond the scope of this thesis. Please refer the paper/writeup "Ξ° and $\bar{\Xi}^\circ$ Polarization Analysis at KTeV E799II" [16] about the detailed discussion of the polarization of Ξ°.

5.4 Detector Response

After the decay event was randomly generated, the nect step is to trace the decay products through the detector. The tracing process is terminated when the particle is stopped in a detector component, it decayed, converted or the particle escaped the detector volume. The detector response must be simulated for this purpose. In addition, the response had to be correctly digitized so that analysis code would work for both real data and MC data with the same cuts. Especially for DPMT, the simulation of digitization was a crucial point to reproduce the calorimeter response. This section describes the simulation of responses in main detector elements.

5.4.1 Drift Chamber

When charged particles traveled through the drift chambers, the hit locations are found by selecting the closest sense wires. Then the drift distance, i.e. the distance

from the particle trajectory to the closest wire in each of the two complementary planes, was converted to the drift time. The conversion factor was calibrated in advance so that the sum of drift distances in the two complementary planes (SOD) equaled 6.35 mm (Section 4.1.1). The drift time was smeared based on the calibration result, and was recorded as TDC counts. The inefficiency for each plane was implemented by not recording the hit information randomly. Only the earliest hit in multiple hits was recorded if they were within the same time window of 235 ns.

The δ-ray emission in the chamber gas was simulated in the following 3 steps. First, when a highly relativistic particle is passing through the length L(m), the emission probability in a material with Z(Atomic Number) and A(Atomic Mass) is;

$$P = 154(\mathrm{KeV}) * \frac{Z}{A} * d(\mathrm{g/cm^3}) * L(\mathrm{cm}) * \frac{1}{E} \ , \tag{5.7}$$

where d represents the density of material and E is the δ-ray energy. With this probability, P, a δ-ray was emitted perpendicular to the parent particle trajectory. Its range was determined based on the emitted energy. If the electron emitted as the δ-ray stopped outside the original cell, the flight distance was considered as the size of the cell. At last, the distance from the δ-ray to the closest wire was computed. The hits due to the δ-ray were also recorded by the same method used for normal charged particles. The resulting hit information was used in the Level 1 for $DC1$ and $DC2$ simulation, which counted the number of hits in the defined in-time window (235 ns).

5.4.2 TRD's

Particles pass through the TRDs after DC4. The eight planes of the TRDs are simulated as $0.115X_0$ amount of material. In the beam region, which contains no radiator material, $0.04X_0$ is assumed. Photon conversion in the TRDs is simulated, but scattering off the individual TRD wires is not. The pion rejection and electron tagging performance of the TRDs are not simulated, but are instead measured using data.

5.4.3 The Trigger Hodoscopes

After the TRDs, the particles are transported to the trigger hodoscopes. If a charged particle hits a scintillator paddle in V or V', the latch bit corresponding to the firing counter was set based on the efficiency of the counter measured from real data. The latch bit was used to simulate Level 1 triggering.

5.4.4 CsI Calorimeter

Different particles gave different effects when the particles impinged on the face of the calorimeter. Electrons and photons produced electromagnetic showers. Muons deposited minimum ionizing energy in the calorimeter and passed through the calorimeter. Pions could leave minumum inonizing energy or initiate a hadron shower. The simulation of the CsI calorimeter first determined the energy deposited to each crystal, based on the kinds, energy, and position of a particle hitting the calorimeter. Once the deposited energy was determined in an event, the scintillation light yield was simulated, and was digitized. The triggering de-

vices, E_{tot} and HCC were also simulated using the result of the simulation for the calorimeter.

Shower in CsI

In our MC simulation, when electron(or photon) reached the CsI, the transverse position was defined at shower mean depth approximated by;

$$z_e\,(\mathrm{m}) = 0.11 + 0.018 \times \ln \mathrm{E}\ , \tag{5.8}$$

$$z_\gamma\,(\mathrm{m}) = 0.12 + 0.018 \times \mathrm{lnE}\ , \tag{5.9}$$

where E is the energy of electron (or photon) in units of GeV.

Electromagnetic showers were simulated using a shower library generated using GEANT. Using the transverse position and energy of electron or photon as inputs, the energy deposited in CsI crystals was derived from lookup tables referred to as the shower library. The shower library was created in advance by collecting the CsI response for electrons in K°_{e3} events in which the position and momentum of electrons was measured by the spectrometer.

The shower library was segmented in depth(z) with 25 bins, and binned in energy: 2, 4, 8, 16, 32 and 64 GeV, and binned in position. Each 2.5 cm $\times$ 2.5 cm crystal had six sizes of the position bin, which varied from 0.2 mm $\times$ 0.2 mm to 0.7 mm $\times$ 0.7 mm with a difference of 0.1 mm with respect to the length of the side. The shower library was composed of 13 $\times$ 13 small (=2.5 cm $\times$ 2.5 cm) CsI crystal array. The segmentation in z was intended to correct for the position dependence along z of the light yield in each crystal. The correction factor was

obtained before the installation of the CsI crystals by using cosmic ray muons. Once a sample shower was picked from the shower library, the energy scale was normalized to original energy of the particle incident on the CsI.

The same shower library was used for both 2.5 and 5.0 cm crystals. If any 5.0 cm crystals were present in the shower, they were treated as four 2.5 cm crystals. This simplified the treatment around the boundary between the two different crystal sizes.

For charged pions, the position was defined at the surface of the calorimeter. As for e/γ, the CsI response for pions was derived from a shower library created by GEANT simulation.

For a muon, deposited energy was determined by Landau distribution based on dE/dx in the 50 cm long CsI.

Digitization

After deciding the energy deposited in each crystal, the Monte Carlo simulated the digitization process. It started with the simulation of the scintillation light yield, and then the light was converted to charge. Finally, the charge was digitized to ADC counts.

The CsI time spectra were modeled with three exponential decays, in which two were fast components with roughly 10 and 40 nsec decay constants. The other had a decay constant of order 1 μsec. Based on the pre-measured time constants, the timing on the scintillation was smeared. Because the DPMT operation was synchronized with accelerator RF, time jitter in the CsI signal with respect to the

RF must be also simulated. The time jitter was modeled by Gaussian distribution with a sigma of 0.6 nsec [53], which was applied to all the CsI crystals on event-by-event basis.

After the determination of energy ratio for each slice, the energy in each slice was smeared individually with photo-statistics. The number of photo-electrons per GeV, $N(p,e)$, had been measured for each crystal. The energy was smeared by Gaussian whose width was defined as;

$$\sigma(E) = \frac{E}{\sqrt{N(p.e)}}\,. \tag{5.10}$$

The least count of DPMT was equivalent to 0.6 MeV, and the CsI crystal had typically 20 photo-electrons per 1 MeV, so that one count corresponded to roughly 12 photo-electrons. Therefore, the Gaussian approximation for the fluctuation was considered as sufficient.

Next step was to convert the smeared energy into charge. It was simply translated using the constants for each crystal which was calibrated with real data. The electrons with well measured momentum from K°_{e3} decays were used for this calibration.

The final part of the calorimeter simulation was the digitization of charge in each slice, QIE simulation. The constants obtained from laser calibration were used to simulate the QIE, which were: slopes and intercepts for each capacitor, range, and crystal; the errors in slopes and offsets; the pedestals for each capacitor and range. Each central value was smeared with the error in the set of constants.

E_{tot} and HCC

At this moment, the energy deposited in each crystal, which was the input to E_{tot} and HCC simulation, was reproduced. The energy only in the in-time slice[1] was used for the E_{tot} simulation. Summing over the energy for the whole calorimeter formed the E_{tot} signal, to which a threshold was applied. HCC was simulated by tabulating crystals whose in-time energy was above the HCC threshold. The completed table was sent to the cluster counting algorithm already described in Section 2.7.

5.5 Accidental Activity

Beam interaction, cosmic rays, and debris from the target and vacuum window, etc. can all contribute to accidental activity in the detector. They are recorded to tape using an accidental trigger uncorrelated with detector activity from the desired decay mode. It must be added on an event-by-event basis and should be independent of the decay of interest.

In order to simulate the accidental activity in the Monte Carlo, the data collected by the Accidental Trigger was overlaid on the generated MC event with the following procedure. After the event generation, all the detector's response was recorded as ADC counts, TDC counts and latch bit by digitization. Then, the digitized quantities in an accidental data event were added to the MC data. ADC counts were simply summed together, latch bits were ored, and only the first

[1]The read out slice was synchronized with accelerator RF. We refer to the slice with the same phase of "in-time bucket"(Section 3.1) as "in-time" slice.

hit in TDC readings was kept. Once the accidental data were appended, trigger requirements for each counter were tested again.

The accidental effect was crucial in the small branching decay mode analysis especially. First, it affected the acceptance calculation for some decay mode, e.g. it can fake some events. Also the accidental activity contributed to the magnitude of the background level. For example, in my signal mode, an accidental photon might fake a signal. Here the simulation of the detector's accidental activity was crucial to evaluate correctly the background level.

Chapter 6

The Normalization Mode $\Xi^\circ \to \Lambda^\circ\pi^\circ$ Analysis

In order to calculate the branching rate or upper limit for a decay mode, one can use a formula like this:

$$BR_{signal} = BR_{norm}\frac{N_{signal}}{N_{norm}} \tag{6.1}$$

Here, N_{signal} or N_{norm} is the total number of signal or normalization mode events which the KTeV detector can see, as corrected for acceptance. With the notation N'_{mode} for the event number after the analysis cuts and A_{mode} for acceptance after cuts, N_{mode} is like this:

$$N_{mode} = N'_{mode}/A_{mode} \tag{6.2}$$

In our analysis, we study the Ξ° hyperon weak radiative decay mode $\Xi^\circ \to \Lambda^\circ\pi^\circ\gamma$. We have to choose a normalization mode for the calculation of the BR. There are several criteria for choosing the normalization mode. It is best if that normlization decay mode is well measured, easy to reconstruct, similar to the signal mode and background free.

From PDG [8] book, $\Xi^\circ \to \Lambda^\circ\pi^\circ$ decay mode has a Branching Ratio of $(99.54 \pm 0.05)\%$. This mode is also very similar with our signal mode, except that the signal

mode has one more γ in the final product. That is why we choose this mode as the normalization mode.

6.1 Data Selection

The data in this analysis came from "hyperon trigger" events. This includes the Sept. 1999 to Jan. 2000 period of data-taking, i.e., the run 14625 to run 15548. There are 60 DLT date tapes, having tape names from UPH001 to UPH060.

6.2 The Reconstruction Methods

Figure 6.1 shows the topology of our normalization mode $\Xi^\circ \to \Lambda^\circ\pi^\circ$ decay in the KTeV apparatus. The detectable final state of the decay is a high momentum proton which remains in the neutral beam and goes down a CsI beam hole, a π^- and two photons which deposit their energy in the CsI calorimeter. We search for the sequence of events $\Xi^\circ \to \Lambda^\circ\pi^\circ$ where $\Lambda^\circ \to p\pi^-$ and $\pi^\circ \to \gamma\gamma$.

What we observe in the detector as a final product of an event which passed the trigger requirements are a positive track going down one of the CSI beam holes of the calorimeter, a negative track associated with one of the electromagnetic clusters in the calorimeter, and two or more extra clusters not associated with any tracks. Assuming thse two extra clusters are decay products of a π°, one can use the following approximation to fix the z position of the π° vertex

$$z = (\frac{\Delta}{m_{\pi^0}})\sqrt{E_1 E_2}\,. \tag{6.3}$$

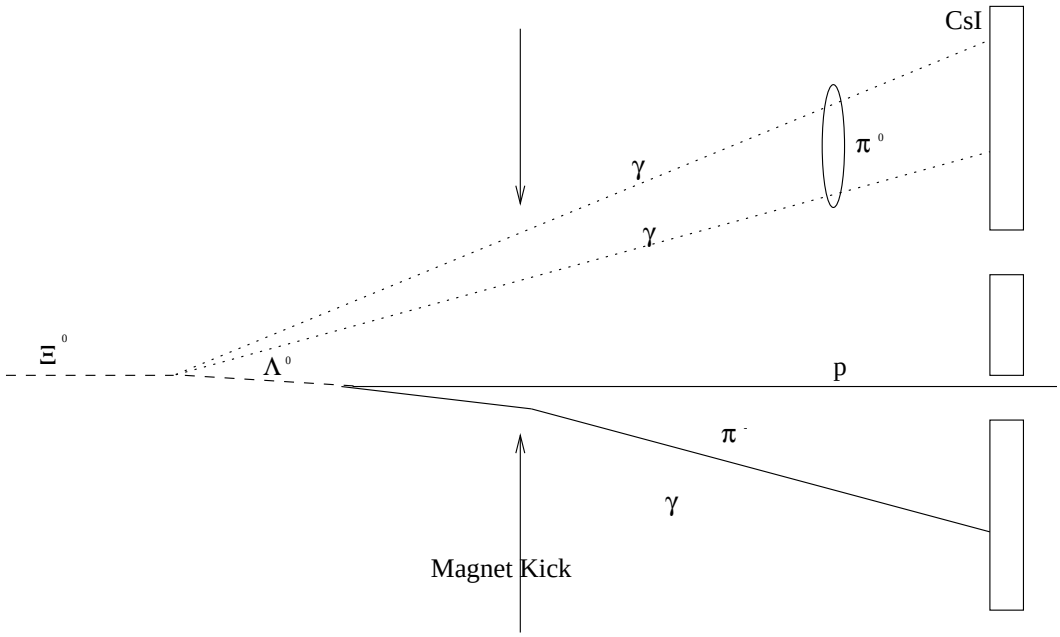

Figure 6.1: The Schemetic drawing of the decay $\Xi^\circ \to \Lambda^\circ\pi^\circ$ where $\Lambda^\circ \to p\pi^-$ and $\pi^\circ \to \gamma\gamma$

E_1 and E_2 are the energies of the photons measured by the calorimeter, and Δ is the distance between the photons at CsI, and m_{π° is the invariant mass of the π°. Here these 2 photons are the prompt decay products of the π°.

From the 2 charged tracks (p^+ and π^-), one can find the $\Lambda^\circ \to p\pi^-$ decay vertex. By extrapolating the Λ direction to the z position of the π° found from the two extra netural clusters, we can fix the Ξ° vertex. Since the π° decays electromagnetically, it has a very short lifetime of 8.4×10^{-17} sec, and one can assume that the Ξ° decay vertex is coincident with the π° decay vertex. Here, I call this sequence of associations the "π° method".

Another optional way to find the Ξ° vertex is by the method called "Center of Gratvity", (CG) method. At first, one finds the center of momentum position

on the front of the CsI for p^+, π^- and two(three) neutral clusters. Then one connects this point with target coordinates $(0,0,0)$ to form a candidate Ξ° track. Extrapolating the Λ to the Ξ° track line which pointing back to $(0,0,0)$, one can get the Ξ° decay vertex. In our coordinate system, one can calculate the z vertex in the $x-z$ or $y-z$ plane. In our case, we simply used the average of these two calculations as z vertex.

Figure 6.2 shows the comparison of these two methods using the $\Xi^\circ \to \Lambda^\circ\pi^\circ$ Monte Carlo simulation events. The top plot is the π^0 method, and the bottom one is CG method. This plot is the z vertex which is constructed by the corresponding method minus the real Ξ° vertex which one can get from Monte Carlo infomation for $\Xi^\circ \to \Lambda^\circ\pi^\circ$ events. From their standard deviations we found out that the π° method is dramatically better than CG method for the Ξ° decay vertex identification. As we know, correct vertex finding is crucial for the event reconstrution. The π^0 method should benefit us more than the CG method.

6.2.1 The cuts for Normalization Mode

To elaborate a list of criteria to select a particular decay mode, we need first to choose a reconstructed variable and compare its distribution between signal and background mode. This reconstructed variable is one that we think can distinguish two or more particular decay modes due to different behaviour in their distributions. In general, we analyze a variable that reveals the differences in topology, kinematics, or particle identification.

This procedure is repeated until the event selection becomes efficient and re-

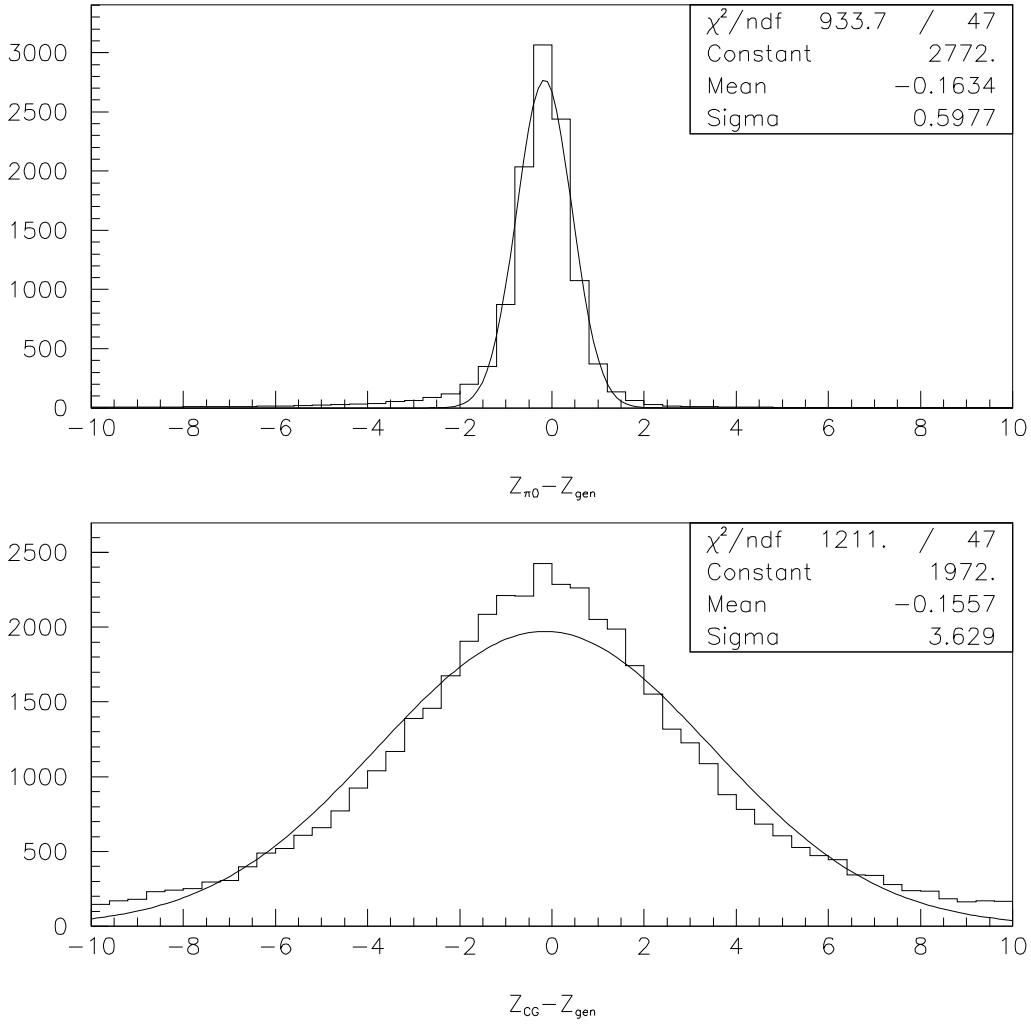

Figure 6.2: The Z vertex comparison of π^0 method and CG method, the top plot is the π^0 method,and the bottom one is CG method.

liable, meaning that the background events are completely eliminated or, if not eliminated, at least understood and under control. The result of this procedure will be a set of selection cuts for a particular decay.

Besides processing the reconstructing technique, one has to come up with a set of quality cuts to reduce background events without losing too much of the signal events. Even though the choice of cuts are suggested by the Monte Carlo (MC) simulations as well as the possible background events, the exact choices of cut boundaries are somewhat arbitrary. One can adjust the values to achieve the best signal to noise ratio. Presented here is a "nominal" set of cuts we applied to the data to select the $\Xi^\circ \to \Lambda^\circ\pi^\circ$ events. We can assign a systematic error to his "arbitrariness" of the cut values.

Here we list the cuts we used for the analysis of the normalization mode. We assume that the two γs decaying from π° have higher energies than a background soft gamma.

General Cuts:

- Number of neutral clusters is greater than one.
- Events only have exactly two tracks. One is a positive charged track, the other is a negative charged track.
- The position of the proton at the CsI face must be inside one of the beam holes by at least 1 cm, and the position of the π^- is outside of the beam holes by at least 1 cm.
- All the γ positions are at least 15 cm away from the π^- position on the CsI

- All the γ positions are at least 15 cm away from each other on the CsI

Vertex Cuts:

- 95.0m $< Z_{\Xi^\circ} <$ 158.0m (inside vacuum decay volume)
- 95.0m $< Z_{\Lambda^\circ} <$ 158.0m, and $Z_{\Lambda^\circ} > Z_{\Xi^\circ}$
- $0.001240 > |x_{\Xi^\circ}/z_{\Xi^\circ}| > 0.000376$
- $0.000430 > |y_{\Xi^\circ}/z_{\Xi^\circ}|$
- $0.001240 > |x_\Lambda/z_\Lambda| > 0.000376$
- $0.000430 > |y_\Lambda/z_\Lambda|$

Momentum and Energy Cuts:

- For two charged tracks, the monemtum ratio $p(+)/p(-) > 3.0$ (exclues kaon decays)
- For the negative charged track, the energy deposited in CsI divided by momentum is < 0.9. (excludes electrons)
- $110 Gev/c < |p_p| < 500 Gev/c$ and $5.0 Gev/c < |p_\pi^-| < 100 Gev/c$
- For the neutral clusters, $E_\gamma > 3.0$ GeV, and $\sum E_\gamma s > 18 GeV$
- $Pt_{\Lambda^\circ\pi^\circ} < 25 MeV/C$
- $Pt_{\Lambda^\circ} > 24.5 MeV/C$ (excludes Λ^0s directly from target)
- CAeneintime < 0.5 Gev (prevents energy loss in beamhole)

- RCeneintime < 0.5 Gev

Invariant Mass Cuts:

- $m_{K_L \to \pi^+\pi^-\pi^0} > 0.55 Gev$

  This cut eliminates the background from the Kaon decay into a $\pi^+\pi^-\pi^\circ$. The event is considered a 3π Kaon decay located at the charged vertex where the two charged tracks are pions. The invariant mass is calculated and the event is kept if it is greater than 0.55GeV.

- $|m_{p\pi^-} - 1.115684| < 0.015 GeV$

Muon System Cut:

- Neither charged track is allowed to match a muon counter hit.

6.3 Data and MC comparison

Fig 6.3 through 6.9 show Data and Monte Carlo comparisons of various distributions. From those plots, we can see that the comparison between data and Monte Carlo simulated events of $\Xi^\circ \to \Lambda^\circ\pi^\circ$ decay showed reasonably good agreement for Trigger 11.

We know that KTeV Monte Carlo V5_05 doesn't simulate the Hadron-Anti veto correctly. Trigger 10 uses HA. For trigger 10, we can see there is some discrepancy between data and Monte Carlo. We deal with the Hadron Anti effects as a systematic error for our analysis. Please refer to Section 2.9.

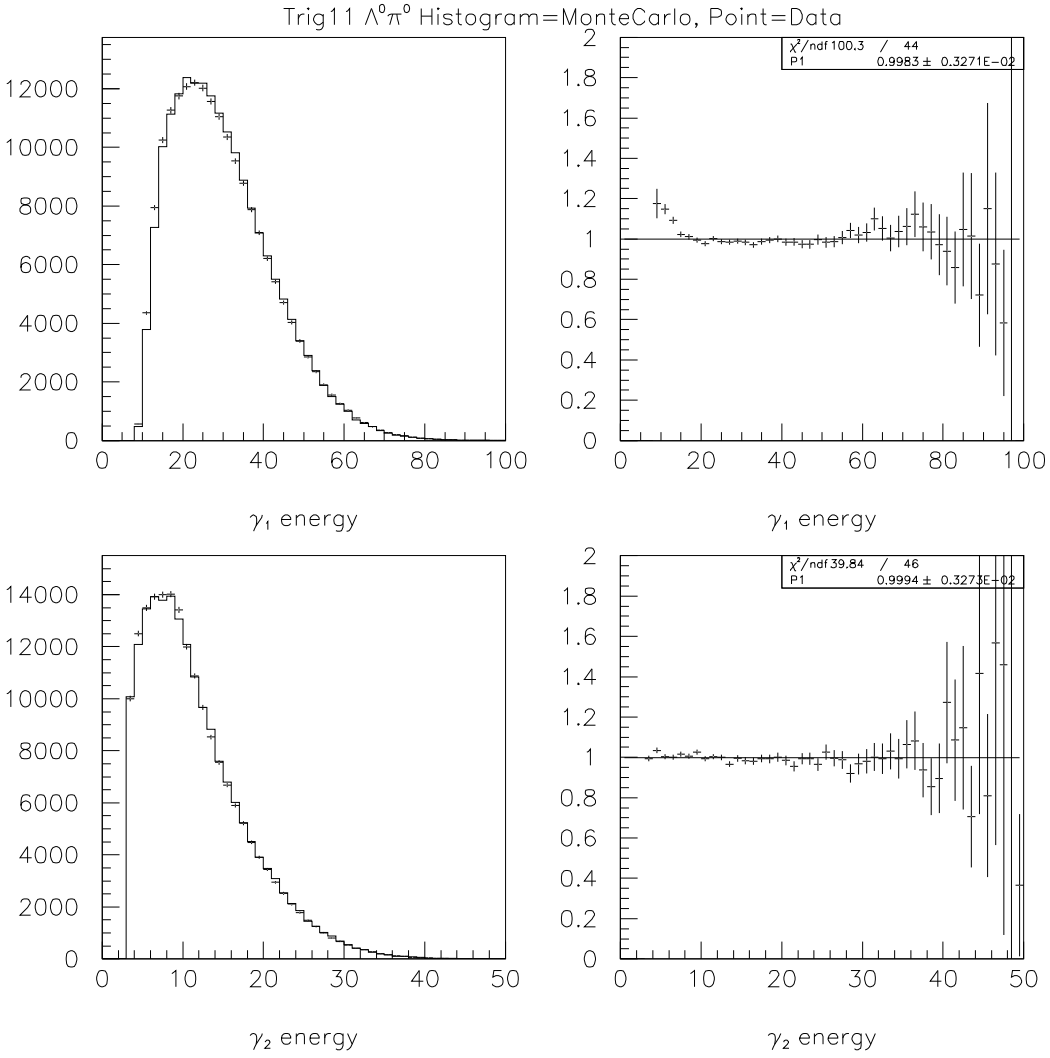

Figure 6.3: Monte Carlo vs. Data for the 2 γs' Energy from $\pi^{\circ} \rightarrow \gamma\gamma$

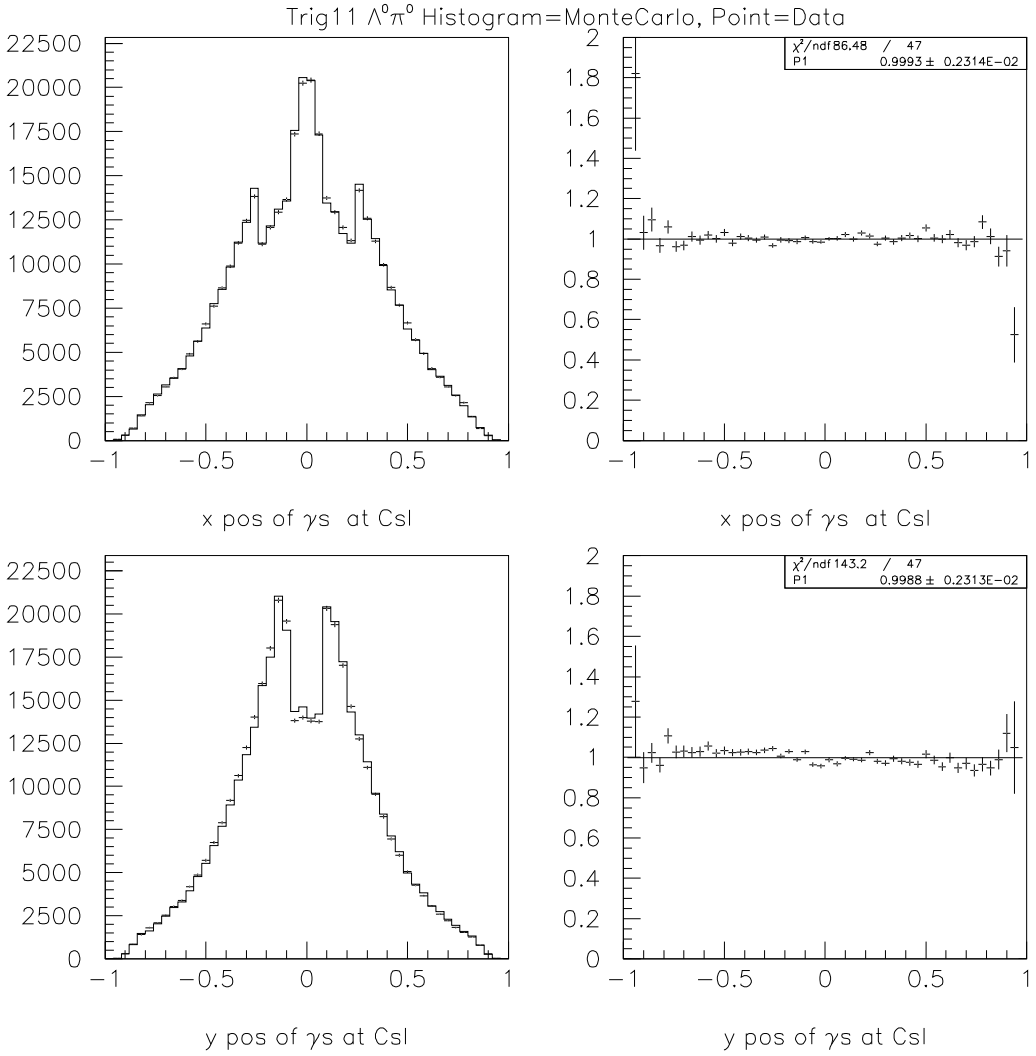

Figure 6.4: Monte Carlo vs. Data for γs' x,y positions on the CsI calorimeter.

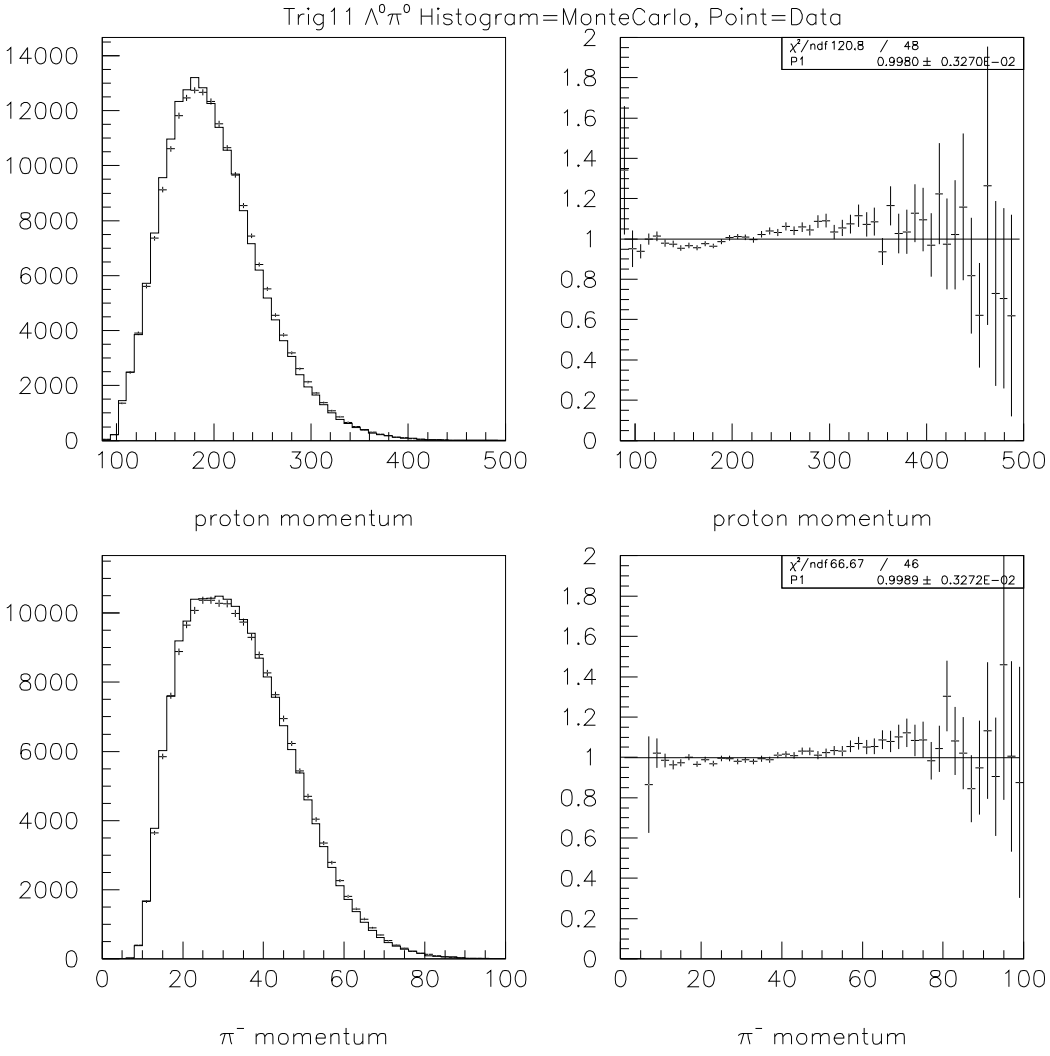

Figure 6.5: Monte Carlo vs. Data for p^+ and π^- momentum.

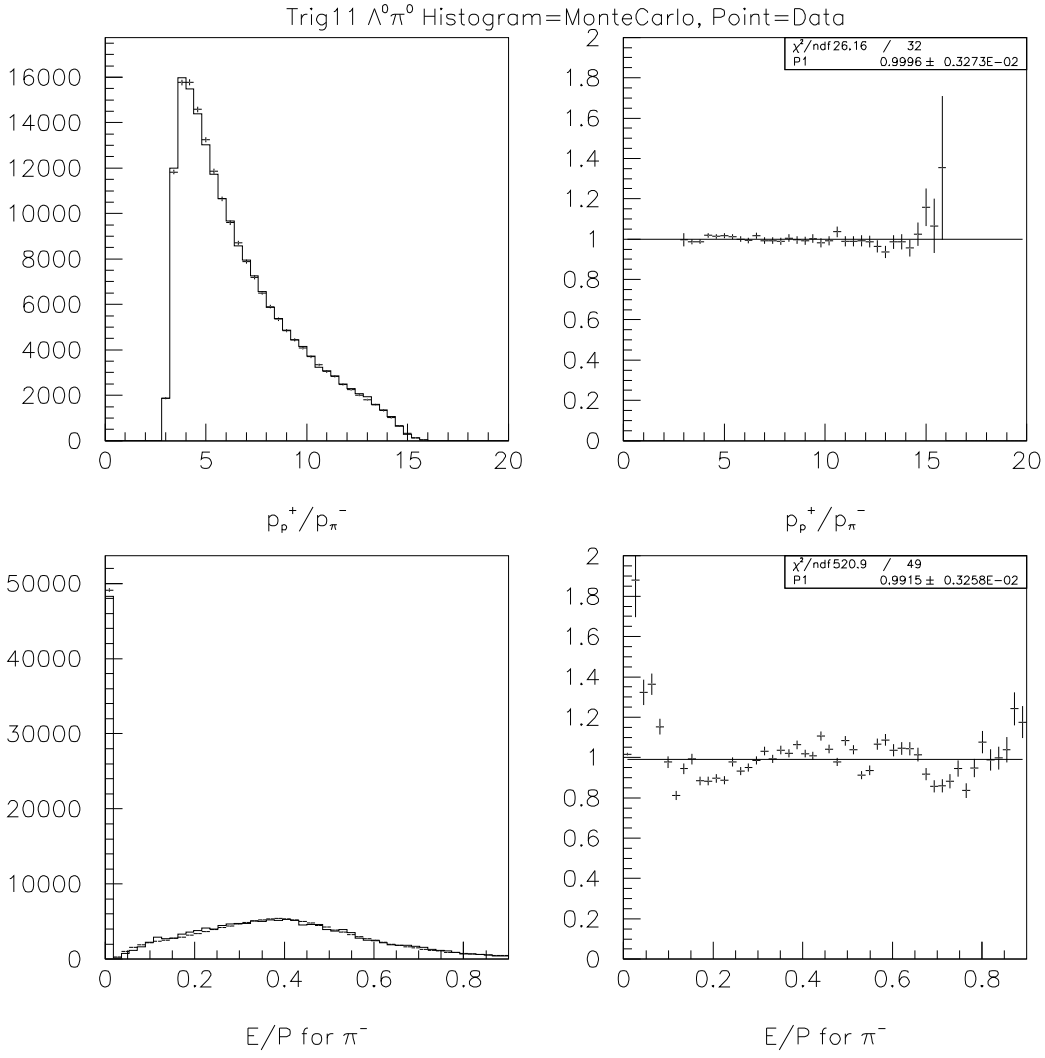

Figure 6.6: Monte Carlo vs. Data for P_p/P_{π^-} and E/P for π^-

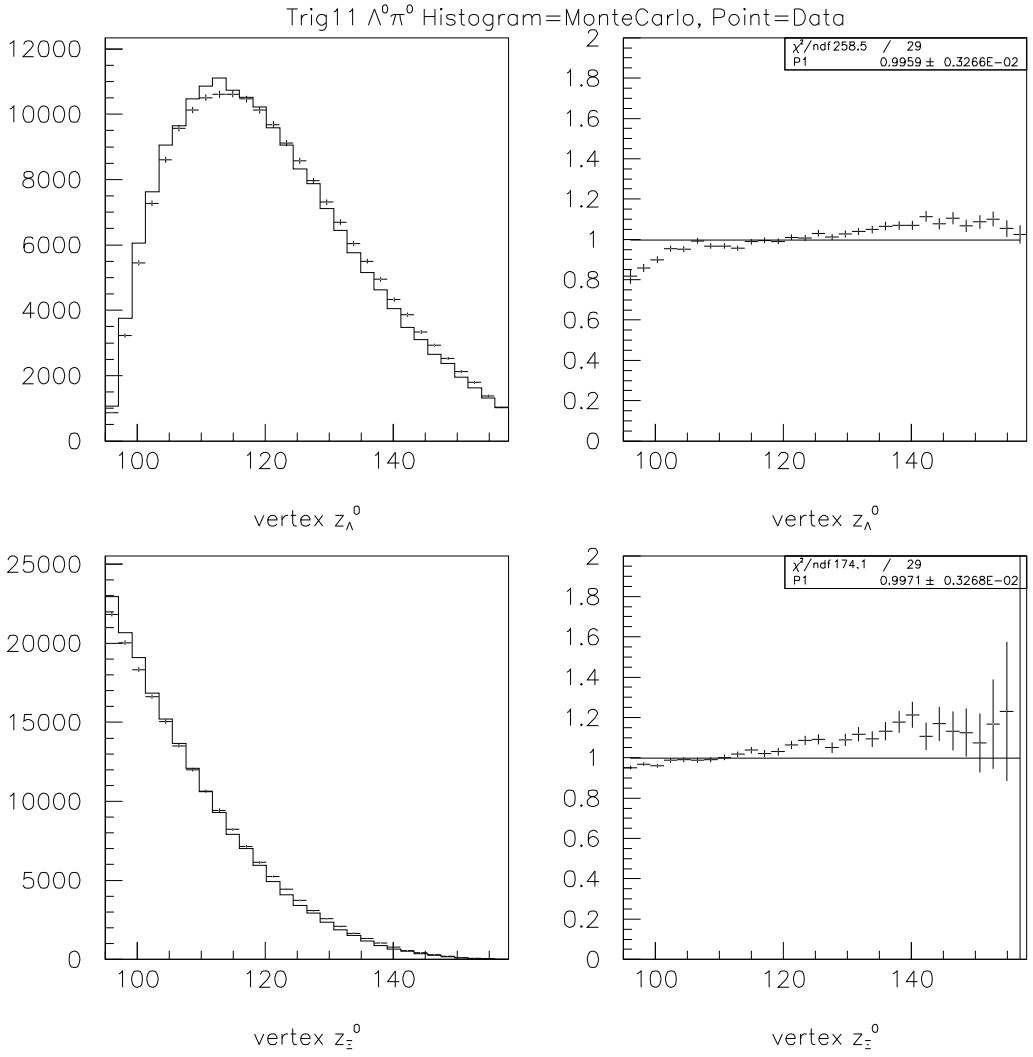

Figure 6.7: Monte Carlo vs. Data for vertex Z_{Λ^0} and Z_{Ξ^0}

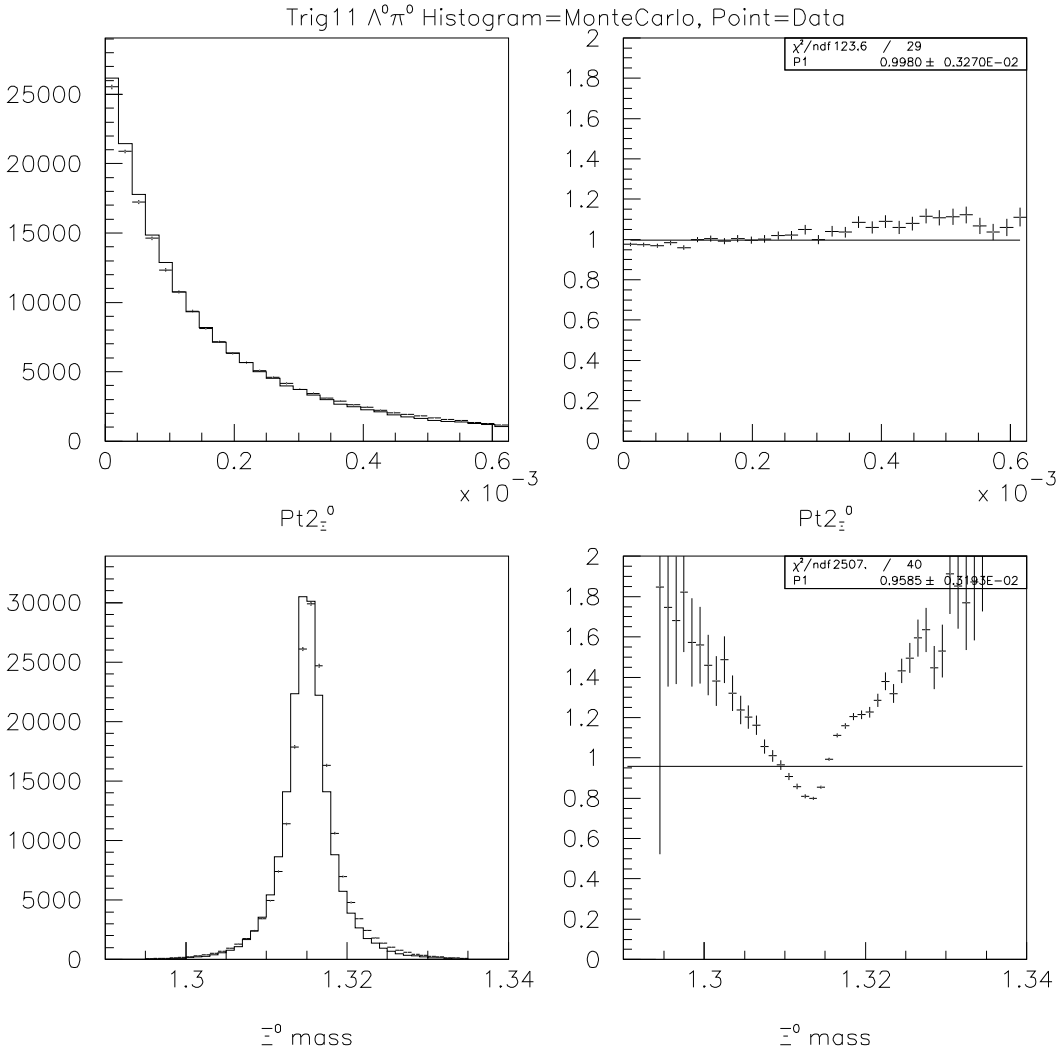

Figure 6.8: Monte Carlo vs. Data for $Pt^2_{\Xi^0}$ and Ξ^0 mass

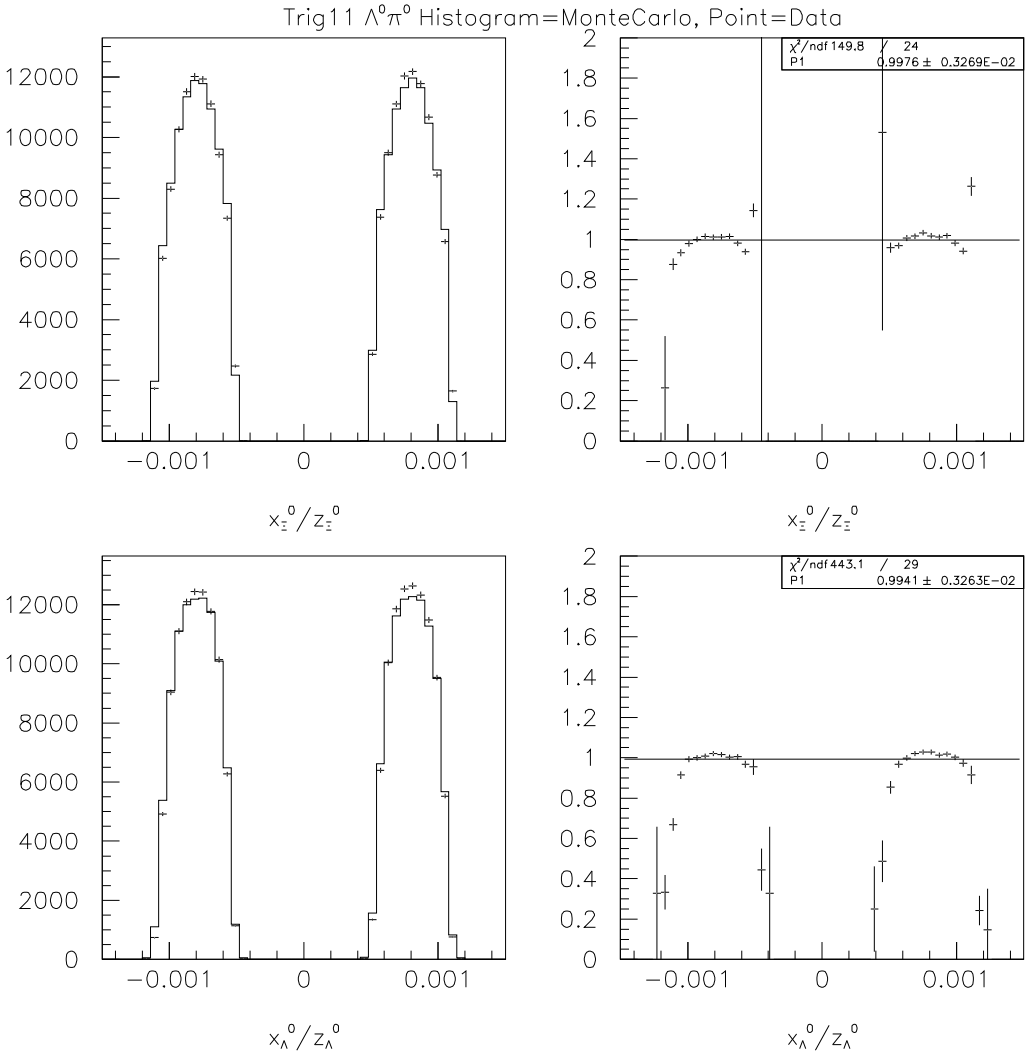

Figure 6.9: Monte Carlo vs. Data for X_{Ξ^0}/Z_{Ξ^0} and $X_{\Lambda^0}/Z_{\Lambda^0}$

6.4 Acceptance and Flux

The normalization mode acceptance has been determined by generating $\Xi^\circ \to \Lambda^\circ\pi^\circ$ decay Monte Carlo events. Different Monte Carlo samples (4,000,000 each) have been generated for trigger 10 and trigger 11.

Using the notation as we discussed in the beginning of this chapter, N'_{mode} for the event number after the analysis cuts and A_{mode} for the cuts acceptance, We can simply write a flux equation for our case.

$$FLUX_{mode} = \frac{N'_{mode}}{Acc_{mode}} \times \frac{1}{BR_{mode}} \times Prescale \tag{6.4}$$

BR_{mode} is the branching ratio. For example, from PDG book, the $\Xi^\circ \to \Lambda^\circ\pi^\circ$ decay mode Branching Ratio is $(99.54\pm0.05)\%$, the $\Lambda^\circ \to p\pi^-$ decay mode Branching Ratio is $(63.9 \pm 0.05)\%$. $Prescale$ is 7 for trigger 11 data, and 1 for trigger 10 data.

6.4.1 Flux calculation from Trigger 11 events

Trigger 11 study:

Trigger 11 Monte Carlo acceptance studies:

	Generated	L2 Accepted	Accepted After Cuts	acceptance(%)
$\Lambda^0\pi^0$	3,999,908	1,132,839	186,601	4.665

Trigger 11 Tape Data studies:

	Accepted Events after Cuts	Acceptance Corrected Events
$\Lambda^0\pi^0$	1,279,299	27,423,344±5,237

We got $1,279,299$ $\Xi^\circ \to \Lambda^\circ\pi^\circ$ trigger 11 tape events after we applied the same cuts as for Monte Carlo events. Based on the acceptance we got from the Monte Carlo simulation which is 4.665%, we got the number, $27,423,344$, which shows us how many the $\Xi^\circ \to \Lambda^\circ\pi^\circ$ events were seen by the KTeV detector subjected to the prescale factor 7. If we multiply this number with prescale factor 7, and divide it with the Branching Ratio of $\Xi^\circ \to \Lambda^\circ\pi^\circ$ (0.9954) and the followed decay $\Lambda^\circ \to p\pi^-$ (0.639), we get the total cascade flux about (301.8 ± 1.3) millions.

6.4.2 Flux calculation from Trigger 10 events

Trigger 10 study:

Trigger 10 Monte Carlo acceptance studies:

	Generated	L2 Accepted	Accepted After Cuts	acceptance(%)
$\Lambda^0\pi^0$	3,999,906	1,106,337	184,170	4.604

Trigger 10 Tape Data studies:

	Accepted Events after Cuts	Acceptance Corrected Events
$\Lambda^0\pi^0$	3,767,458	81,823,779±9,046

In the trigger 10 case, we got $81,823,779$ $\Xi^\circ \to \Lambda^\circ\pi^\circ$ trigger 10 tape events after we applied the same cuts for Monte Carlo events. Based on the acceptance

we got from the Monte Carlo simulation which is 4.604%, we got the number, $81,823,779$, which shows us how many the $\Xi^\circ \to \Lambda^\circ\pi^\circ$ events were seen by the KTeV detector. If we divide it with the Branching Ratio of $\Xi^\circ \to \Lambda^\circ\pi^\circ$ (0.9954) following by $\Lambda^\circ \to p\pi^-$ (0.639), we get the total cascade flux about 128.6 millions.

We can see the there is a big discrepancy between these two $\Xi^\circ \to \Lambda^\circ\pi^\circ$ fluxs (301.8 Million vs 128.6 Million). As we discussed before, the trigger 10 has a Hadron Anti component which will veto a lot of *cascade* decay events if the *pi* in the decay products could be seen by HA.

In our analysis, we have a lot of trigger 11 events. We will use the flux number obtained from trigger 11.

For a discussion of the rough correction I used for the Hadron Anti Veto Effects when doing the branching ratio calculation, please refer sec 8.5.

Chapter 7

The Signal Mode $\Xi^\circ \to \Lambda^\circ\pi^\circ\gamma$ Analysis

When talking about the weak radiative hyperon decays, such as $\Sigma^+ \to p\gamma$, $\Xi^\circ \to \Lambda^\circ\gamma$, phycisists paid attention to its large asymmertry which is contrary to the expectations based on Hara's theorem [2] from the 60's.

Compared to our normalization mode $\Xi^\circ \to \Lambda^\circ\pi^\circ$, the radiative Ξ° decays are more difficult to study. Theoretically, these decays are difficult because of the involvement of weak, electromagnetic, and strong forces.

For the decay mode $\Xi^\circ \to \Lambda^\circ\pi^\circ\gamma$, the γ from the Ξ° has pretty small momentum phase space. It is very easy to be faked by the accidental/background soft γ. Also the estimated Branching Ratio of $\Xi^\circ \to \Lambda^\circ\pi^\circ\gamma$ is very low. This gives more experimental difficulties. Up to now no experiemts have reported a branching fraction measurement for this decay mode.

In this chapter, I will report the search of the weak radiative hyperon decay $\Xi^\circ \to \Lambda^\circ\pi^\circ\gamma$ using the KTeV detector.

7.1 The Reconstruction Methods

Figure 7.1 shows the topology of the signal decay in the KTeV appratus. It is very similar to our normaliztion mode except here we have one more γ in our final state.

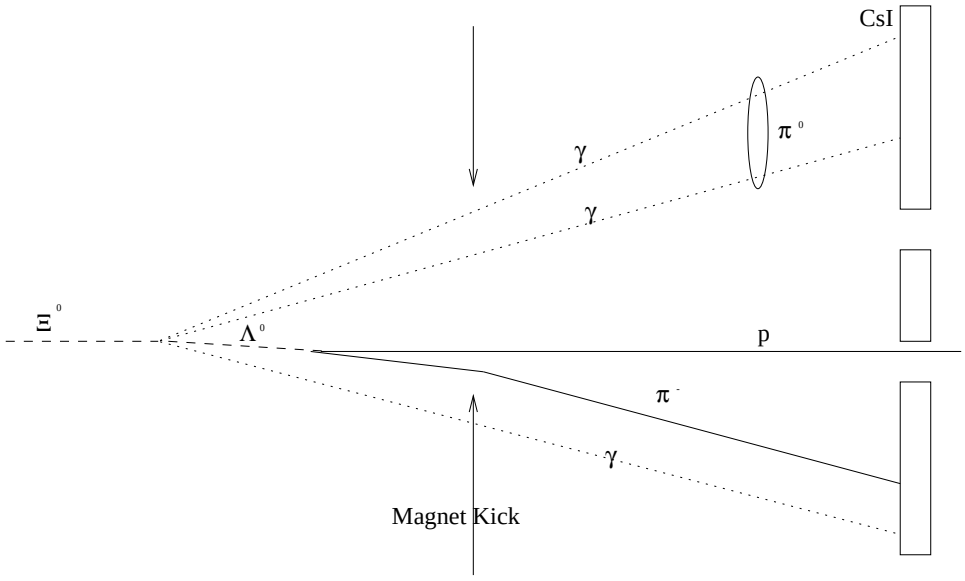

Figure 7.1: The Schemtic Drawing of decay mode $\Xi^\circ \to \Lambda^\circ\pi^\circ\gamma$

As we did for the normalization mode, we can use the π° method to find the Z of the Ξ° decay vertex.

$$z = (\frac{\Delta}{m_{\pi^0}})\sqrt{E_1 E_2} \tag{7.1}$$

The use of the equation is just as we discussed in the normalization mode $\Xi^\circ \to \Lambda^\circ\pi^\circ$ study. At first you assume two γs are the decay products from the π°. Then use the formula to find the Z vertex of the Ξ° decay particle. From the spectrometer system, we know the Λ vertex. Based on the information of the

spectrometer, one can use the Λ momentum and extrapolate it to z coordinate of the Ξ° vertex. The next job is to add another γ to the event and try to get the invariant mass.

Because we have more than two decay γ s, things become more complicated. We know that we have 3 neutral clusters, two of them are the instant decay products of π°, and the other is from the Ξ°. We have to find some ways to guess the correct π° combination.

In our data analysis, we also compared the two ways to reconstruct the events, one is the π° method and the other is CG method. Figure 7.2 shows the comparasion of these two methods. After investigation of these 2 methods, we selected the π° method. This plot is the result of reconstruction methods using Monte Carlo simulated $\Xi^\circ \rightarrow \Lambda^\circ\pi^\circ\gamma$ events. We found that the π° method is dramatically better than CG method in the Ξ° vertex identification. Correct vertex finding is crucial for the event reconstrution.

7.2 Same Cuts for Signal Mode $\Xi^\circ \rightarrow \Lambda^\circ\pi^\circ\gamma$ and Normalizatoin mode

In addition to the L1, L2 and L3 trigger which was applied to the events, we need more cuts to identify the decay mode correctly during data analysis. For easier understanding, we will present my cuts sequentially. At first, we applied the standard cuts to the data (the preselected data with much looser cuts). This produces a much smaller data sample, on which we did the further analysis and applied more cuts.

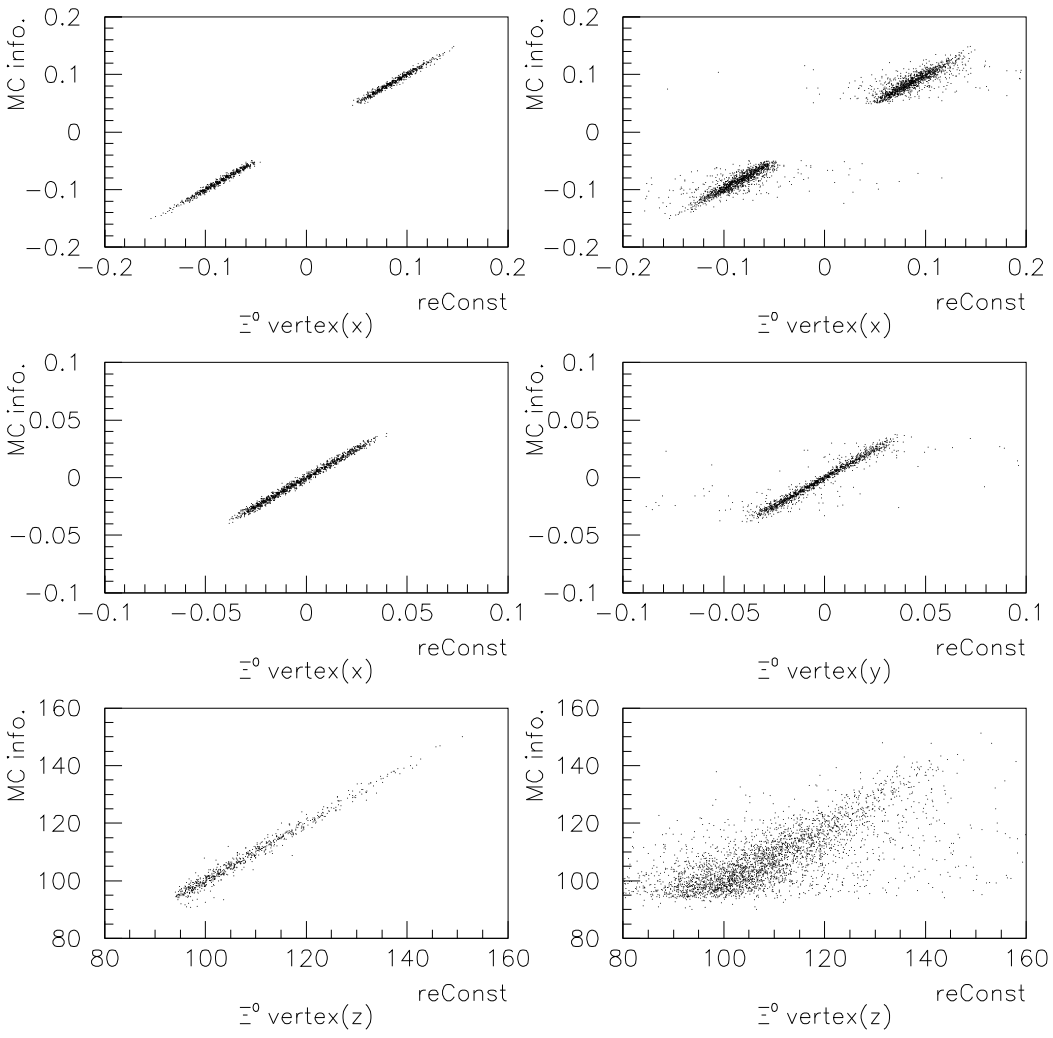

Figure 7.2: *The π° method is better than CG method. In these plots, the horizontal-axes are the recontructed z coordinates of vertices, and the vertical-axes are the corresponding monte carlo information of vertices. The three plots on the left side (using π° method) have better shape than the right three plots (using CG method). The cuts I applied here are the same as the final cuts I applied to 99 Data which I will discuss in the following sections.*

The list below is the part of the cuts for our signal mode.

General Cuts:

- Events only have exactly two tracks, one is a positive charge track, the other is a negative charge track.
- The position of the proton at the CsI face must be inside one of the beam holes by at least 1 cm, and the position of the π^- is outside of the beam holes by at least 1 cm.
- All the γ positions are at least 15 cm away from the π^- position on the CsI
- All the γ positions are at least 15 cm away from each other on the CsI

Vertex Cuts:

- 95.0m $< Z_{\Xi^\circ} <$ 158.0m (vacuum decay region)
- 95.0m $< Z_{\Lambda^\circ} <$ 158.0m, and $Z_{\Lambda^\circ} > Z_{\Xi^\circ}$
- $0.001240 > |x_{\Xi^\circ}/z_{\Xi^\circ}| > 0.000376$
- $0.000430 > |y_{\Xi^\circ}/z_{\Xi^\circ}|$
- $0.001240 > |x_\Lambda/z_\Lambda| > 0.000376$
- $0.000430 > |y_\Lambda/z_\Lambda|$

Momentum and Energy Cuts:

- For two tracks, the momemtum ratio $p(+)/p(-) > 3.0$ to eliminate Kaon decays to 2 π

- For the negative charged track, the energy deposited in CsI and Monmentum ratio is < 0.9 to eliminate electrons.

- $110 Gev/c < |p_p| < 500 Gev/c$ and $5.0 Gev/c < |p_\pi^-| < 100 Gev/c$

- For the neutral clusters, $E_\gamma > 3.0$ GeV, and $\sum E_\gamma s > 18 GeV$

- $Pt_{\Lambda^0} > 24.5 MeV/C$ to eliminate primary Λ°

  This cut is discussed in the chapter of the background study. Please refer the section 8.1 and Figure 8.1.

- $CA_{intime-engy} < 0.5 GeV$ (The intime energy deposited in CAs less than 0.5 GeV).

  Please refer the 1st plot in the Figure 7.3.

- $RC_{intime-engy} < 0.5 GeV$ (The intime energy deposited in RCs less than 0.5 GeV).

  Please refer the 2nd plot in the Figure 7.3.

Invariant Mass Cuts:

- $m_{K_L \to \pi^+\pi^-\pi^0} > 0.55 Gev$

  This cut eliminates the background from the Kaon decay into a $\pi^+\pi^-\pi^\circ$. The event is considered to be a Kaon decay into two charged-track pions. The invariant mass is calculated, and the event is kept if it is greater than 0.55GeV.

- $|m_{p^+\pi^-} - 1.115684| < 0.015 GeV$

Muon System Cut:

- Neither Track is allowed to match a muon counter hit.

7.3 More Cuts: Find π° γ combination

- Number of neutral clusters is exactly 3.

For the signal mode, we have 3 γs, two of them from the π°, so we have to try the 3 possible combinations for the π°'s two gammas. In this analysis we only keep the events with 3 neutral clusters, otherwise more γs would cause many more pair combination problems.

We call the clusters $\gamma 1$, $\gamma 2$, and $\gamma 3$, where $\gamma 1$ has the highest energy followed by $\gamma 2$ and $\gamma 3$. We should try all 3 combinations for π° ($\pi^\circ \rightarrow \gamma 1 + \gamma 2$ etc.), and identify one as the desired combination for the π°.

Here is an example, for the $\pi^\circ(\gamma 1,\gamma 2)$ combination. If the event satisfies these requirements, I will say it is a canditate:

- $(Z_\Lambda - Z_{\Xi^\circ}(12)) > 0$

  Here $Z_{\Xi^\circ}(12)$ is obtained from the assumption that the $\pi^\circ \rightarrow \gamma 1 + \gamma 2$.

- 95.0 m$< Z_{\Xi^\circ}(12) <$ 158.0 m

- $Pt_{\Lambda^\circ\pi^\circ\gamma} < 25 MeV/C$.

  Please Refer the 3rd plot in the Figure 7.3.

- $m_{\Lambda^\circ\pi^\circ} < 1.30$.

  Please Refer the 4th plot in the Figure 7.3.

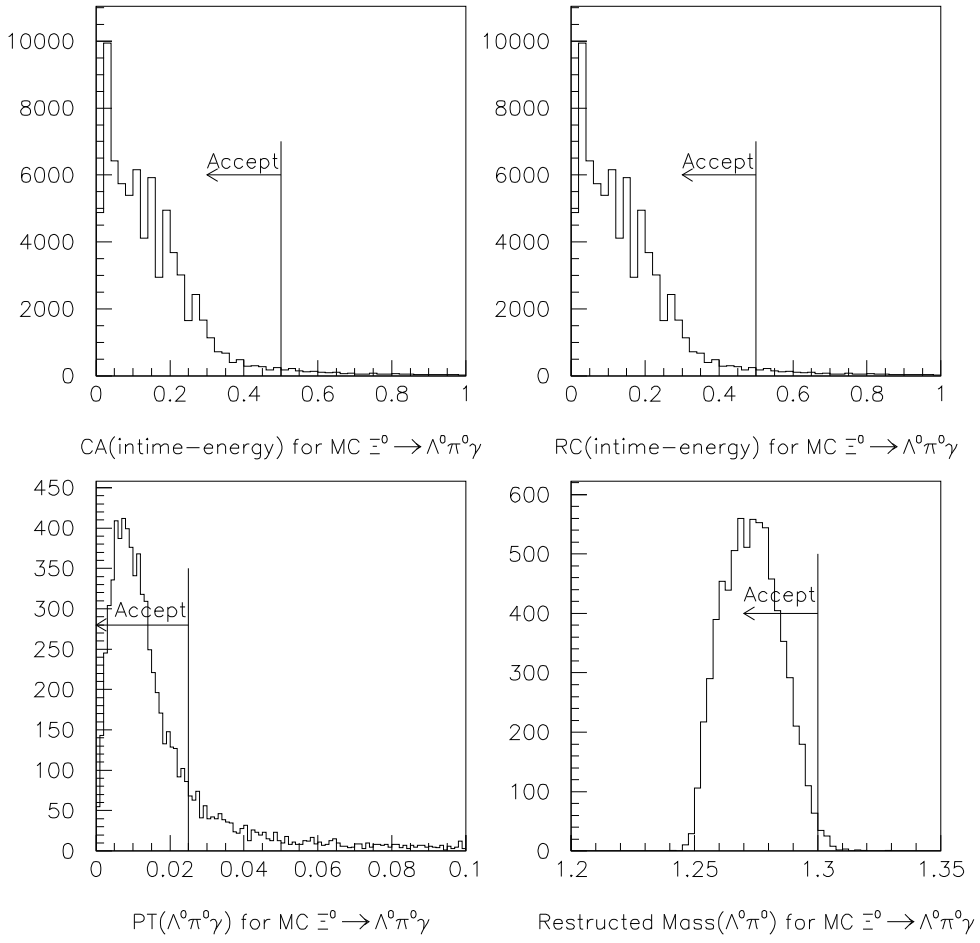

Figure 7.3: CA and RC Intime Energy Cuts; PT($\Lambda^0\pi^0\gamma$) and M($\Lambda^0\pi^0$) cut

In the Figure 7.3, the bottom 2 plots show us the $Pt_{\Lambda^0\pi^0\gamma}$ cut and $m_{\Lambda^0\pi^0}$ cut. These plots are made on the Monte Carlo $\Xi^0 \rightarrow \Lambda^0\pi^0\gamma$ events which were subjected to the cuts we discussed so far. We will keep about 89% of the events after we apply the Pt cut, and will keep about 98% of the events after we apply the mass cut. Here the mass cut is pretty loose. More restrict mass cut on the events are applied later when the events can be seen much more clearly.

After we tried these three possibilities and subjected them to the above cuts, there were several possible γ combination candidates for the *pion*. We got Figure 7.4 using our real tape data. From Figure 7.4 we can see that about 90% of candidates were coming from the combination of the choice $\pi^0(\gamma 1\gamma 2)$ and $\pi^0(\gamma 1\gamma 3)$. For simplicity, we can keep and study only the candidate choice $\pi^0(\gamma 1\gamma 2)$ and $\pi^0(\gamma 1\gamma 3)$, without losing many of the candidates. After this investigation, we apply other cuts to the analysis:

- $\pi^0 \rightarrow (\gamma 1\gamma 2)$ or $\pi^0 \rightarrow (\gamma 1\gamma 3)$
- If the event satisfies both combinations, we will drop this event.
  From Fig. 7.4, this cut will sacrifice about 2% of the total events, but for simplicity in doing analysis we used this one.

7.4 Drift Chambers Cuts

In order to keep our events clean we used additional Drift Chamber hit cuts.

We know that the Drift Chamber reconstruction used some criteria as listed for the intime good hits:

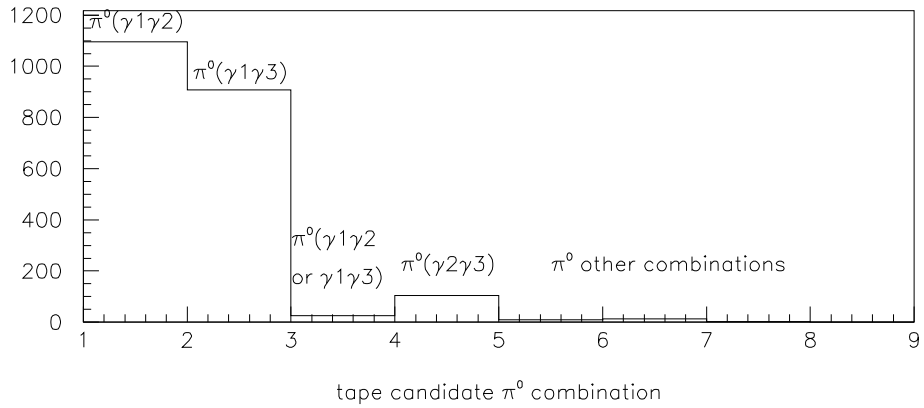

Figure 7.4: The Possible π^0's gamma combinations, from tape data

- The sum of drift distances in the two complementary planes (SOD) equaled 6.35 mm.

- Only the earliest hit in multiple hits was recorded if they were within the same time window of 235 ns.

This increases the probability that we got the correct hit.

In drift chamber selections we should try to avoid any unclean events. For example if there were 3 or more charged particle passing through the up stream DCs and some of them were kicked out after DC1 and DC2 by the magnet, then only 2 charged particles might stay in the decay region and be recorded by DC3 and DC4. Obviously it is possible that this kind of event could fake our event signal requirement of "only two charged tracks".

So we should try to insure the Drift Chambers have no extra hit(s) except the two we wanted, one for proton, and the other for π^-. In our case, we compared

the x and y coordinate of the hits in the DCs with the ones of the proton and π^-. If the differences are larger than 1.5 cm, the we thought it was an extra hit.

The Fig. 7.5 shows us the Up Stream and Down Stream Drift Chambers' Extra Hit for the Data with the cuts so far. We can see most (93%) of the events have pretty clean DC hits, we can set the Extra Hit < 2 for up stream and down stream chambers.

- The Extra Hit of Up Stream and Down Stream < 2

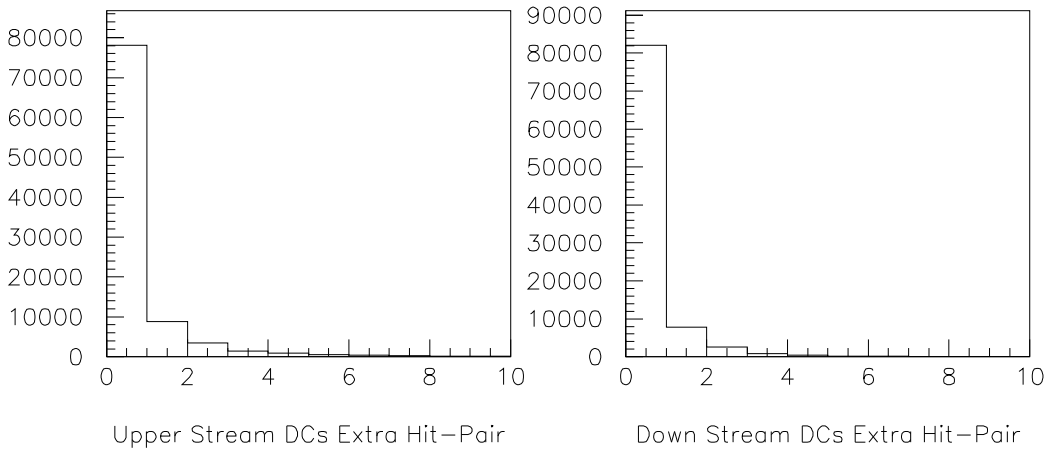

Figure 7.5: The Up Stream and Down Stream DCs' Extra Hit frequency distrubution.

7.5 Rejection of Accidental Photons in the Calorimeter

The time profile of the clusters allowed us to reject some accidental particles. It is a very useful cut to help us to prevent an accidental cluster from faking a radiative

photon. This cut would reduce the background contribution from the decay mode $\Xi^\circ \to \Lambda^\circ\pi^\circ$ with accidental γs and others.

Since the DPMTs measured charge from phototubes every 19 nsec, we could compare the fraction of energy in each 19ns slice as shown in Fig 7.6. Here 19 nsec operation in the DPMT was synchronized with the accelerator RF. The protons incident on the target occupied only the first 2 nsec period in each RF bucket. Thus the secondary particle production was also synchronized with the RF timing. The time profile of the pulse generated by particles for the in-time RF bucket was always the same. After adjusting the DPMT readout phase, roughly 85% of energy deposited by an in-time particle was contained in the first in-time slice from the CsI.

In the KTev analysis code, there are two arrays, ADCSI_EARLY(nclus) and ADCSI_INTIM(nclus). The Units were DPMT counts above the pedestal, summed over all crystals in a cluster. The ADCSI_EARLY(nclus) recorded the ADC counts of one early slice of each cluster, and ADCSI_INTIM(nclus) recorded the ADC counts of the first in-time slice. For good in-time clusters, we should expect very small counts in the ADCSI_EARLY(nclus) and large counts in the ADCSI_INTIM(nclus). Based on this, we can safely discard the events for which the early slice has large counts, or the first in-time slice has small counts.

For the non-accidental photon candidate, the CsI cluster energy deposited in the first in-time RF bucket must be well above pedestal. We studied the ADCSI_INTIM(nclus) in the $\Xi^\circ \to \Lambda^\circ\pi^\circ$ sample. The Fig 7.7 compares the energy-vs-time profiles of the accidental photons and the non-accidental photons. We

reconstructed the normalization mode $\Xi^\circ \rightarrow \Lambda^\circ\pi^\circ$ with the cuts I discussed in the previous chapter. After that, we got the plots of ADCSI_INTIM(γ1, γ2) and ADCSI_INTIM(accidental γ) if the event had an accidental γ.

We can see that there is a very big difference between the accidental γ histogram and the other γs which were decayed from a π°. Based on this study, We apply the below cut to our signal mode, since the hardware response to the intime γ and accidental γ should be same.

- ADCSI_INTIM(intime γs) > 200

We also studied the ADCSI_EARLY variable, but we found out that it was not helpful to move the accidental γ in our case.

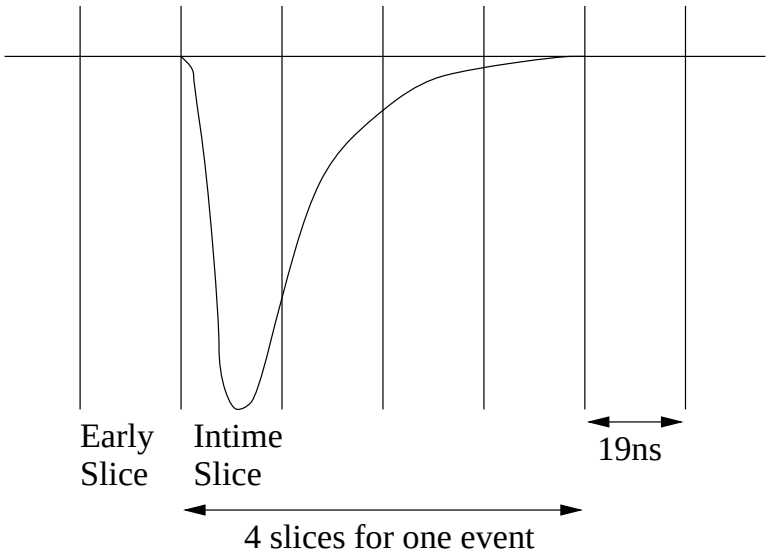

Figure 7.6: Schematic picture of time profile of a pulse at DPMT. The DPMT read out the charge every 19 ns which was synchoronized with accelerator RF.

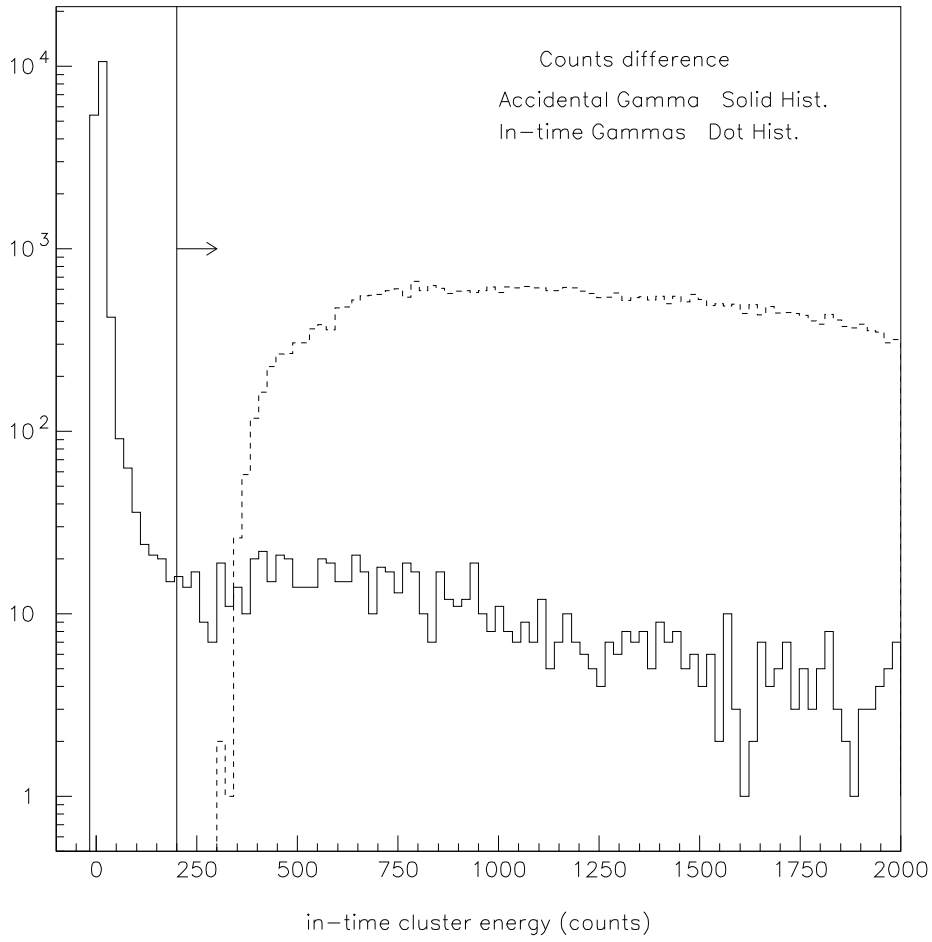

Figure 7.7: The in-time cluster energy distribution in $\Xi^\circ \to \Lambda^\circ\pi^\circ$ data sample. The accidental gamma uses the solid histogram, and the other two γs from π° use the dot histogram.

7.6 $M_{\Lambda^0\pi^\circ}$ Cut Discussion

Fig. 7.8 shows the distribution in $M_{\Lambda^0\pi^\circ}$ for tape data and $\Xi^\circ \to \Lambda^\circ\pi^\circ$ Monte Carlo which are subjected to the cuts so far. The unshaded histogram was made using tape data with previously described cuts so far. The shaded histogram was made using MC events for $\Xi^\circ \to \Lambda^\circ\pi^\circ$ which contains 2 or more neutral clusters. Most data events at this point are background from $\Xi^\circ \to \Lambda^\circ\pi^\circ$. Most of these background events can be removed by applying a cut on $M_{\Lambda^0\pi^\circ}$:

- $M_{\Lambda^0\pi^\circ} < 1.272$

This plot was obtained after applying most of the cuts listed before. I used arbitrary normalization of the MC events used in the plot.

7.7 TRD Cuts

We require there were exactly 2 tracks. One is for the proton with positive charge, and the other is for the pion with negative charge. It is true that there are still possible electron tracks left even though we applied the cut $e/p < 0.9$ before. These electrons could bremslstrahlung to form a 3rd cluster. To enhance the purity of the pions and to get rid of the mis-identified electrons, we use the TRD information [57]. We know that the TRD was designed to discriminate between electrons and pions. Please refer section to 2.4.

For simplicity, we randomly picked one tape (UPH032) for the purpose of the investigation as a sample, and studied the TRDLIKE variable. The TRDLIKE variable [57] means the pion likelihood, i.e., the likelihood of the particle being a

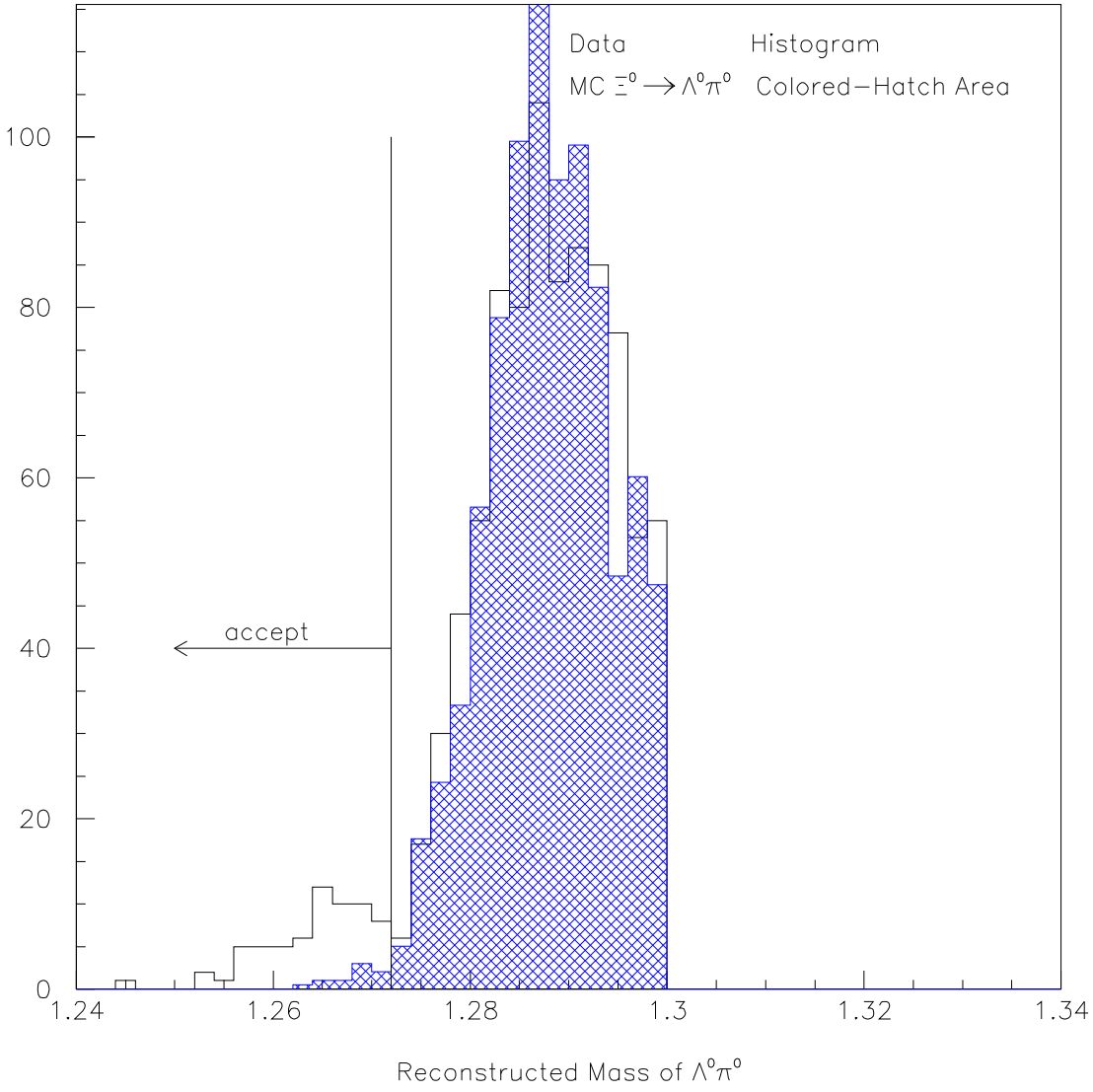

Figure 7.8: This plot of 3-cluster data with all cuts applied except coplanarity, pt cuts, and TRD cuts that are described later. More than 280 million Monte Carlo $\Xi^\circ \rightarrow \Lambda^\circ\pi^\circ$ events were generated for the cross-hatched histogram. We applied the pre-selection cut of $Mass_{\Lambda^0\pi^0} < 1.30$ before plotting, so you can see the sharp edge of the right side.

pion or not. As is the general way for KTeV analysis, we use $0.95 < eop < 1.05$ as electron signature, and $eop < 0.9$ as π^- signature. In our notation, *eop* stands for ratio of energy over momentum for the particle. In the Fig. 7.9, the dash-line is for electron, and the solid histogram is for π^- as identified using eop (the ratio of energy over mementum). We used the TRD cut in our analysis as follows:

- $TRDLIKE < -5$

This TRD cut with eop ratio cut can give a discrimination of over 500:1 for the separation of pion signals and electron signals.

7.8 Coplanarity Cuts Discussion

Figure 7.1 shows the topology of the decay in the KTeV apparatus. We know that the difference for $\Xi^\circ \to \Lambda^\circ\pi^\circ\gamma$ and $\Xi^\circ \to \Lambda^\circ\pi^\circ$ is that our signal mode has an extra γ compared to our normalization mode. For 2-body decay, $\Xi^\circ \to \Lambda^\circ\pi^\circ$, the momentum vectors of the three particles in our lab system must be in the same plane, but it is not necessarily true for our signal mode $\Xi^\circ \to \Lambda^\circ\pi^\circ\gamma$. We try to use this property to distinguish those 2 modes here.

We define the coplanarity like this:

$$coplanarity = \cos(\theta) = \frac{(\vec{p}_{\pi^\circ} \times \vec{p}_{\Xi^\circ}) \cdot (\vec{p}_{\Xi^\circ} \times \vec{p}_{\Lambda^\circ})}{|\vec{p}_{\pi^\circ} \times \vec{p}_{\Xi^\circ}| \cdot |\vec{p}_{\Xi^\circ} \times \vec{p}_{\Lambda^\circ}|} \tag{7.2}$$

There are other choices for the definition of coplanarity. The reason we choose this one is that this one is more sensitive in our analysis. In our signal mode, the extra γ will not carry much momentum because of the limited phase space of this decay mode.

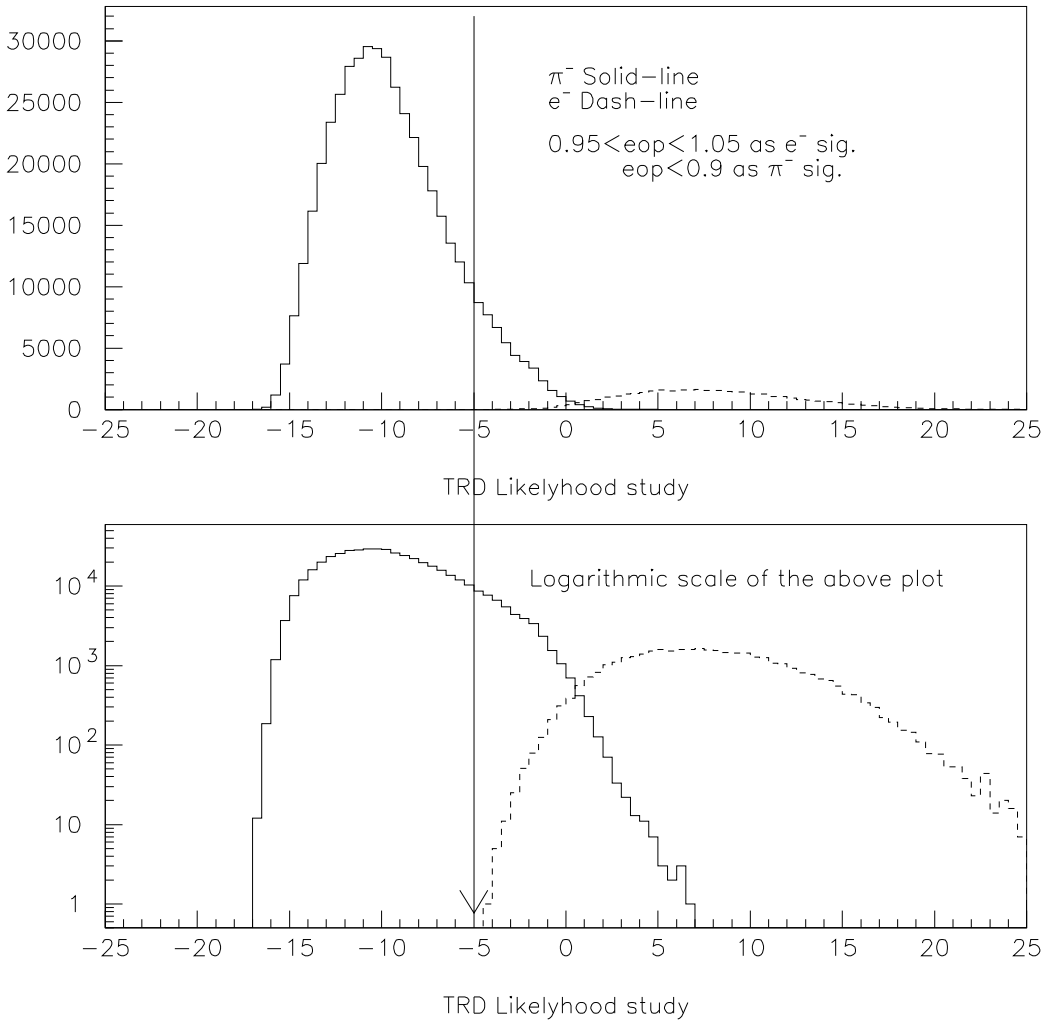

Figure 7.9: The TRD Likelihood study for tape data sample.

Ideally, for $\Xi^\circ \to \Lambda^\circ\pi^\circ$ case, the coplanarity should be equal to 1 (measuring error will produce a secondary peak at -1), but this is not always true for signal mode $\Xi^\circ \to \Lambda^\circ\pi^\circ\gamma$. Figure 7.10 shows the coplanarity of our Monte Carlo events which have been subjected to the cuts discussed so far. For the better visual effects, the plot only shows you part of the $cos\theta$ plot. We can see the difference of these two cases. The shape for our signal mode is much scattered. We put another cut for our data:

- We require for our signal mode events $|coplanarity| < 0.985$.

  We hope we can get rid of 51% of the background of $\Xi^\circ \to \Lambda^\circ\pi^\circ$ with a loss of 21% of our signal events.

7.9 4 Candidate Events

The data used for this study were obtained using trigger 10 and 11 from the 1999-2000 period of data, spanning the runs 14625 to 15548. The data were searched with the standard KTeV analysis package version 5.05 with the seleciton criteria described in the previous sections.

From all these data only 4 events were found that are considered candidates. These events are shown in Table 7.1 which gives us the RunNum, EventNum, the reconstructed invariant mass, the transverse momentum, and trigger information. All 4 events were shown in Fig [7.12 - 7.15] using the standard KTeV event display program with the name of kdisp. The Fig. 7.11 shows us a plot of the reconstructed Ξ° mass versus p_t of the reconstructed Ξ°.

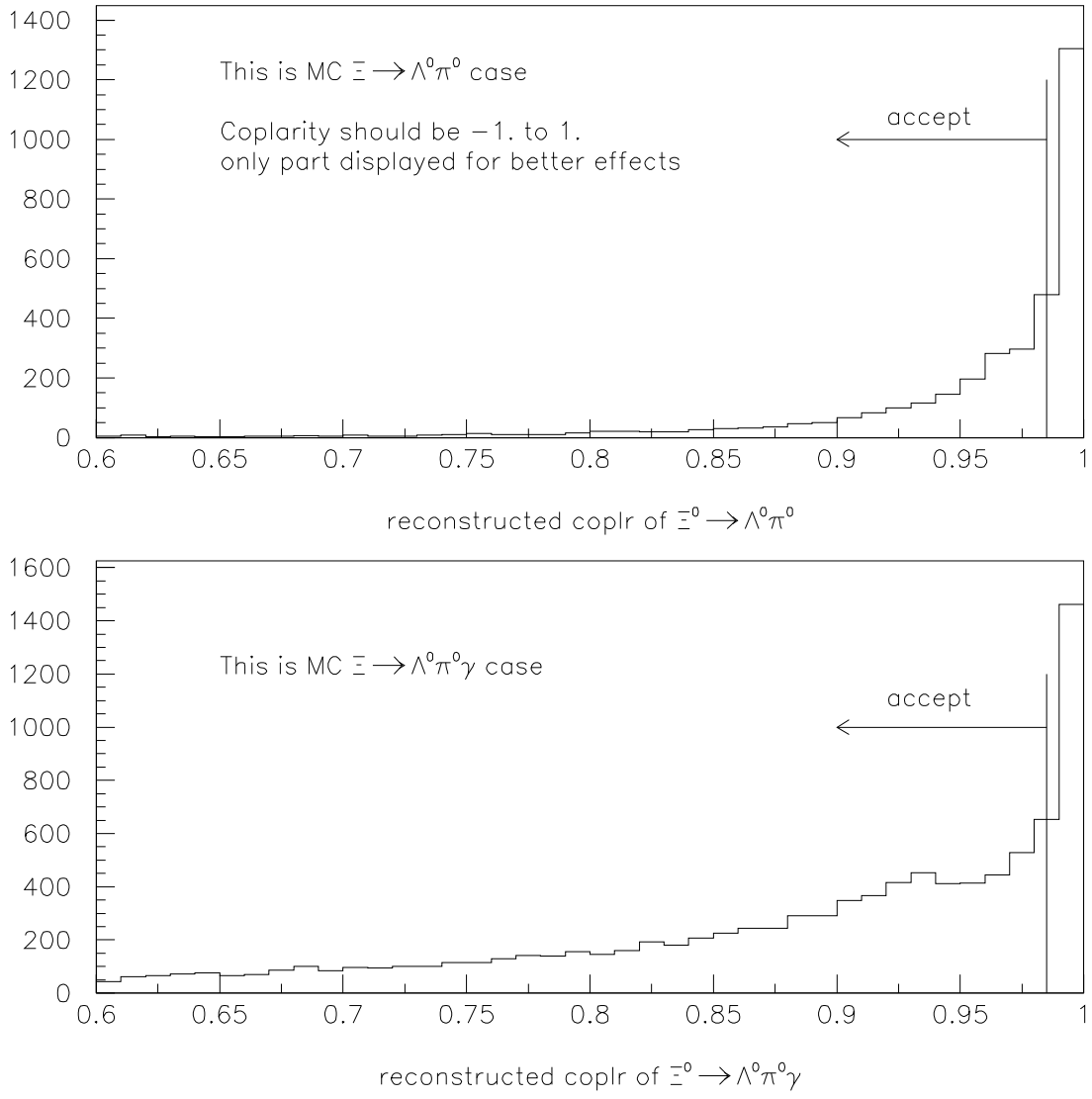

Figure 7.10: The Coplanarity for reconstructed $\Xi^\circ \rightarrow \Lambda^\circ\pi^\circ$ and $\Xi^\circ \rightarrow \Lambda^\circ\pi^\circ\gamma$ Monte Carlo Events

A Monte-Carlo study of this signal mode was performed with version 5.05 of the KTeV Monte-Carlo simulation package and it is shown in the two bottom plots in Fig. 7.11.

In the Fig. 7.11, the top plot shows us the 4 candidate events' mass peak, and the bottom plot shows us the Monte Carlo events which are subject to the same cuts which were applied for the data.

Table 7.1: The detailed information of these 4 candidate events.

RunNo.	EventNum	InvMass	Coplar	Pt(Mev)	$P_{\pi^-}(GeV)$	Trig10	Trig11
14745	56283695	1.315457	0.9287	15.64	25.1	-1	0
14853	12796658	1.313265	0.9297	4.67	48.4	-1	0
14986	5783654	1.315632	0.9715	19.35	24.6	-1	-1
15310	80192848	1.316296	0.6923	8.09	36.9	-1	0

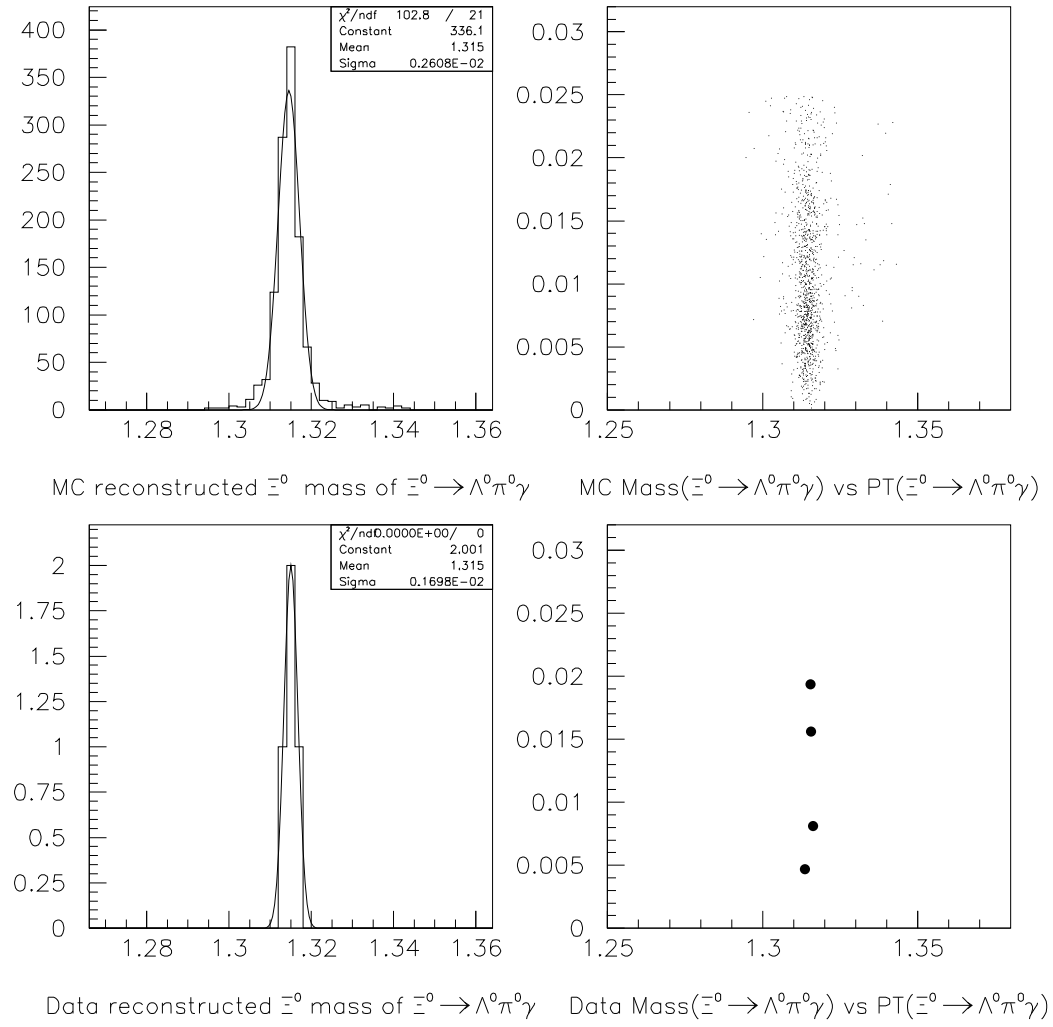

Figure 7.11: The bottom two plots are the Data reconstructed mass peak and it mass vs. momentum kick (PT); the above two plots are the corresponding ones for Monte Carlo.

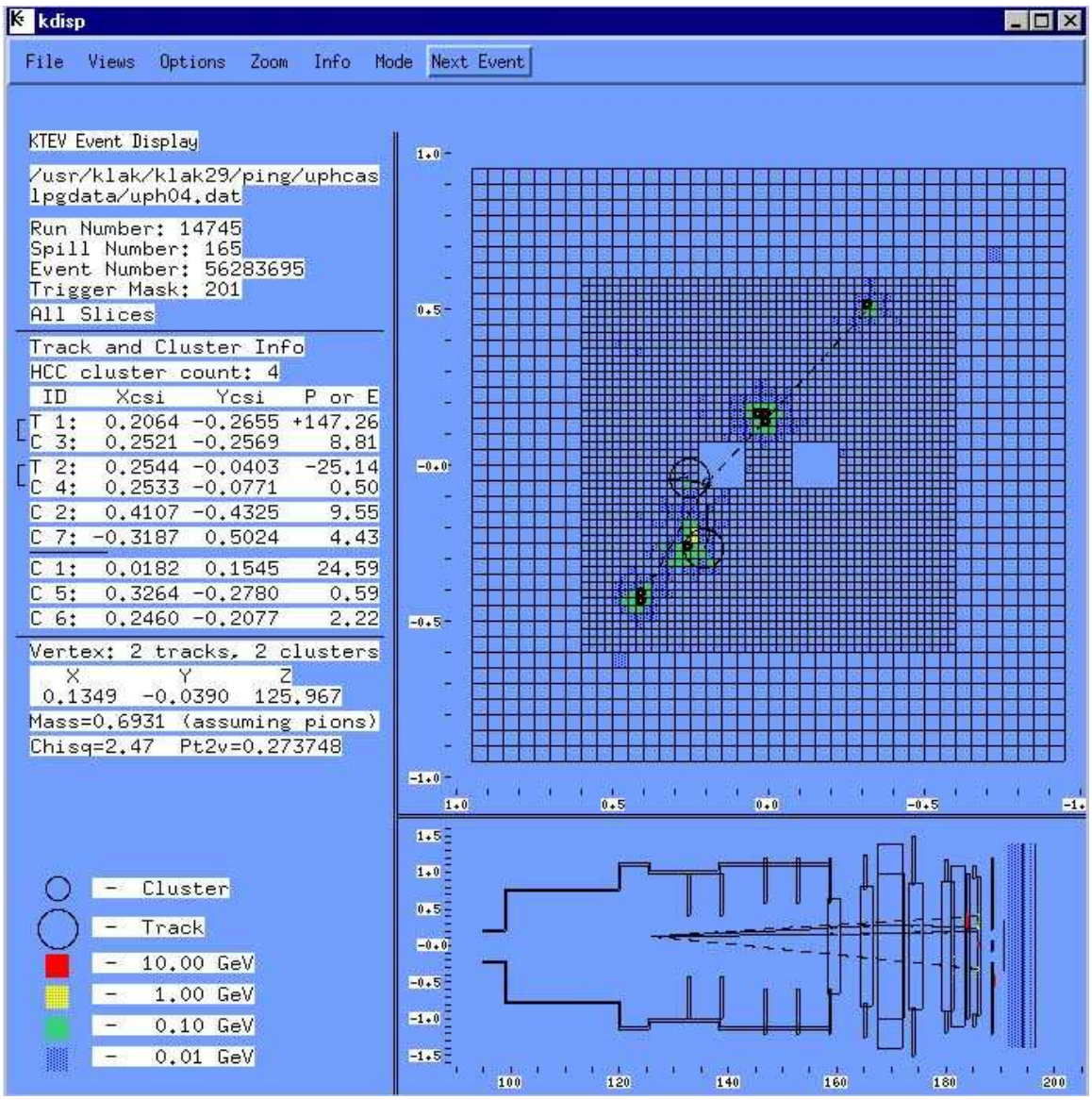

Figure 7.12: The KTeV event display for a typical $\Xi^\circ \to \Lambda^\circ \pi^\circ \gamma$ event. This event is very clean and is one of our 4 candidate events

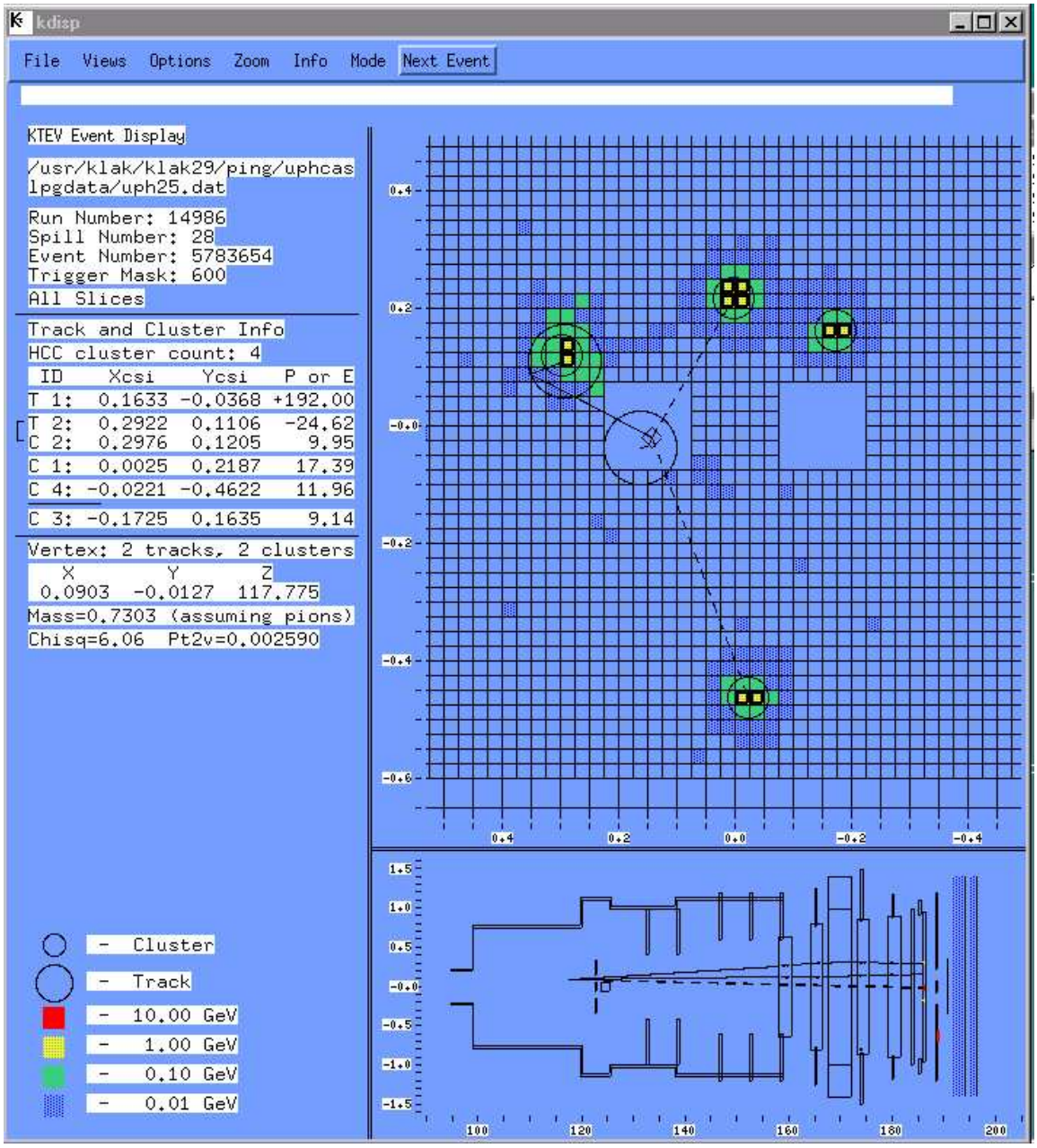

Figure 7.13: The KTeV event display for a typical $\Xi^\circ \to \Lambda^\circ \pi^\circ \gamma$ event. This event is very clean and is one of our 4 candidate events

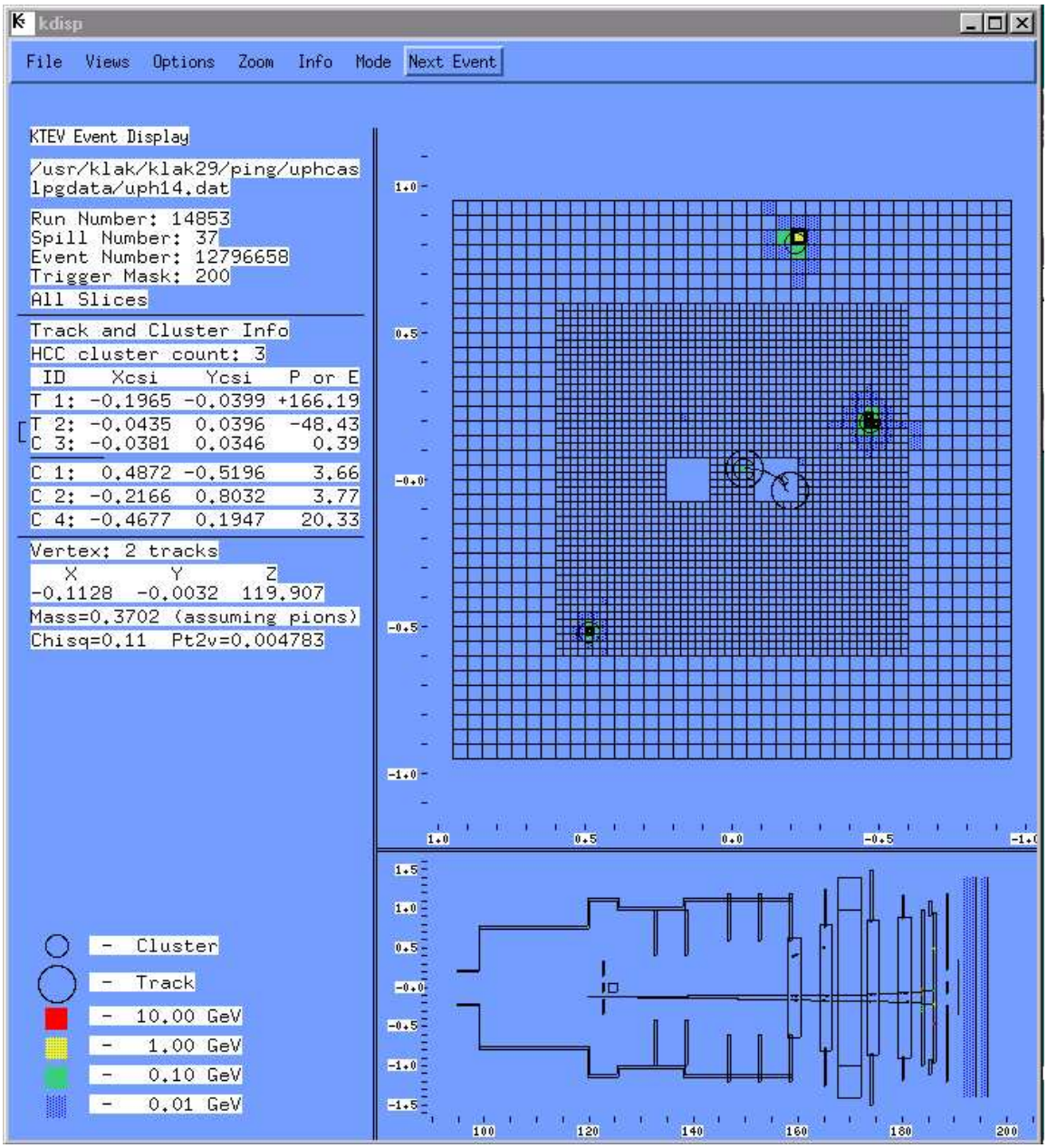

Figure 7.14: The KTeV event display for a typical $\Xi^0 \to \Lambda^0\pi^0\gamma$ event. This event is very clean and is one of our 4 candidate events

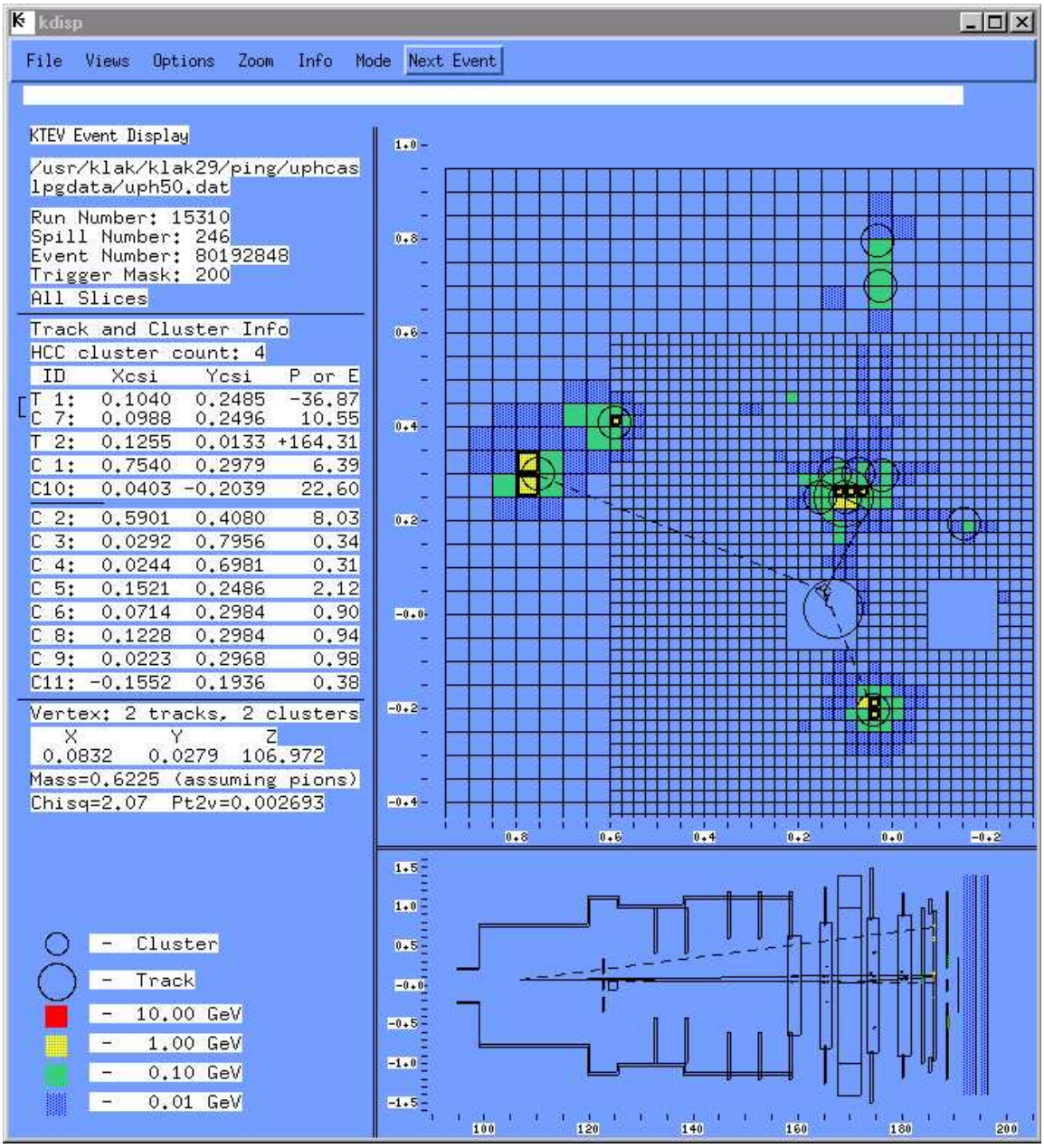

Figure 7.15: The KTeV event display for a typical $\Xi^0 \to \Lambda^0\pi^0\gamma$ event. This event is very clean and is one of our 4 candidate events

Chapter 8

Background and Hadron Anti Correction

Most background decays were studied by Monte Carlo Simulation which includes accidental gammas. They were generated using KTeV Monte Carlo version 5.05 and at a level higher than 10 times the statistics needed for their actual background level contribution.

8.1 Lambda Background

We studied the Primary Lambda decay $\Lambda^\circ \to p\pi^-$. We know that the KTeV target also generated a lot of primary Λs when the proton beams hit the BeO target. We consider this mode also as one of our main backgrounds here. We study the reconstructed square of transverse momentum of the Λ, and if $Pt[\Lambda^0] < 0.0245$, then we will not keep these events. With high possibility, this is a primaryΛ decay event. In the Figure 8.1's right plot which is for Monte Carlo sample of the signal mode, with this cut we can keep 93% of our signal mode events intact, and get rid of 92% of primary lambda decay $\Lambda^\circ \to p\pi^-$ events in the left plot. These two plots are made in the same cut stage, i.e., after the Level 1 , Level 2 and Level 3 trigger and my pre-selection cuts. Combined with other cuts which are used in our

analysis such as $Pt[\Xi^0]$, we didn't find any of these background events. The plot was made from the Monte Carlo simulation of $\Lambda^\circ \to p\pi^-$ and our signal mode.

- The cut here: $Pt[\Lambda^\circ] > 0.0245$.

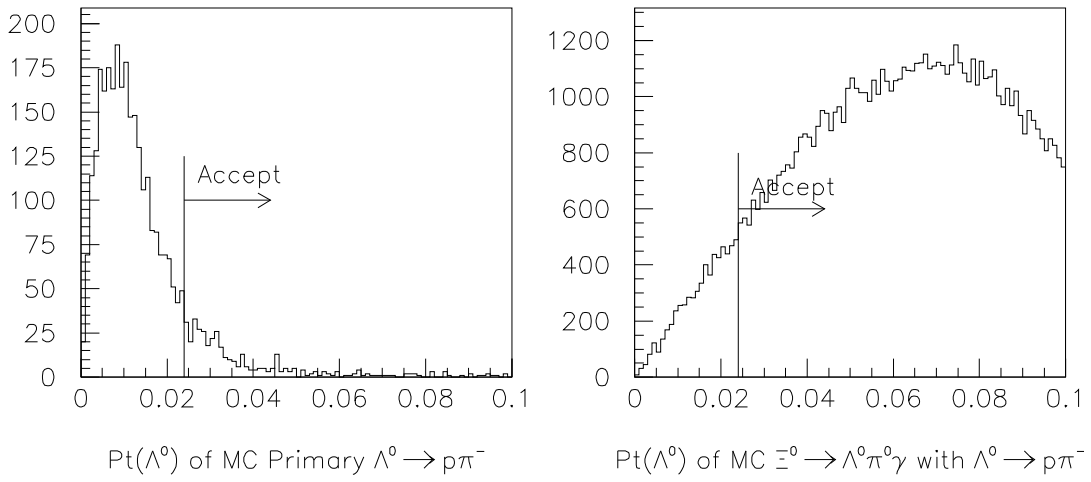

Figure 8.1: The cut for primary Λ decay.

8.2 Cascade Backgrounds

8.2.1 $\Xi^\circ \to \Lambda^\circ\pi^\circ$ followed by Radiative Lambda decay $\Lambda^\circ \to p\pi^-\gamma$

Because it has the same final decay products, the decay mode $\Xi^\circ \to \Lambda^\circ\pi^\circ$ with Radiative Lambda decay $\Lambda^\circ \to p\pi^-\gamma$ is considered as one of our main backgrounds. Its BR of $\Xi^\circ \to \Lambda^\circ\pi^\circ$ with $\Lambda^\circ \to p\pi^-\gamma$ is about $(99.522\% \times 8.4 \times 10^{-4} \approx 8.36 \times 10^{-4})$.

Based on the paper by S. Barshay and R. E. Behrends [58], we wrote our Monte Carlo generator for radiative lambda decay and incorporated it into the

KTeV Monte Carlo.

We generated 4M events, which is about 16 times more than the number of these events in these runs based on the $301.8M$ Ξ° flux we determined earlier. This decay mode has the same final decay products as our signal mode, and we deem it as a main background for our study. This background is easy to remove by some reconstructed mass cuts. We compared the mass$[p\pi^-]$ and mass$[p\pi^-\gamma]$ for the signal Monte Carlo sample and this background Monte Carlo sample.

From Figure 8.2, you can see the histogram's difference. The top two plots are for the mass$[p\pi^-]$ and mass$[p\pi^-\gamma]$ for our signal mode Monte Carlo sample. The bottom two plots are for the mass$[p\pi^-]$ and mass$[p\pi^-\gamma]$ for this background mode. As we stated in the section 7.2, we used the cut:

- $|m_{p^+\pi^-} - 1.115684| < 0.015GeV$

Using this cut, we can cut about 47% of these background events out. Also here we needed to use a new cut:

- $m_{p\pi^-\gamma} > 1.14$.

Using the mass cut $m_{p\pi^-\gamma} > 1.14$ will get rid of 100% of the background events, and we lose no signal in this way.

8.2.2 $\Xi^\circ \to \Lambda^\circ\pi^\circ$ followed by $\Lambda^\circ \to p\pi^-$ plus accidental one γ

This decay mode is our normalization mode. As we stated before, the difference of the normalization mode and signal mode is only the γ, so the tail of the normalization mode due to large measuring error makes us uncomfortable. Background from the tail of $\Xi^\circ \to \Lambda^\circ\pi^\circ$ followed by $\Lambda^\circ \to p\pi^-$ and a background γ might fake

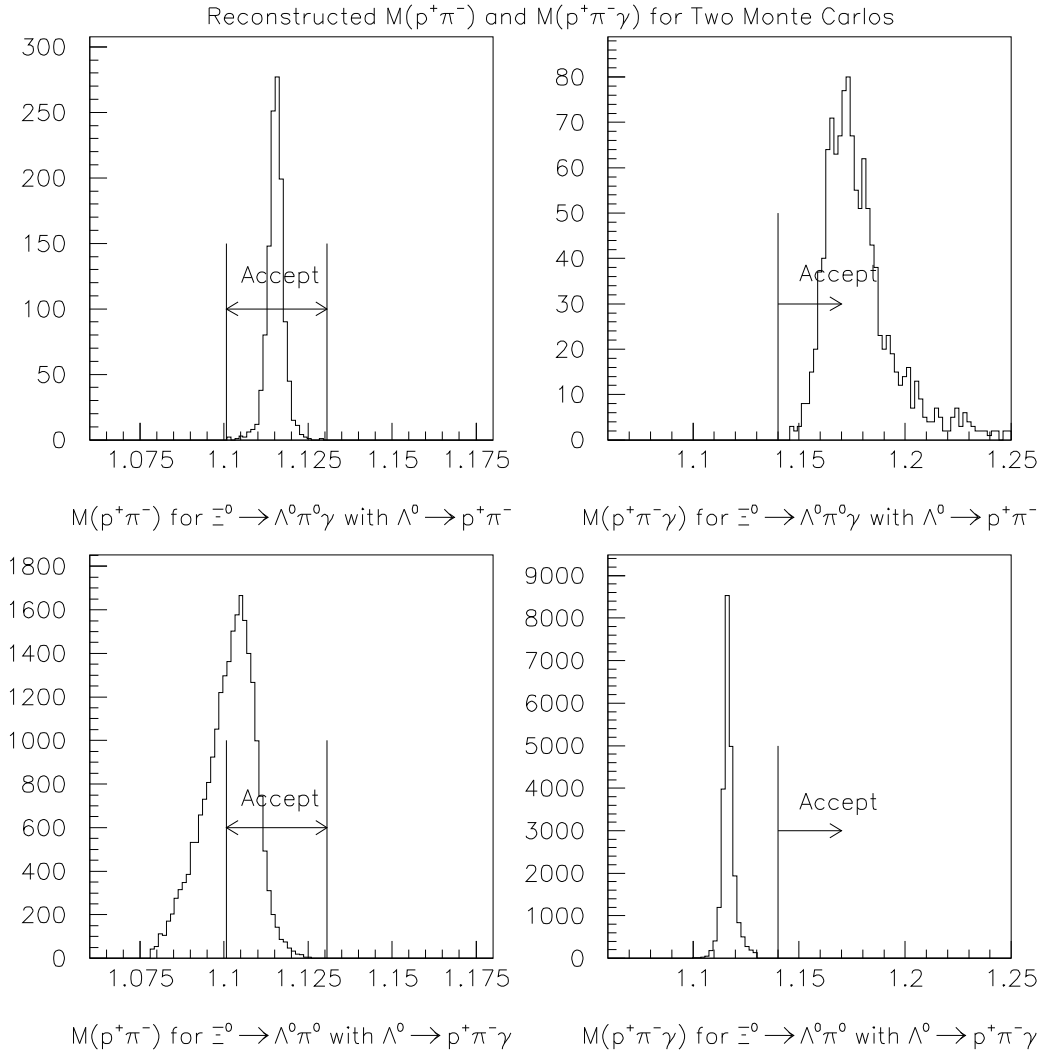

Figure 8.2: The top two plots are for the mass[$p\pi^-$] and mass[$p\pi^-\gamma$] for our signal mode MC; the bottom two plots are for the mass[$p\pi^-$] and mass[$p\pi^-\gamma$] for this background mode MC. The arrows in the plots are the cuts to accept or cut the events.

our signal mode. In order to get rid of this background, we used these cuts:

- If $|m_{\Lambda^\circ\pi^\circ} - 1.3145| < 0.09$ and $Pt_{\Lambda^\circ\pi^\circ} < 0.001$ in any one of the three combinations of π°, we will assume these events could be $\Xi^\circ \to \Lambda^\circ\pi^\circ$. If they satisfy these cuts, we will drop the event. The reason why we choose 0.09GeV is that this is within 3σ of the reconstructed invariant mass of normalization mode using real data.

- Also we used the coplanarity cut before to get rid of this background. It was discussed in this chapter, in section 7.8.

8.2.3 $\Xi^\circ \to \Lambda^\circ\pi^\circ$ followed by $\Lambda^\circ \to p\mu^-\nu_\mu$ plus accidental one γ

The BR of $\Xi^\circ \to \Lambda^\circ\pi^\circ$ with $\Lambda^\circ \to p\mu^-\nu_\mu$ is about 1.56×10^{-4}. We generated 1 million events. This number is more than 20 times bigger than the expected number. Since this decay mode has a μ^- in the final state, we know that it is a very penetrating particle. Usually it will hit the muon counters which were located at the most down-stream part of the KTeV detector. We applied the cut to require that "Neither Track is allowed to match the muon counter hit". This cut is very useful. For those MC events generated, after I apply all cuts discussed previously, there is no background from these events left.

8.2.4 $\Xi^\circ \to \Sigma^\circ\gamma$ followed by $\Sigma^\circ \to \Lambda^\circ\gamma$ and $\Lambda^\circ \to p\pi^-$ plus an accidental γ

This configuration also gives the same final particles as our signal mode. The BR of this mode is: $3.33 \times 10^{-3} \times 100\% \times 63.9\% = 2.13 \times 10^{-3}$. We study this decay using the CG method to find the vertex, because here we cannot use the π° method to find the vertex. In this background mode, we use the invariant mass of Σ to cut the events out. Also we know that other cuts like coplanarity cuts, and vertex cuts in our signal mode analysis (we require 2 γs to give the π° invariant mass and get the vertex) also contribute to supress this background. We generated 500K MC events of this kind. We applied our cuts to that MC data, and no background remained in this analysis.

8.3 Kaon Backgrounds

8.3.1 $K_L \to \pi^+\pi^-\pi^\circ$

The long lived kaon decaying into $K_L \to \pi^+\pi^-\pi^\circ$ is one of the most relevant backgrounds for our analysis, mainly because the number of kaons in the experiment is huge (about 500 time the number of Ξ^o). To generate the number of events using Monte Carlo for this decay would requre too much computing time and capacity.

This is one of the dominant K_L decay modes with a branching ratio (BR) of 12.56% and could be a background when the positive pion goes down the beam hole and is mistakenly called a proton. This background can easily be indentified and removed. The cuts $m_{K_L \to \pi^+\pi^-\pi^\circ} > 0.55 Gev$, $|m_{p\pi^-} - 1.115684| < 0.015 GeV$ to keep the events, the timing cut to reject the accidental γs (see the section 7.5),

and the charged vertex transverse mometum cut are effective for removing these events.

To measure this background level of charge symmetric $K_L \to \pi^+\pi^-\pi^\circ$ decays, it is not feasible to use the Monte Carlo to generate the number of events for this decay. The solution of this problem was to use data itself to simulate $K_L \to \pi^+\pi^-\pi^\circ$ background. We employed a wrong-sign charge analysis to measure the background level. The wrong-sign analysis of $K_L \to \pi^+\pi^-\pi^\circ$ used the symmetry between π^+ and π^-. It consisted of selecting events having a negative high-monemtum particle in the beam satisfying the proton selection criteria and a positive low-momentum particle in the calorimeter satisfiying the π^- identification criteria. This technique took advantage of the symmetry between π^+ and π^- in $K_L \to \pi^+\pi^-\pi^\circ$ decay and of the suppression of anti-hyperon production at the KTeV facility; the $\overline{\Xi^o}$ production rate being an order of magnitude smaller than the Ξ^o rate [59].

This method is perfect to investigate the contribution of $K_L \to \pi^+\pi^-\pi^\circ$ background and the corresponding anti-hyperon decay. There were no background events seens from the wrong sign charge analysis after applying all selection criteria.

8.4 Backgrounds After Selection Criteria

Backgrounds from Kaon and hyperon decays are studied for possibly faking the $\Xi^\circ \to \Lambda^\circ\pi^\circ\gamma$.

From the study, the main background is from our normalization mode ($\Xi^\circ \to \Lambda^\circ\pi^\circ$ with $\Lambda^\circ \to p\pi^-$). We generated 280M events (about 30M/tape), and there were

no background events of this kind left in our analysis. Also for all the other modes which we listed previously, there were no background events left either after they were subjected to all the cuts.

8.5 Hadron-Anti correction for the candidate events

First, we pointed out the Hadron-Anti problem when we did the normalizaion mode $\Xi^\circ \to \Lambda^\circ\pi^\circ$ analysis. We know that the bank of scintillator hodoscopes, called "Hadron Anti" (HA), was used to reduce the trigger rate by vetoing the events producing charged pions. In particular, in our normalization mode and signal mode, the HA frequently vetoed on the pions from the decay of lambda, $\Lambda^\circ \to p\pi^-$. In our data, Trigger 10 included the HA veto (Trigger 11 did not). It means that a lot of Trigger 10 events were vetoed out, and in the current MC version the HA effects were not implemented. As we have noticed, all the 4 candidate events are trigger 10 events, we need to make some correction when we do the branching ratio caculation. In this section, we present the methodology for estimating the HA effect on the trigger 10 data.

Since the Hadron-Anti was not part of Trigger 11, by using Trigger 11 $\Xi^\circ \to \Lambda^\circ\pi^\circ$ data we can study the correction of HA efficiency versus the π^- momentum. Assume that N(11) is the total number of $\Xi^\circ \to \Lambda^\circ\pi^\circ$ events with Trigger 11 latch ON (Trigger 10 could be either ON or OFF), and N(11•10) is the number of events with Trigger 10 and 11 on. From section 3.4, we can see that the major difference between these two triggers is the Hadron-Anti requirement. If trigger 11 fires and trigger 10 doesn't fire, it is only because of the veto from the Hadron Anti.

From the studies of the cascade flux in section 6.4, we have a table for $\Xi^\circ \rightarrow \Lambda^\circ\pi^\circ$ events that were tagged by Trigger 11.

Trigger 11 Tape Data studies:

	$TotalTrig11$	$Trig11 \bullet Trig10$	$Trig11 \bullet \overline{Trig10}$
$\Lambda^0\pi^0$	1,279,299	688,311	590,988

The Figure 8.3 shows us the π^- momentum distrubution of the Trigger 11 data subject to the HA's effects. The hollow histogram is for *all* $Trigger11$ data, and the hatched histogram is for $Trig11 \bullet Trig10$ (Both Trigger 11 and 10 are ON) data. From this Figure, we can clearly see the HA effects on the $\Xi^\circ \rightarrow \Lambda^\circ\pi^\circ$'s Trigger 11 data. We can conclude that the same effects must exist in the Trigger 10 data, since both Trigger 11 and Trigger 10 data that we are studying have the π^- as a decay particle.

We have constructed the table 8.1 for each bin in the Figure 8.3. From the column of efficiency, we can see that with the π^- momentum increasing, more events will be vetoed out by HA. It is true since higher momentum π^- would more easily pass through the Calorimeter and hit the HA scintillator and leave a sufficiently large veto signal.

Based on the efficiency which was calculated in the above table, we can reasonably make a correction for our 4 candidate events using the HA veto effects for the Trigger 10.

The Run Number, Momentum and other information about these four events are shown in table 8.2.

Table 8.1: The HA effects for $\Xi^\circ \rightarrow \Lambda^\circ\pi^\circ$ Trigger 11 data.

Momentum Range (GeV)	$TotalTrig11$	$Trig11 \bullet Trig10$	Efficiency
(0,5]	1	1	100.0%
(5,10]	2909	2455	84.4%
(10,15]	54673	43052	78.7%
(15,20]	134773	96169	71.4%
(20,25]	170587	109200	64.0%
(25,30]	177331	101604	57.3%
(30,35]	172390	89234	51.8%
(35,40]	157273	75254	47.8%
(40,45]	133625	59767	44.7%
(45,50]	103094	44215	42.9%
(50,55]	71912	29335	40.8%
(55,60]	45585	17902	39.3%
(60,65]	26525	10132	38.2%
(65,70]	14539	5256	36.1%
(70,75]	7489	2586	34.5%
(75,80]	3604	1213	33.6%
(80,85]	1713	559	32.6%
(85,90]	748	225	30.1%
(90,95]	329	91	27.7%
(95,100]	130	40	30.8%

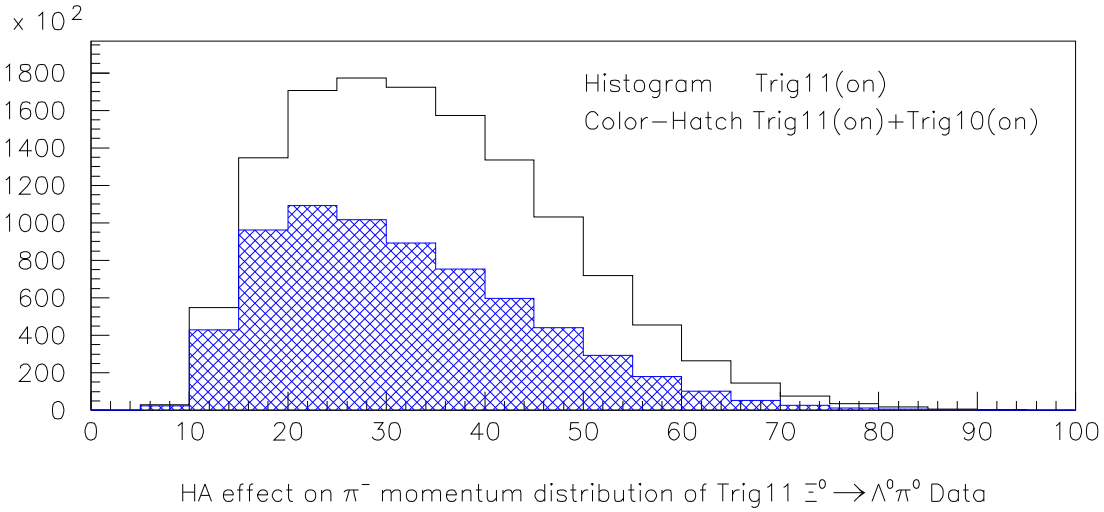

Figure 8.3: HA effects on π^- momentum distrubution for the Trigger 11 data

Table 8.2: The detailed information for these 4 candidate events.

RunNo.	EventNum	InvMass	Pt(Mev)	$P_{\pi^-}(GeV)$	Trig10	Trig11
14745	56283695	1.315457	15.64	25.1	-1	0
14853	12796658	1.313265	4.67	48.4	-1	0
14986	5783654	1.315632	19.35	24.6	-1	-1
15310	80192848	1.316296	8.09	36.9	-1	0

Also from table 8.1, we have used the HA effects for the corresponding π^- momentum range for the 4 candidate events.

Momentum Range (GeV)	Efficiency
(20,25)	64.0%
(25,30)	57.3%
(35,40)	47.8%
(45,50)	42.9%

Each trigger 10 event is corrected with the corresponding efficiency in the table 8.1 and then summed over these events. After considering the Hadron Anti effects, we get 7.73 Events.

Chapter 9

Systematics

We will describe the systematic errors in our analysis in this section. There are several important sources of systematic errors. The most important one is caused by the Monte Carlo Generator problem. Also the cuts I used could bias the results. I will discuss them separately.

9.1 Old and New MC Comparison

Because there are no published theoretical calculations in the literature about our signal decay mode $\Xi^\circ \to \Lambda^\circ\pi^\circ\gamma$, when we did the analysis initially, we used the generic Monte Carlo generator which is called GENBD8 in the CERN Library for our 3-body decay. Basically this generator assumes that the events are uniformly distributed in its phase space, and of course it may not be a good approximation. Later, Prof. Charles J. Goebel at the University of Wisconsin_Madison did a theoretical calculation for us in which he assumed all radiation came from changes in the hyperon magnetic moments during the decay $\Xi^\circ \to \Lambda^\circ\pi^\circ\gamma$. You can refer the appendix A for the calculation.

Based on his calculation, we developed a new Monte Carlo generator in our

analysis. Since the theoretical calculation is not published, we are going to list the results based on these two Monte Carlo generators in this thesis, and also do some comparison of these two Monte Carlo generators. We will use any discrepancy as one measure of the systematic error.

In the Fig. 9.1, the top two plots show us the angular distribution between the γ and the π^0 in the Ξ^0 CM system. In each of the plots, the histogram shows the distribution of the MC samples without any cuts applied. The dashed lines show accepted events after the cuts, and the arrows are the values of $\cos(\theta)$ of 4 candidate events. The bottom two plots show us the different number of Monte Carlo events which passed the same cuts for 1 Million Monte Carlo $\Xi^\circ \to \Lambda^\circ\pi^\circ\gamma$ events. We can see big different acceptances ($1.12 \times 10^{-3} vs. 2.15 \times 10^{-3}$) for the new and the old Monte Carlo generators for the same cuts.

9.2 Systematics by Monte Carlo Simulation

The first issue here is the Monte Carlo of our signal mode $\Xi^\circ \to \Lambda^\circ\pi^\circ\gamma$. Because there is no published theoretical literature about this decay mode, initially we used the isotropic n-body decay model with the name of GENBD8 to simulate the events from KTeV standard Monte Carlo. We stated in our previous section 9.1 that based on the Prof. Goebel's theoretical calculation, we made a new Monte Carlo generator. We assume the different efficiency corrections obtained using these two M.C. programs are a measure of our main systematic error.

After we applied all the cuts to the 1 Million Monte Carlo events, we got pretty different results for the two Monte Carlo generators. As we know from Section 8.5,

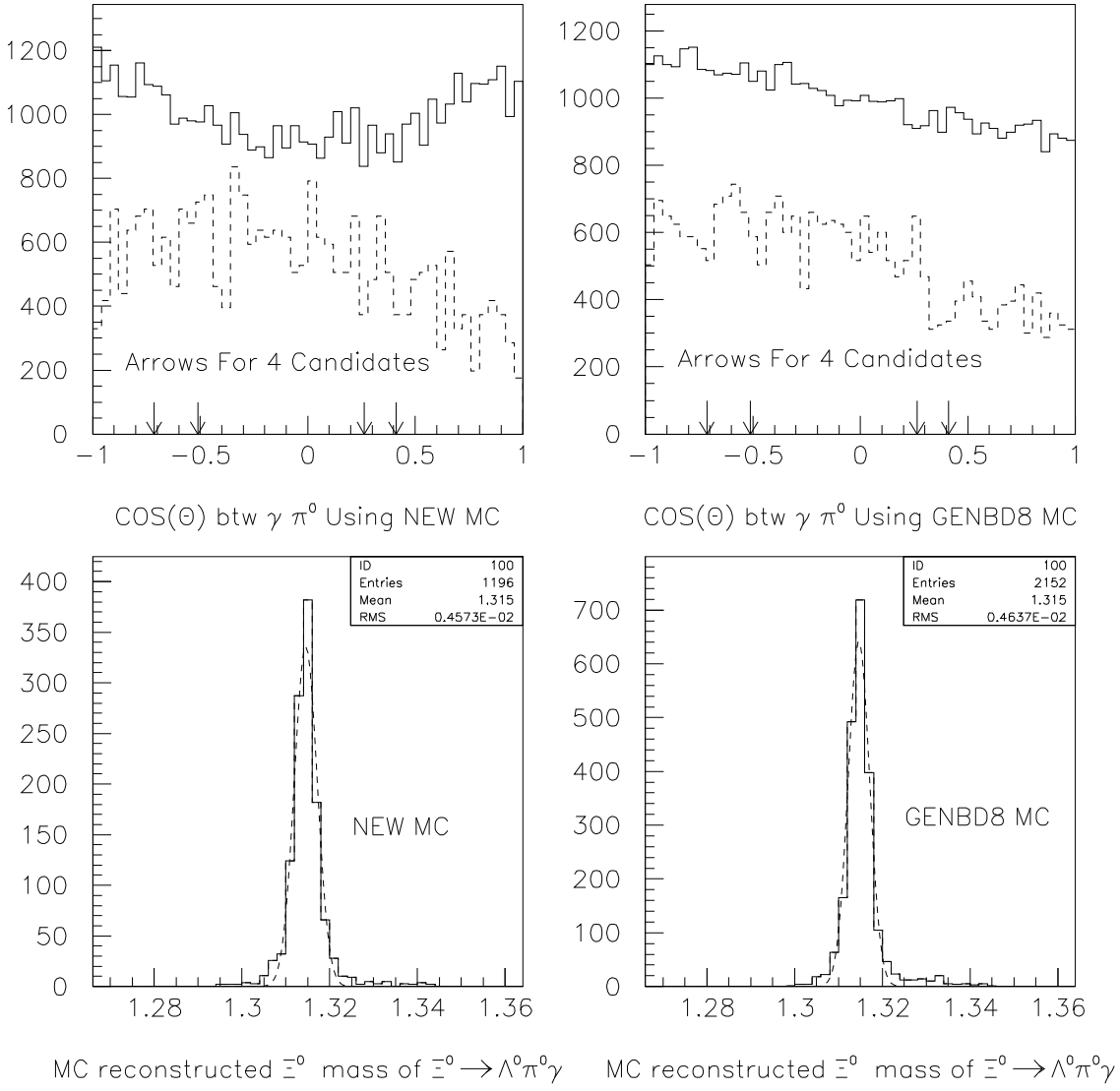

Figure 9.1: Comparasion of the NEW Monte Carlo and Old GENBD8 Monte Carlo for $\Xi^\circ \to \Lambda^\circ\pi^\circ\gamma$. The upper two plots are the $Cos(\theta)$ between γ and π^0. The bottom two plots are the reconstructed Ξ mass subjected to the same cuts on 1 Million $\Xi^\circ \to \Lambda^\circ\pi^\circ\gamma$ Monte Carlo events. These plots are in the arbitray scales.

we got 7.73 candidate events after the hadron anti correction. For the calculation of BR, we used the Ξ flux from Section 6.4 which is 301.8 Million, based on a trigger 11 analysis.

From the Table 9.1, we can see a big difference in the BR calculated by using efficiencies from these two M.C. programs. We estimate a systematic error from the M.C. to be half this difference, and it is $\pm 0.48 \times 10^{-5}$.

Table 9.1: Systematics caused by difference of the Old MC and the NEW MC Generator.

	Old GENBD8 MC	NEW MC
MC Events After Cuts	2152	1196
Efficiency	2.152×10^{-3}	1.196×10^{-3}
Efficiency Corrected Events	3570	6425
Branching Ratio	1.19×10^{-5}	2.14×10^{-5}

9.3 Systematics by Selection of the Cut Values

Also the systematic error could be caused by the selection of the cut values we applied. We will express our concern about several severe cuts like the coplanarity cut, the pt cut and the TRD cut. In the following analysis, we will discuss the Branching Ratio results without using these cuts. The invariant $\Lambda^0\pi^0$ mass plot for events without these three cuts was already showed at Figure 7.8.

In the Fig. 9.2, we plot the re-constructed mass peak for the $\Lambda^0\pi^0\gamma$ invariant

mass for the Old and New Monte Carlo and for Data on the tapes. All of them are subjected to the same cuts. A background appears because we have not used the final three cuts mentioned above. As we illustrate in the 3rd plot, we used a very simple and effective way to do the background subtraction.

In these 3 plots we used 3Mev for each mass bin. We will calcalate the background level in the two side bands of the third plot, and linearly fit the background level, and then subtract the fitted number from the center band in the plot. For the better background and signal ratio, we consider the areas of less than 1.310 Gev and larger than 1.319 Gev as our side bands. For the left side band, i.e. $[1.271, 1.310]$, there are 16 events in these 13 bins; for the right side band, i.e. $[1.319, 1.343]$, there are 6 events in these 8 bins. Based on this, we say that there are 1.23 background events per each left bin, and 0.75 events per each right bin. Linearly interpolating we find that there is 0.96 background events in the bin of $[1.310, 1.313]$, 0.94 background event in the bin of $[1.313, 1.316]$, and 0.91 background event in $[1.316, 1.319]$.

We still need to follow the same procedure as we did in section 8.5 for the Hadron-Anti correction of the events in the center band $[1.310, 1.319]$. There are 9 events in these bins. They are listed in the table 9.2. After we do the Hadron Anti correction for the trigger 10 data (8 of them), we get 14.86 events including 1 trigger 11 event. With the background subtraction, we get $14.86 \times (9 - 0.96 - 0.94 - 0.91)/9 = 10.22$ events.

We compare the results I got with the current analysis to the results with all the cuts in my previous discussion in Table 9.3. In Table 9.3, we make

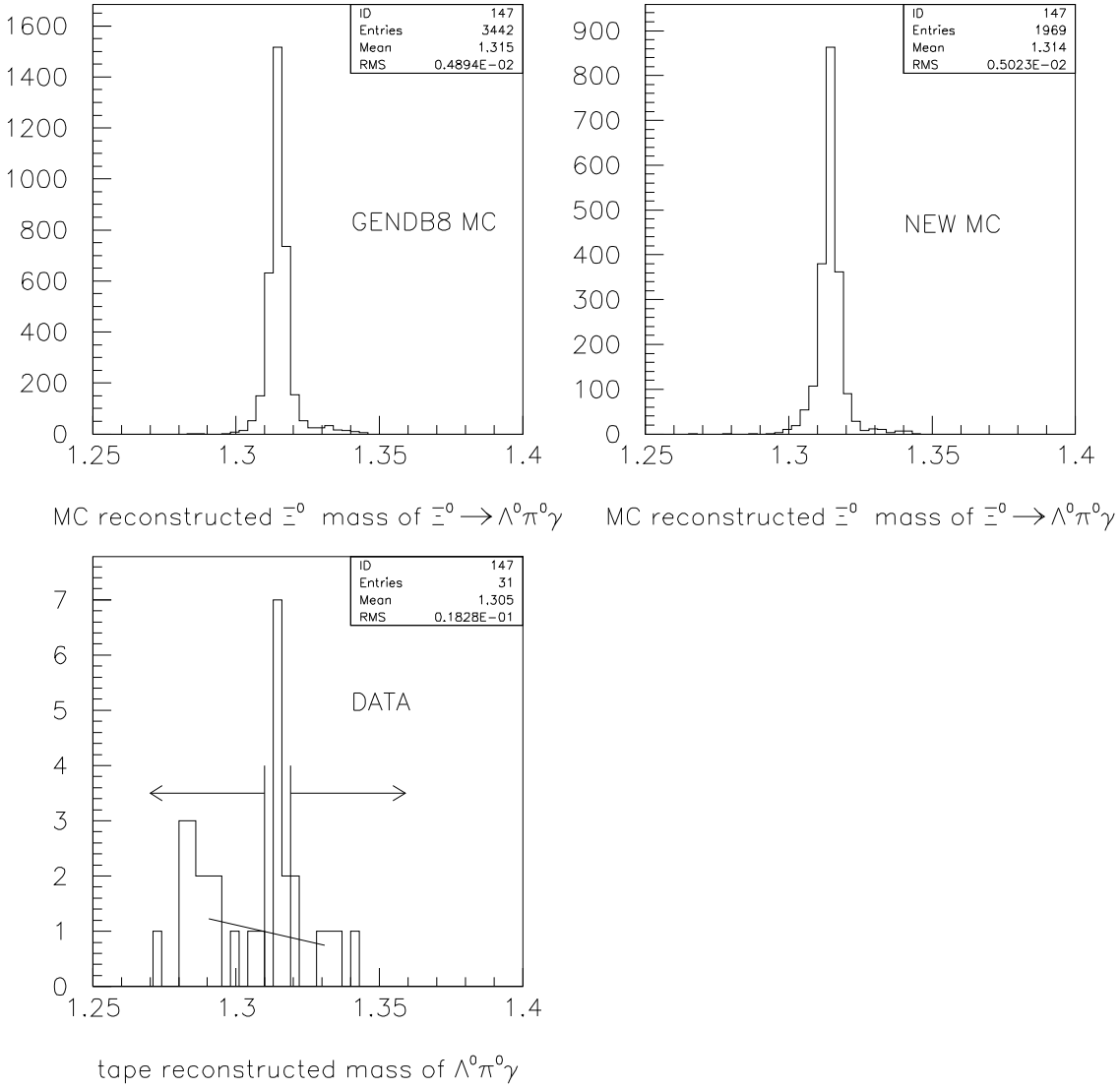

Figure 9.2: The first plot is the histogram for the constructed mass of Ξ for 1 Million GENBD8 Monte Carlo events. The 2nd plot is for the NEW Monte Carlo events. The 3rd plot is for the data. In this plot, we show the way we did the background subtraction. All 3 plots are subjected to the same cuts.

Table 9.2: The Detailed info. of these 9 candidate events.

RunNue	InvMass	$P_{\pi^-}(GeV)$	Trig10	Trig11
14745	1.315457	25.08478	-1	0
14853	1.313265	48.43148	-1	0
14956	1.315063	33.49725	-1	0
14986	1.315632	24.62168	-1	-1
15218	1.315668	19.12901	-1	0
15310	1.316296	36.87109	-1	0
15427	1.314119	19.66224	-1	0
15427	1.318065	18.10586	-1	0
15548	1.313911	36.26654	0	-1

efficiency corrections for both sets of cuts using only old GENDB8 for the events in the central band $[1.310, 1.319]$. The two results give BR's which are different by 0.01×10^{-5}. We assign half of this values ($\pm 0.005 \times 10^{-5}$) as a limit on systematic error due to our final 3 cuts.

Table 9.3: Systematics caused by some Severe Cuts in OLD GENBD8 MC

	With All the Cuts	Without Some Cuts
MC Events After Cuts	2152	3442-559
Efficiency	2.165×10^{-3}	2.883×10^{-3}
Signal Candidates	7.73	10.22
Efficiency Corrected Events	3570	3545
Branching Ratio	1.19×10^{-5}	1.18×10^{-5}

Also for the NEW Monte Carlo case, we got a similar table 9.4. We used the same procedure for the new Monte Carlo events without several cuts. We corrected the event number correspondingly, e.g., we only consider the events in the central band $[1.310, 1.319]$ as we discussed above. From this table 9.4, the two BR's difference is about 0.05×10^{-5}. We assign half of this value ($\pm 0.025 \times 10^{-5}$ as a limit on systematic error for this case.

We estimate a systematic error from these 3 cuts to be half the sum of these two numbers, and it is $\pm 0.015 \times 10^{-5}$.

Table 9.4: Systematics caused by some Severe Cuts in NEW MC

	With All the Cuts	Without Several Cuts
MC Events After Cuts	1196	1969-364
Efficiency	1.196×10^{-3}	1.627×10^{-3}
Signal Candidates	7.73	10.22
Efficiency Corrected Events	6425	6281
Branching Ratio	2.14×10^{-5}	2.09×10^{-5}

9.4 Systematics by Polarization Effect

For the unpolarized Ξ^o decay into spin-1/2 baryon and a spin-0 meson, the longitudinal polarization of the baryon will be proportional to the asymmetry parameter α. With that baryon decaying into the other final baryon, the angular distribution of the final spin-1/2 baryon is related to the asymmetry parameter and the polarization of the decaying particle [12]. In the case of our normalization mode, we observed there was 7% systematic error if we didn't consider this effect for $\Xi^\circ \to \Lambda^\circ\pi^\circ$. In the current Monte Carlo generator I used, we couldnot introduce this effect. Here we assume this ($1.67\times10^{-5}\times7\% = 0.12\times10^{-5}$) was the systematic error of our signal mode $\Xi^\circ \to \Lambda^\circ\pi^\circ\gamma$ because of the polarization effect.

9.5 Summary of all systematics

If we combine all the sysmatics which we discussed in the previous subsections, we get the total sysmatics is $\pm 0.50 \times 10^{-5}$.

Chapter 10

Conclusion

10.1 Summary of Results

The decay $\Xi^\circ \to \Lambda^\circ\pi^\circ\gamma$ has been searched for in the 1999-2000 dataset of the KTeV/E799-II collaboration at FermiLab.

We used the principal decay of $\Xi^\circ \to \Lambda^\circ\pi^\circ$ where Λ decays to a proton and a π^- as the flux normalization mode. We used the isotropic decay model and the new Monte Carlo model based on the calculation of PDG Page 684 and Prof. Charles J Goebel to simulate the signal mode $\Xi^\circ \to \Lambda^\circ\pi^\circ\gamma$. 4 candidate events for decay mode $\Xi^\circ \to \Lambda^\circ\pi^\circ\gamma$ were observed. Various background events were also simulated and studied, but no background events were observed. We studied the Systematics error, and also used poisson statistics from PDG [8] and Feldman and Cousins' paper [60] to get the statistical error at 90% level with 4 observed events. We got the Branching Ratio of the decay mode $\Xi^\circ \to \Lambda^\circ\pi^\circ\gamma$:

$$\text{B.R. } (90\%CL) = (1.67\ ^{+1.45}_{-0.80}(stat.)\ \pm 0.50(syst.)) \times 10^{-5}$$

$$\text{B.R. } (68.27\%CL) = (1.67\ ^{+1.16}_{-0.69}(stat.)\ \pm 0.50(syst.)) \times 10^{-5}$$

The BR is the average of that obtained using the efficiency obtained from the

two Monte Carlo programs.

10.2 Prospects

Future experiments must collect more Ξ° decays for better observing and studying this $\Xi^\circ \to \Lambda^\circ\pi^\circ\gamma$ decay mode.

This hyperon weak neutral radiative decay mode was not well-studied theoretically or experimentally in the past. Hopefully, later theorists will pay much more attention to it and develop a more complete theory about it. Based on that, more accurate Monte Carlo simulation can be done and a more precise branching fraction can be achieved.

Appendix A

A theoretical calculation of BR for the decay

$\Xi^\circ \to \Lambda^\circ \pi^\circ \gamma$

This work is done by combining PDG [8] 864 and a calculation of Prof. Charles J. Goebel at the Physics Department of University of Wisconsin-Madison.

A.1 Hyperon nonleptonic decay fundmentals

The amplitude for a spin-1/2 hyperon decaying into a spin-1/2 baryon and a spin-0 meson may be be written in the form

$$M = G_F m_\pi^2 \cdot \overline{u_f}(A - B\gamma_5)u_i \tag{A.1}$$

where A and B are constants [61]. Starting from this expression, we have

$$u_i = \begin{pmatrix} \chi_i \\ 0 \end{pmatrix} \tag{A.2}$$

$$u_f = (\frac{E_f + m_f}{2m_f}) \begin{pmatrix} \chi_f \\ \frac{(\sigma \cdot p_f)}{E_f + m_f}\chi_f \end{pmatrix} \tag{A.3}$$

where χ_i and χ_f are two-component spinors. Thus

$$M = G_F m_\pi^2 (\frac{E_f + m_f}{2m_f})^{1/2} (A\chi_f^\dagger \chi_i + B\chi_f^\dagger \frac{(\sigma \cdot p_f)}{E_f + m_f}\chi_i) \quad (A.4)$$

We now define $\hat{p} = p_f/|p_f|$, $s = A$, and $p = |p_f|B/(E_f + m_f)$. Thus we get

$$M = G_F m_\pi^2 (\frac{E_f + m_f}{2m_f})^{1/2} [\chi_f^\dagger (s + p\sigma \cdot \hat{p})\chi_i] \quad (A.5)$$

The transition rate is proportional to

$$|\chi_f^\dagger (s + p\sigma \cdot \hat{p})\chi_i|^2 = tr[(\frac{1 + \sigma \cdot n_f}{2})(s + p\sigma \cdot \hat{p})(\frac{1 + \sigma \cdot n_i}{2})(s^* + p^*\sigma \cdot \hat{p})] \quad (A.6)$$

Evaluating the trace by standard means, we find that the transition rate is proportional to

$$\Gamma = 1 + \gamma n_f \cdot n_i + (1 - \gamma)(n_f \cdot \hat{p})(n_i \cdot \hat{p}) + \alpha(n_f + n_i) \cdot \hat{p} + \beta \hat{p} \cdot (n_f \times n_i) \quad (A.7)$$

where the $\hat{p}$ is the unit vector in the direction of the final baryon mementum, and n_f and n_i are unit vectors in the directions of the initial and final baryon spins. The parameters α, β, and γ are defined as

$$\alpha = 2Re(s^* p)/(|s|^2 + |p|^2), \quad (A.8)$$

$$\beta = 2Im(s^* p)/(|s|^2 + |p|^2), \quad (A.9)$$

$$\gamma = (|s|^2 - |p|^2)/(|s|^2 + |p|^2) \quad (A.10)$$

where $s = A$ and $p = |p_f|B/(E_f + m_f)$; here E_f and p_f are the energy and momentum of the final baryon. The parameters α, β, γ satisfy

$$\alpha^2 + \beta^2 + \gamma^2 = 1 \quad (A.11)$$

A.2 $\Xi^\circ \to \Lambda^\circ\pi^\circ$Decay Rate

For decay $\Xi^\circ \to \Lambda^\circ\pi^\circ$, we consider the unpolarized case for Ξ^0. From the previous section, the transition rate for $\Xi^\circ \to \Lambda^\circ\pi^\circ$ is proportional to

$$tr[A + B\sigma \cdot p^2] \doteq 2(A^2 + B^2p^2) \tag{A.12}$$

where we use $tr\vec{1} = 2$, $tr\vec{\sigma} = 0$ and $tr\vec{\sigma}\vec{\sigma} = 2\vec{1}$

Use the Golden Rule, and let's integrate the whole phase space. We get

$$\Gamma = 2\pi \frac{2(A^2 + B^2p^2)}{v \cdot 2\omega} \frac{vd^3p\delta(\omega_p - \Delta)}{(2\pi)^3} \tag{A.13}$$

$$= \frac{1}{\pi}(A^2 + B^2p^2)p|_{\omega_p=\Delta} \tag{A.14}$$

Where $M_\Xi - M_\Lambda \equiv \Delta$ in our notation, and p is the momentum of particle π in the Center of Mass system of Ξ.

A.3 $\Xi^\circ \to \Lambda^\circ\pi^\circ\gamma$Decay Rate

In the following calculation for the decay rate of $\Xi^\circ \to \Lambda^\circ\pi^\circ\gamma$, we will use the static approximation method. We have the decay diagram like A.1. The decay has two possible components, and we have two parts in the amplitude formula.

If we assume radiation originates exclusively from the hyperon magnetic moment, the amplitude of the decay is like

$$\frac{(A + B\sigma \cdot p)}{\sqrt{v \cdot 2\omega}} \frac{(\sigma \cdot k \times \epsilon)}{\sqrt{v \cdot 2k}} \frac{\mu_\Xi}{(-k)} + \frac{(\sigma \cdot k \times \epsilon)}{\sqrt{v \cdot 2k}} \frac{(A + B\sigma \cdot p)}{\sqrt{v \cdot 2\omega}} \frac{\mu_\Lambda}{k}$$

$$= \frac{1}{\sqrt{4v^2\omega k^3}}[\mu_\Lambda\{A\sigma \cdot k \times \epsilon + Bp \cdot k \times \epsilon + iB\sigma \cdot (k \times \epsilon) \times p\}$$

$$-\mu_\Lambda\{A\sigma \cdot k \times \epsilon + Bp \cdot k \times \epsilon - iB\sigma \cdot (k \times \epsilon) \times p\}]$$

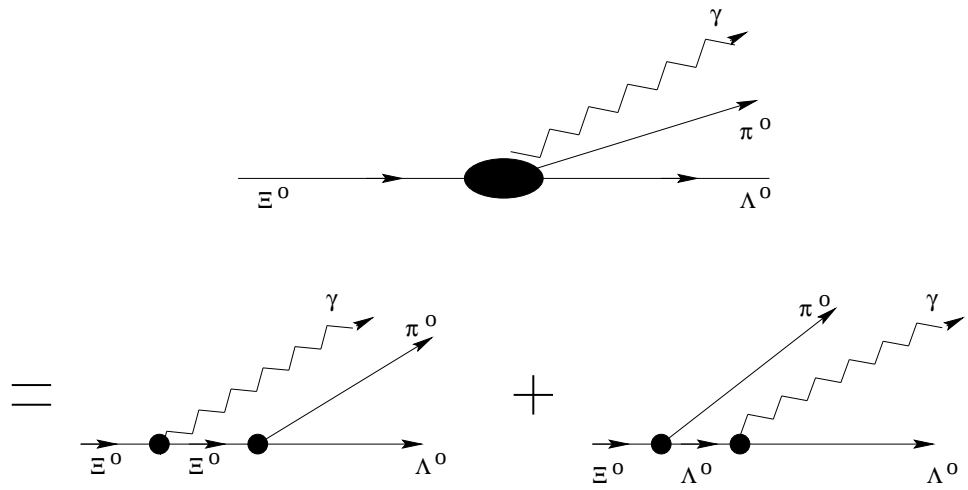

Figure A.1: We have two possibilities for the decay diagram of $\Xi^\circ \to \Lambda^\circ \pi^\circ \gamma$.

$$= \frac{1}{\sqrt{4v^2\omega k^3}}[\{(\mu_\Lambda - \mu_\Xi)Ak \times \epsilon + i(\mu_\Lambda + \mu_\Xi)B(k \times \epsilon) \times p\} \cdot \sigma$$
$$+(\mu_\Lambda - \mu_\Xi)B(p \times k) \cdot \epsilon] \qquad \text{(A.15)}$$

The transition rate is proportional to $tr|above|^2$

$$tr|above|^2 = 2[\{DA^*k \times \epsilon - iSB^*(k \times \epsilon) \times p\}$$
$$\cdot\{DAk \times \epsilon - iSB(k \times \epsilon) \times p\}$$
$$+D^2B^*B(p \times k \cdot \epsilon)^2] \qquad \text{(A.16)}$$

Where $D = \mu_\Lambda - \mu_\Xi$ and $S = \mu_\Lambda + \mu_\Xi$. We will use the below formula to evaluate the transition rate

$$\sum_\epsilon (k \times \epsilon) \cdot (k \times \epsilon) = \sum_\epsilon k^2\epsilon^2 - (k \cdot \epsilon)^2 = 2k^2 \qquad \text{(A.17)}$$

$$\sum_\epsilon (k \times \epsilon) \cdot (k \times \epsilon \times p) = 0 \qquad \text{(A.18)}$$

$$\sum_{\epsilon}[(k\times\epsilon)\times p]^2 = \sum_{\epsilon}(k\cdot p)^2\epsilon^2 + k^2(p\cdot\epsilon)^2$$
$$= 2(k\cdot p)^2 + p\cdot(k^2 - k\cdot k)\cdot p$$
$$= (k\cdot p)^2 + k^2p^2 \tag{A.19}$$
$$\sum_{\epsilon}(p\times k\cdot\epsilon)^2 = (p\times k)^2$$
$$= p^2k^2 - (p\cdot k)^2 \tag{A.20}$$

Let's integrate the whole phase space. We got

$$\frac{\Gamma_{\Xi^\circ\to\Lambda^\circ\pi^\circ\gamma}}{d\Omega} = \frac{2\pi}{4v^2\omega_p k^3}\int\int[2D^2A^2k^2 + S^2B^2k^2p^2(1+C^2)$$
$$+D^2B^2k^2p^2(1-C^2)]\frac{v^2d^3kd^3p\delta(\omega_p+k-\Delta)}{(8\pi^3)^2} \tag{A.21}$$

Simplify the intergal a little bit. We got

$$\frac{\Gamma_{\Xi^\circ\to\Lambda^\circ\pi^\circ\gamma}}{d\Omega} = \frac{1}{32\pi^4}[2A^2D^2 + B^2p^2\{(S^2+D^2)+(S^2-D^2)C^2\}]$$
$$\frac{(\Delta-\omega)}{\omega}p^2dp|_{k=\Delta-\omega} \tag{A.22}$$

In our expression, we have

$$C \equiv \frac{k\cdot p}{kp}, \tag{A.23}$$
$$\Delta \equiv M_\Xi - M_\Lambda, \tag{A.24}$$
$$S \equiv \mu_\Lambda + \mu_\Xi, D \equiv \mu_\Lambda - \mu_\Xi, \tag{A.25}$$
$$m^2 + p^2 = (\Delta - k)^2 \equiv \omega^2 \tag{A.26}$$

where μ_Λ, μ_Ξ are the magnetic moments, M_Λ and M_Ξ are the invariant masses of particle Λ and Ξ which you can get from PDG. k and p are the momentum of the radiative γ and π^0 during the process of the decay.

Using the following integral formulas helps to evaluate the transition rate in the above formula

$$\int \frac{x^2 dx}{\sqrt{x^2+a^2}} = \frac{x}{2}\sqrt{x^2+a^2} - \frac{a^2}{2} log(x+\sqrt{x^2+a^2}) \tag{A.27}$$

$$\int \frac{x^4 dx}{\sqrt{x^2+a^2}} = \frac{x^3}{4}\sqrt{x^2+a^2} - \frac{3a^3}{4}\int \frac{x^2 dx}{\sqrt{x^2+a^2}} \tag{A.28}$$

After integrating the solid angle and momentum phase space, We can get the result

$$\begin{aligned}\Gamma_{(\Xi^\circ \to \Lambda^\circ \pi^\circ \gamma)} = \frac{1}{8\pi^3}[2A^2D^2\{&\frac{\Delta^2\sqrt{\Delta^2-m^2}}{2} - \frac{(\Delta^2-m^2)^{3/2}}{3} \\ &- \frac{m^2\Delta}{2} log\frac{(\Delta+\sqrt{\Delta^2-m^2})}{m}\} \\ +B^2(\frac{4S^2}{3}+\frac{2D^2}{3})\{&\frac{\Delta^2(\Delta^2-m^2)^{3/2}}{4} - \frac{3m^3\Delta^2(\Delta^2-m^2)^{1/2}}{8} \\ &- \frac{(\Delta^2-m^2)^{5/2}}{5} - \frac{3m^5\Delta}{8} log\frac{(\Delta+\sqrt{\Delta^2-m^2})}{m}\}]\end{aligned} \tag{A.29}$$

Where A, B are the constant which you can get from the measurement of α, β or γ. m is the mass of π^0. Other variables are with the same meaning as disscussed before.

A.4 $\Xi^\circ \to \Lambda^\circ \pi^\circ \gamma$ Branching Ratio

In the previous sections, we got the decay rate Eq. A.14 and Eq. A.29 for decay modes $\Xi^\circ \to \Lambda^\circ \pi^\circ$ and $\Xi^\circ \to \Lambda^\circ \pi^\circ \gamma$. Since the decay $\Xi^\circ \to \Lambda^\circ \pi^\circ$ is well studied, from the ratio of these two decay rates we can get the Branching Ratio of the mode $\Xi^\circ \to \Lambda^\circ \pi^\circ \gamma$.

From PDG, we know the $\alpha = -0.411$. We assume that $\phi = 0$ which is not quite $21^0 \pm 12^0$ as listed in the book. Using the Eq. A.8 to solve the equation, we

got the relation for A and B. $B = -3.5683A$. We assume $A = 1$ and $B = -3.5683$ in our calculation. We can get two solutions for solving equation from α. The reason why we choose this solution is that only it agrees with the values of γ in the particle data book [8].

In the natural unit, $\hbar = c = 1$, the nuclear magneton $\mu_N = e\hbar/2m_p = e/2m_p$, we can get

$$\mu_N^2 = \frac{e^2}{4m^2} = \frac{\pi\alpha}{m_p^2} \tag{A.30}$$

because of

$$\alpha = \frac{e^2}{4\pi} \tag{A.31}$$

In the calculation, we changed the unit of μ and other variables to the natural unit. We have all the variables like this

$$A = 1 \tag{A.32}$$

$$B = -3.5683 \tag{A.33}$$

$$m \equiv 0.1349766 Gev \tag{A.34}$$

$$\Delta \equiv M_\Xi - M_\Lambda = 0.19915 Gev \tag{A.35}$$

$$S = \mu_\Xi + \mu_\Lambda = (-1.250 - 0.613)\mu_N = -1.683\mu_N \tag{A.36}$$

$$D = \mu_\Xi - \mu_\Lambda = (-1.250 + 0.613)\mu_N = -0.637\mu_N \tag{A.37}$$

When we input these number into the the decay rates Eq. A.14 and Eq. A.29, we get

$$\Gamma_{(\Xi^\circ \to \Lambda^\circ \pi^\circ)} = 5.294 \times 10^{-2} \tag{A.38}$$

$$\Gamma_{(\Xi^\circ \to \Lambda^\circ \pi^\circ \gamma)} = 9.6543 \times 10^{-8} \tag{A.39}$$

Based on this, we get that the Branching Fraction of $\Xi^\circ \to \Lambda^\circ\pi^\circ\gamma$ is

$$BF(\frac{\Xi^\circ \to \Lambda^\circ\pi^\circ\gamma}{\Xi^\circ \to \Lambda^\circ\pi^\circ}) = 1.824 \times 10^{-6} \tag{A.40}$$

Bibliography

[1] L. K. Gershwin, *et al.*, *Phys. Rev. 188, 2077* (1969)

[2] Y. Hara, *Phys. Review. Letter 12, 378* (1964)

[3] Lach, Zenczyskowski, Int. Journal of Modern Physics **A10**, 3817 (1995)

[4] E. Ramberg, *The 3rd Int Conf on Hyperons,Charm,and Beauty, Genoa, Italy* (1998) (Conference Proceedings to be published in Nucl. Phys. B)

[5] S. L. Glashow, *Nucl. Phys. A22, 579* (1961)

[6] S. Weinberg, *Phys. Rev. Lett. 19, 1264* (1967)

[7] A. Salam, *Elementary Particle Theory* (1968)

[8] S. Eidelman et al., *Particle Data Group, Phys. Lett. B* **592** 1(2004)

[9] P. Petersen, *et al.*, *Physics Review Letters* **57**, 949 (1986)

[10] F. Gilman, M. B. Wise, *Phys. Rev. D* **19** 976(1976)

[11] J. Donoghue *et al.*, *Low-energy weak interactions of quarks,* Phys. Rep. **131**, 403 (1986)

[12] J.D. Jackson, *Notes about Radiative Hyperon Decays,* Sept. (2003)

[13] G. Guglielmo, *PhD thesis, The University of Minnesota,* August 1994.

[14] L.G. Pondrom, *Physics Report* **122,** 58 (1985)

[15] Skubic, *et al.*, *Phys. Rev.* **D18,** 1355 (1978)

[16] Ramberg *et al.*, *Phys. Lett.* **B338**, 403 (1994)

[17] R. E. Behrends, *et al.*, *Physical Review* **111**, 1691 (1958)

[18] C. James, *et al.*, *Physical Review Letters* **64**, 843 (1990)

[19] V. Bocean, S. Childress, R. Coleman, R. Ford, D. Jensen, *KTeV Internal Note* **466** .

[20] K. Arisaka, *et al.*, *KTeV Design Report, FN-580* (1992)

[21] T. Kobilarcik, R. Tokarek, S. Childress, *et al.*, *KTeV Internal Note* **0097** (1993)

[22] T. Kobilacik, *et al.*, *KTeV Internal Memo 97*

[23] P. Shawhan, *et al.*, *KTeV Internal Memo 257*

[24] D. Jensen, *KTeV Internal Note* **0050** (1992)

[25] E. Bartz, *et al.*, *KTeV Drift Chamber Electronics Design Report, KTeV Internal Note* **190** (1994)

[26] G. Graham, *et al.*, *KTeV Internal Note* **185** (1994)

[27] N. Solomey, *KTeV Internal Note* **569** (1998)

[28] John Belz, *KTeV Internal Note* **0080** (1992)

[29] D. Jensen, *KTeV Internal Note* **0088** (1992)

[30] A. Roodman, *Conference Record of ICHEP 96,* (1996)

[31] R. J. Yarema, *et al.*, *KTeV Internal Note* **0203** (1992)

[32] P. Shanahan, *Proceedings of ICHEP, Frascati, Italy* (1996)

[33] A. Roodman, "The KTeV pure CsI calorimeter", *Proceedings of the VII International Conference on Calorimetery, Tucson, Arizona,* World Scientific (1998)

[34] E. Cheu, H. Sanders, *et al.*, *KTeV Internal Note* **0129** (1993)

[35] C. Bown, E. Cheu, *et al.*, *KTeV Internal Note* **0298** (1995)

[36] S. Schnetzer, *KTeV Internal Note* **191** (1994)

[37] R. Tesarek and S. Schnetzer, *KTeV Internal Note* **215** (1994)

[38] S. T. Bright, *PhD thesis, The University of Chicago,* (2000)

[39] B. Tony, M. Peter, *KTeV Internal Note* **0198** (1994)

[40] B. Tony, M. Peter, *KTeV Internal Note* **0199** (1994)

[41] Peter Mikelsons, *KTeV Internal Note* **0201**

[42] R. Kessler, *KTeV Internal Note* **0361**

[43] B. Winstein, *KTeV Internal Note* **0116** (1993)

[44] P. Mikelsons, *KTeV Internal Note* **347,** (1995)

[45] R. Kessler, *KTeV Internal Note* **361,** (1996)

[46] P. Krolak, *et al.*, *KTeV Internal Note* **267**, (1994)

[47] S. Bright, *KTeV Internal Note* **369**, (1996)

[48] Peter Shawhan, *KTeV Internal Note* **0492** (1998)

[49] M. Pang, *KTeV Internal Note* **0449** (1997)

[50] Jim Graham, *KTeV Internal Note* **0764** (2000)

[51] P.S. Shawhan, *Ph.D. thesis (The Univ. of Chicago, Dec. 1999)*

[52] A.J. Malensek, *Preprint FN-341, Fermi National Accelerator Laboratory,* (1981)

[53] R.A. Briere, *PhD thesis, The University of Chicago,* (1995)

[54] K. Hanagaki, *PhD thesis, Osaka University, Japan,* (1998)

[55] K.S. McFarland, *PhD thesis, The University of Chicago,* (1994)

[56] A. Ashkan, *PhD thesis, The University of Wisconsin_Madison,* (1999)

[57] John Shields, *Fermilab KTeV meeting talk* (Jan. 18, 2003)

[58] S. Barshay and R. Behrends, *Physical Review* **114**, 931 (1959)

[59] E. Monnier and KTeV Collaboration, *Nucl. Phys. Proc. Suppl. 75B, 36, (1999)*

[60] Gary J. Feldman, Robert D. Cousins, Phys. Rev. D. Vol. 57, Num. 7, P3873 (1976) (1998)

[61] E.D. Commins and P.H. Bucksbaum, Weak Interaction of Leptons and Quarks, *Cambridge University Press, Cambridge, England,* (1983)

[62] Marshak, Riazuddin and Ryan, *Theory of weak interactions in particle physics,* John Wiley & Sons, Inc. (1969)